

QUANTUM TESTS OF THE UNIVERSALITY OF FREE FALL

Von der QUEST-Leibniz-Forschungsschule der
Gottfried Wilhelm Leibniz Universität Hannover

zur Erlangung des Grades
Doktor der Naturwissenschaften
Dr. rer. nat. -
genehmigte Dissertation von

Dipl.-Phys. Dennis Schlippert
geboren am 11.02.1985,
in Hannover

2014

Referent: Prof. Dr. Ernst M. Rasel
Korreferent: Prof. Dr. Wolfgang Ertmer
Korreferent: Prof. Dr. Wolfgang P. Schleich
Tag der Promotion: 24.11.2014

Abstract

Quantum Tests of the Universality of Free Fall

In the process of formulating a “theory of everything” that aims to provide a self-contained model of modern physics by unifying all four fundamental interactions, two theoretical frameworks have yielded important contributions: quantum mechanics, which can explain the nature of physics at the most microscopic length scales such as the origin of spectra of electrons bound in atomic systems, and EINSTEIN’s general relativity, that conveys our understanding of gravity over the largest distances across the universe. Although no theory of “quantum gravity”, that is consistent over all energy scales, exists to date, certain modifications may enable a reconciliation of quantum mechanics and general relativity. These approaches allow for violations of the universality of free fall (UFF), that among LORENTZ invariance and local position invariance constitute EINSTEIN’s equivalence principle. The UFF states that all bodies, located at the same space-time point, experience the same acceleration in a gravitational field independently of their composition. Because of its central role in modern physics the UFF has been tested extensively in many experiments, most of which utilized classical test masses. Quantum mechanical tests of the UFF differ from classical ones in various aspects such as the coherence length and spin polarization of the test masses.

In this thesis, the first inertial-sensitive matter wave interferometer comparing the free fall of two different elements, ^{87}Rb and ^{39}K , was realized. This quantum test of the UFF yielded an EÖTVÖS ratio $\eta_{\text{Rb,K}} = (0.3 \pm 5.4) \times 10^{-7}$, and was limited by statistical uncertainty. In this work, an existing apparatus for rubidium interferometry was extended to the use of potassium and the first inertial-sensitive potassium matter wave interferometer with a resolution to gravitational acceleration of $\sigma_{\text{K}} = 3 \times 10^{-6} \text{ m/s}^2$ after 4096 s integration has been demonstrated. A description of the experiment including the technical realization and the techniques used is provided. Specifically, the challenges imposed by the use of potassium, which in comparison to rubidium has a smaller mass and lower hyperfine energy splitting, are examined. The thesis furthermore discusses an assessment of the systematic effects influencing the dual species measurement and presents future strategies to further improve the performance of the apparatus. As a preliminary result, it was possible to improve the potassium short-term sensitivity to gravitational acceleration to $\sigma_{\text{K}} = 2.1 \times 10^{-5} \text{ m/s}^2/\sqrt{\text{Hz}}$. The results of this thesis pave the way for exciting future experiments to be performed in large-scale apparatuses and in space.

Key words: Matter wave interferometry, Universality of Free Fall, Precision measurements

Zusammenfassung

Quantentests der Universalität des freien Falls

Zur Formulierung einer „Weltformel“, deren Ziel eine in sich abgeschlossene Vereinigung aller vier fundamentalen Wechselwirkungen ist, haben zwei Theorien große Beiträge geleistet: die Quantenmechanik, welche die Grundlagen der Physik auf kleinsten Längenskalen, wie zum Beispiel die Ursprünge der Spektren von Elektronen in atomaren Systemen, erklärt, und EINSTEINS allgemeine Relativitätstheorie, die unser Verständnis der Gravitation auf den größten Längenskalen im Universum liefert. Gewisse Modifikationen der allgemeinen Relativitätstheorie erlauben ihre Vereinigung mit der Quantenmechanik, allerdings konnte bisher noch keine über alle Energieskalen gültige Theorie der „Quantengravitation“ formuliert werden. Einige dieser Modifikationen erlauben beispielsweise Verletzungen der Universalität des freien Falls (UFF), welche neben der LORENTZ-Invarianz und der lokalen Positions-Invarianz die Grundlage des EINSTEINSCHEN Äquivalenzprinzips bildet. Die UFF besagt, dass alle Körper, die sich am selben Raumzeitpunkt befinden, unabhängig von ihrer Zusammensetzung identische Beschleunigungen in einem Gravitationsfeld erfahren. Wegen ihrer zentralen Rolle in der modernen Physik wurde die UFF in zahlreichen Experimenten mit vorwiegend klassischen Testmassen umfangreich getestet. Quantenmechanische Tests der UFF unterscheiden sich von ihren klassischen Gegenstücken in vielerlei Hinsicht, wie zum Beispiel in der Kohärenzlänge und der Spinpolarisation der Testmassen.

Im Rahmen dieser Arbeit wurde das erste beschleunigungsempfindliche Materiewelleninterferometer basierend auf ^{39}K und ^{87}Rb für einen Vergleich der Freifallbeschleunigungen realisiert. Dieser Quantentest der UFF führte zu einer durch statistische Unsicherheit limitierten Bestimmung des EÖTVÖS-Verhältnisses $\eta_{\text{Rb,K}} = (0.3 \pm 5.4) \times 10^{-7}$. Hierzu wurde ein existierendes Rubidium-Materiewelleninterferometer für den Betrieb mit Kalium erweitert. Es konnten hierbei mit einer Auflösung von $\sigma_{\text{K}} = 3 \times 10^{-6} \text{ m/s}^2$ nach 4096 s Integrationszeit die ersten beschleunigungsempfindlichen Messungen mit Kalium demonstriert werden. Die spezifischen Herausforderungen in Verbindung mit dem Element Kalium, welches eine geringere Masse und eine kleinere Hyperfeinaufspaltung als Rubidium besitzt, werden bei der Beschreibung des experimentellen Aufbaus und der Methoden behandelt. Weiterhin werden in dieser Arbeit die für den Test der UFF relevanten systematischen Effekte analysiert und Strategien zur Verbesserung der bisher erreichten Ergebnisse zu verbessern. Im Rahmen erster Verbesserungen war es möglich, eine Kurzzeitsensitivität des Kaliuminterferometers von $\sigma_{\text{K}} = 2.1 \times 10^{-5} \text{ m/s}^2/\sqrt{\text{Hz}}$ zu erreichen. Die Ergebnisse dieser Arbeit ebnen den Weg für zukünftige Experimente in Apparaturen mit großer Basislinie und im Weltraum.

Schlagwörter: Materiewelleninterferometrie, Universalität des freien Falls, Präzisionsmessungen

Acknowledgments

Ich danke meiner Familie, die mir geholfen hat, bis hierhin zu kommen. Mein größter Dank gilt meiner Schwester Daniela und meinen Eltern Sonja und Klaus, ohne deren Liebe ich niemals derjenige wäre, der ich heute bin. Ich möchte auch meinen Großeltern Ruth, Siegfried, Lucie und Friedrich für die Unterstützung, die ich schon mein ganzes Leben lang von ihnen bekomme, danken. Danke für einfach ALLES! Ein großes Dankeschön gilt auch Johanna, die in den letzten Jahren immer für mich da war.

Ich möchte Ernst Rasel für all sein Vertrauen in mich danken. Ohne seine Unterstützung wäre der Weg vom Hiwi in 2008, über zwei USA-Aufenthalte und die Diplomarbeit, bis hierhin nicht möglich gewesen. Ich danke auch Wolfgang Ertmer, der maßgeblich an der Formung des Umfelds, in dem ich arbeiten durfte, beteiligt war und ist. Jenes Arbeitsumfeld ist geprägt von vielen unglaublich hilfsbereiten Menschen. Vielen Dank an Frau Ohlendorf, Frau Thiele-Bode, Frau Göldner-Pauer, Frau Hünitzsch, Frau Faber und Frau Pfennig, und auch der Werkstatt für ihren Einsatz. Ich danke all meinen Freunden und Kollegen, die mich in den letzten Jahren begleitet haben. Durch Maic Zaiser bin ich ans Institut gekommen und habe früh Unzähliges lernen dürfen. Mit Jonas Hartwig habe ich den Großteil der Zeit am Experiment verbracht und bin bis heute von seinem Elan begeistert und motiviert. Vor allem möchte ich auch Henning Albers und Logan Richardson für ihre unermüdliche Aufrechterhaltung des Betriebs im Labor während des letzten Jahres danken. Sie sind eine wahre Bereicherung. Vielen Dank an Daniel Tiarks, der gemeinsam mit Jonas die Grundlagen für die Interferometrie and unserem Experiment geschaffen hat. Ich danke auch Christian Meiners und Jonas Matthias für ihren Einsatz am Experiment. Ulrich Velte, Christina Rode und Nils Winter haben zur Schaffung der Grundlagen für die Ergebnisse dieser Arbeit beigetragen. Vielen Dank an alle Freunde, die ich am Insitut gewinnen durfte! Auch die Zeit mit John Debs wird unvergessen bleiben. Ohne die zahlreichen Korrekturen von und Diskussionen mit meinen Kollegen Christian Schubert, Jonas, Logan, Henning, Albert Roura, Mike Hohensee, Paul Hamilton, Stephan Seidel, Holger Ahlers, Waldemar Herr, Gunnar Tackmann, Torben Schulze, Peter Berg, Maike Lachmann, und Dennis Becker wäre diese Arbeit niemals fertig geworden. Ich möchte auch Wolfgang Schleich für die Übernahme des externen Gutachtens dieser Dissertation danken. Ich danke außerdem HALOSTAR für die finanzielle Unterstützung in den ersten Jahren meiner Doktorarbeit.

Over the last years I was able to spend a little more than one year in the USA during two separate trips. Without the trust and help of many involved people, my experiences would have never been the same. I would like to thank Nan Yu, Jim Kellogg, Jim Kohel, Rob Thompson, and Dave Aveline at JPL for teaching me. Special thanks go out the all my colleagues at UC Berkeley. Many thanks to Holger Müller for hosting me. I have always found his way of educating students fascinating and inspiring. Finally, many thanks to Paul Hamilton and Mike Hohensee for all the discussions and explaining their view of physics to me.

Contents

1	Introduction	1
2	Theoretical description of methods	7
2.1	Brief theoretical description of matter wave interferometry	7
2.1.1	Beam splitting process	7
2.1.2	Mach-Zehnder geometry	10
2.1.3	Sensitivity formalism	12
2.2	Quantifying violations of the Universality of Free Fall	13
3	Experimental setup	17
3.1	Vacuum system and peripheral installations	17
3.1.1	Vertical magnetic bias field	18
3.1.2	Radio-frequency manipulation	19
3.2	Potassium laser system	23
3.2.1	Cooling and trapping	25
3.2.2	Shared fiber distribution system	27
3.2.3	Coherent manipulation	28
3.3	Shared interferometry and detection optics	31
4	Matter wave interferometry with potassium	33
4.1	Laser cooling of potassium	33
4.1.1	Energy level structure of ^{39}K	34
4.1.2	Dual MOT performance	35
4.1.3	Sub-Doppler cooling	36
4.2	Fluorescence detection	38
4.3	Coherent manipulation	41
4.3.1	Stimulated Raman transitions	41
4.3.2	One-photon AC-Stark shift	45
4.3.3	Input state preparation	48
4.3.4	Influence of the ensemble temperature in a Doppler-sensitive transition	51
4.4	Measurements of local gravitational acceleration	55
4.4.1	Experimental methods	55
4.4.2	Suppression of phase shifts using the k -reversal method	55
4.4.3	Data analysis	57
4.5	Discussion	59

5	Testing the Universality of Free Fall with rubidium and potassium	63
5.1	Experimental methods	63
5.1.1	Data analysis	64
5.2	Analysis of systematic effects	66
5.2.1	One-photon light shift	66
5.2.2	Zeeman effect	67
5.2.3	Effective wave vector	68
5.2.4	Coriolis force	70
5.2.5	Two-photon light shift	71
5.2.6	Gravity gradient	72
5.3	Summary	72
6	Outlook	75
6.1	Overcoming current limitations	75
6.2	The future of matter wave tests of gravity	78
	Bibliography	81
	List of figures	97
	List of tables	99
	Appendix	101
A	Properties of ^{87}Rb and ^{39}K	101
B	^{39}K laser frequencies	103
C	Parameters used for the systematic uncertainty estimation	105
D	Radio frequency antenna	107

CHAPTER 1

Introduction

“Auch in den Lehrbüchern wird es gewöhnlich als etwas Naheliegendes und nicht besonders Hervorzuhebendes hingestellt, dass die Schwere, das Gewicht eines Körpers, seiner Masse proportional ist, unabhängig von dem Stoffe aus welchem er besteht. Und doch haben wir hier in Wahrheit zwei Eigenschaften, zwei Haupteigenschaften der Materie vor uns, die völlig unabhängig voneinander gedacht werden können und die sich durch die Erfahrung und nur durch diese als völlig gleich erweisen. Diese Übereinstimmung ist also vielmehr als ein wunderbares Rätsel zu bezeichnen, sie bedarf einer Erklärung.”

— H. HERTZ, 1884 [1]

A Theory of Everything

At the beginning of the 20th century, two central theories were developed that form the foundation of modern physics as we know it today. On the one hand, the brilliant findings of physicists including EINSTEIN, DE BROGLIE, HEISENBERG, SCHRÖDINGER, BORN, PAULI, and many others lead to the development of quantum mechanics [2–9]. Previously unanswered questions, that could be as simple as “*Why is water transparent?*” were finally resolved by understanding absorption and emission spectra with the aid of this framework. As an example, over the following decades continuing work led to a full description of the hydrogen atom and its spectrum. As it is the simplest atomic system, precision spectroscopy of its transitions [10, 11] has ever since evolved into one of the most fruitful testbeds of quantum mechanics as well as theories based on its foundation. On the other hand, in 1916 EINSTEIN established the theory of general relativity [12]; a metric theory of gravity. Although the gravitational attraction of two protons of masses m_p with distance r compared to the COULOMB repulsion of their charges e [13]

$$\frac{F_{\text{grav}}}{F_{\text{elec}}} = \frac{G m_p^2 / r^2}{e^2 / (4\pi \epsilon_0 r^2)} = \frac{G m_p^2}{e^2 / (4\pi \epsilon_0)} \approx 10^{-36} \quad (1.1)$$

with G being the gravitational constant and ϵ_0 the dielectric constant, is by far weaker, the importance of gravity on a cosmological scale becomes obvious when considering that the universe is electrically neutral¹ and at the same time there is no anticharge to screen mass. Applying EINSTEIN’S theory of general relativity made it possible to understand the geometry of spacetime

¹ Due to the strong and long-ranging COULOMB interaction, macroscopic charges quickly neutralize each other.

that explains the physics of cosmology, as well as the majority of astronomical observations in our solar system and beyond, such as binary systems and black holes [14]. Further, gravitational phenomena, such as the gravitational redshift, could be explained. Equally important, a variety of predictions were inferred with one of the most popular ones being gravitational waves [15] whose direct observation¹ is still an ongoing quest [17–19].

To create a universal “theory of everything” [20] that combines all four fundamental interactions², it is necessary to assure compatibility of the underlying theories. As of today, both, quantum mechanics and general relativity, have been confirmed in a large number of experiments probing the validity of these theories at outstanding precision³. If both theories are valid, they have to hold for all phenomena as a direct consequence. Unfortunately, no attempt to express a unified theory of “quantum gravity”, that is consistent over all energy scales, has succeeded thus far [28]. In addition to the current incompatibility of general relativity and quantum mechanics, the nature of dark matter and dark energy [28] remain to be explained⁴. These circumstances lead to the necessity of extensions of at least one of the theories to enable a unified theory of “quantum gravity” on all energy scales.

Tests of Einstein’s Equivalence Principle

The foundation of general relativity is constituted by EINSTEIN’S equivalence principle (EEP) that itself contains three postulates [14, 28, 30]:

1. Local Position Invariance

All comoving clocks relying on non-gravitational physics measure identical proper times⁵ when propagating along the same world lines in a gravitational field, implying a universality of the gravitational redshift.

2. Local Lorentz Invariance

The speed of light is constant, and no local non-gravitational experiment can distinguish a local reference frame from another one.

3. Universality of Free Fall

In the absence of other forces, all bodies, located at the same space-time point, experience the same acceleration in a gravitational field independently of their composition when neglecting self-gravity.

Einstein’s equivalence principle has been confirmed in many experimental tests. Starting with the original experiments performed by POUND and REBKA [24], the universality of the gravitational redshift has been further investigated by clock comparisons both on ground and with one clock in space [25–27, 31–33]. Also the local LORENTZ invariance has been confirmed in numerous tests and analyses [34–36]. The universality of free fall (UFF), which is subject of this thesis, originates from the equality of inertial mass m_{in} and gravitational mass m_{gr} . The consequence that gravity, unlike any other fundamental interaction, acts on all bodies in the same manner

¹ Indirect proof for the existence of gravitational waves is deduced from the increase of the rotation frequency of binaries [16].

² Commonly, a “theory of everything” is referred to as a unification of the “grand unified theory” and gravitation.

³ Examples of seminal experiments testing quantum mechanics are given in Refs. [21–23]; examples of seminal tests of general relativity are published in Refs. [16, 24–27].

⁴ The Pioneer anomaly that is mentioned as a third question in Ref. [28] has recently been resolved [29].

⁵ The proper time is the motion-dependent time measured by a clock propagating on a world line between two events.

regardless of their gravitational charge has been described as a “*wonderful mystery*” in 1884 by HERTZ [1] and has come under scrutiny in numerous experiments ever since. Tests aiming to validate the UFF for test bodies A and B perform a null measurement of the EÖTVÖS ratio

$$\eta_{A,B} \equiv 2 \frac{g_A - g_B}{g_A + g_B} = 2 \frac{\left(\frac{m_{\text{gr}}}{m_{\text{in}}}\right)_A - \left(\frac{m_{\text{gr}}}{m_{\text{in}}}\right)_B}{\left(\frac{m_{\text{gr}}}{m_{\text{in}}}\right)_A + \left(\frac{m_{\text{gr}}}{m_{\text{in}}}\right)_B}, \quad (1.2)$$

where g_X is the gravitational acceleration of test body X . The EÖTVÖS ratio hence expresses the differential gravitational acceleration of two test masses divided by their mean acceleration. Equivalently, Equation (1.2) can be related to the difference of ratios of gravitational and inertial mass. A UFF violation yields $\eta_{A,B} \neq 0$ that can result from a difference of the gravitational and inertial mass $m_{\text{gr}}/m_{\text{in}} \neq 1$, or a fifth force coupling differently to the test bodies, or more specifically, to their constituent particles such as neutrons and protons.

Historically, tests of the UFF emerged from GALILEI’S thought experiment¹ in the 16th century of comparing the free fall of different cannon balls dropped from the leaning tower of Pisa. This kind of free fall tests is thus commonly referred to as GALILEAN tests. Similarly, a demonstration experiment was performed by dropping a hammer and a feather on the Moon during the Apollo 15 mission in 1971. The best tests of the UFF to date were performed in complementary ways: Monitoring the distance between Earth and Moon in free fall around the Sun by means of laser ranging, it was possible to constrain the normalized differential acceleration to $\eta_{\text{Earth,Moon}} = (-0.8 \pm 1.3) \times 10^{-13}$ [37, 38]; employing a torsion balance [39, 40] with beryllium and titanium test masses, experiments performed by the group of ADELBERGER constrained $\eta_{\text{Be,Ti}} = (0.3 \pm 1.8) \times 10^{-13}$ [41]. The best GALILEAN test has been performed using a laser interferometer to read out the free fall of two test masses built of copper and uranium and found $\eta_{\text{Cu,U}} = (1.3 \pm 5.0) \times 10^{-10}$ [42]. Furthermore, numerous initiatives are currently developing new projects that are based on astronomical observations [43, 44] and GALILEAN tests in space [45] aiming to further improve the bounds on UFF violations. All of the aforementioned tests have in common that they employ classical, macroscopic bodies as test masses. In addition

Table 1.1: Overview of performed matter wave tests of the UFF.

Experiment	Ref.	A	B	$\eta_{A,B}$
Palo Alto	[46] ^a	¹³³ Cs	SiO ₂	$(7.0 \pm 7.0) \times 10^{-9}$
Paris	[47] ^a	⁸⁷ Rb	SiO ₂	$(4.4 \pm 6.5) \times 10^{-9}$
München	[48]	⁸⁵ Rb	⁸⁷ Rb	$(1.2 \pm 1.7) \times 10^{-7}$
Palaiseau	[49]	⁸⁵ Rb	⁸⁷ Rb	$(1.2 \pm 3.2) \times 10^{-7}$
Firenze	[50]	⁸⁷ Sr	⁸⁸ Sr	$(0.2 \pm 1.6) \times 10^{-7}$
Hannover	[51] ^b	³⁹ K	⁸⁷ Rb	$(0.3 \pm 5.4) \times 10^{-7}$

^a This semi-classical experiment compared the free fall of cold atoms to that of a falling corner cube.

^b The experiment is presented in this thesis.

¹ The experiments GALILEI actually performed were regarding investigations of “falling” bodies on an inclined plane.

to classical tests, the UFF can also be tested with quantum objects as first demonstrated by COLELLA, OVERHAUSER, and WERNER in 1975 [52]. In these experiments, which are based on the interference of massive particles such as neutrons or atoms, the gravitationally induced phase shift imprinted on a particle’s wave function is either compared to a classical gravimeter [46, 47], or to that of a second quantum object. A variety of tests based on matter wave interferometry have been performed comparing different rubidium [48, 49, 53] and strontium [50] isotopes, and have recently been extended to tests of two different chemical elements, rubidium and potassium [51], as presented in this thesis (Table 1.1). In order to increase the gravitationally induced phase shift, there are experiments proposed in large-scale fountains on ground [54–56] and for microgravity [57–60] aiming to increase the free fall time and thus the sensitivity to accelerations.

Quantum mechanical tests of the UFF differ from classical ones in various aspects, thus qualitatively different results are expected:

1. Set of test masses

Torsion balance experiments are typically restricted to the use of conducting, non-magnetic solids as test masses [61]. As discussed below, depending on the underlying theory, the choice of test masses directly influences the sensitivity to a UFF violation. By providing a number of species that can be laser-cooled [62, 63], matter wave tests extend the set of test masses for UFF experiments with highest isotopic purity, thus provide new linear combinations when searching for violation of the UFF [64, 65].

2. Spin-gravity coupling

Ensembles employed in matter wave tests are naturally spin-polarized and thus allow to investigate effects of spin-gravity coupling [28, 48, 50, 66–68]. When utilizing macroscopic test masses, spin-polarization is only possible in rare cases [69].

3. Test mass coherence length

The coherence length of quantum objects specifically is different to the one of macroscopic masses by orders of magnitude. This allows to investigate UFF-violating modifications of quantum mechanics, for example as a cause of space-time fluctuations [70].

4. Test duality

Atomic ensembles can be employed as UFF test masses as well as atomic clocks [71]. Thus, a single system is able to test both the UFF and the universality of the gravitational redshift¹.

Frameworks that are able to quantify violations of Einstein’s equivalence principle² are for example given by the dilaton scenario [74], and the standard model extension [64, 75–80], which parametrizes violations of LORENTZ invariance and related violations of the EEP. In the framework of the standard model extension, a simplified approach allows to express EEP violations of neutral matter in terms of five parameters which are all zero if the EEP holds. One of the five describes electronic EEP violation [64] and is well constrained by local LORENTZ invariance [34–36] and redshift experiments [24–27, 31–33]. Two of the remaining four parameters express EEP violations due to neutron excess of the test nuclei and their total baryon number.

¹ It should be pointed out, however, that the technical requirements of atomic clocks and matter wave interferometers are quite different.

² In specific, such a theory allows to compare EEP tests with respect to their sensitivity to a violation and their test mass choices.

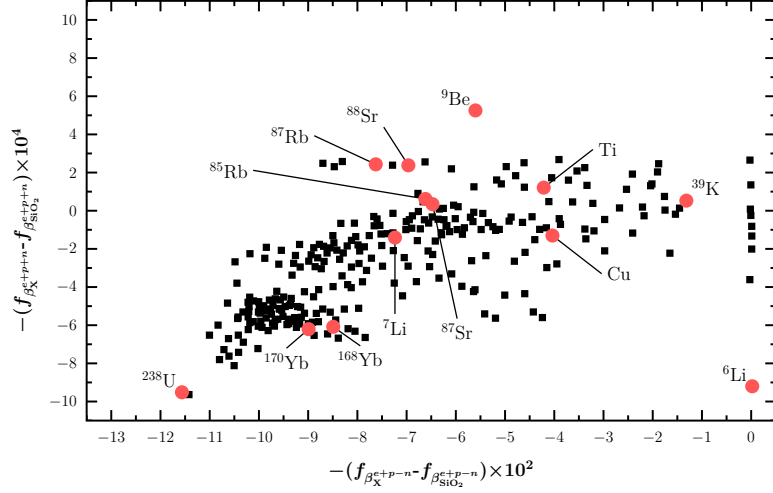


Figure 1.1: Comparison of test masses X with respect to SiO_2 analyzed in the standard-model extension. The sensitivity factors $f_{\beta_X^{e+p-n}}$ (neutron excess) and $f_{\beta_X^{e+p+n}}$ (baryon number) for species X are calculated according to Ref. [64]. Relevant nuclide data is taken from Ref. [72]. A larger separation of two species corresponds to a larger anomalous acceleration and thus higher sensitivity to violations of the EEP. For Ti and Cu natural occurrence of isotopes [73] is assumed.

The last two are a measure for the impact of EEP tests using bound systems of normal matter on the antimatter sector [64]. As an example of an application of the standard model extension, the sensitivity factors for the normal matter violation parameters β_X^{e+p-n} (neutron excess parameter) and β_X^{e+p+n} (baryon number parameter) are calculated for long-lived nuclides according to Ref. [64] in Figure 1.1. Here, a large separation of two test masses corresponds to a large anomalous acceleration and thus higher sensitivity to violations of the EEP. Different test mass pairs probe different linear combinations of EEP violations of their constituent particles neutrons, protons, and electrons. An EEP test with a new test mass pair that is significantly different from existing tests, such as rubidium and potassium in this thesis, has a great potential in influencing the results on the global bounds of EEP violations. This holds even for the case that the measurement accuracy does not exceed the one of the best existing tests [65].

Scope of this thesis

A violation of the universality of free fall remains the most likely candidate to unveil a microscopic theory enabling a unification of quantum mechanics and general relativity. Matter wave interferometers provide a novel and complementary method to test the universality of free fall due to their unique features and an extended set of test masses. Specifically, the test mass combination of rubidium and potassium provides an interesting complementarity to the existing torsion balance experiments with respect to the violation parameters in the standard model extension. While rubidium matter wave interferometers are operated by many groups all over the world, no potassium interferometer has been realized prior to the work of this thesis.

This thesis is organized as follows. An introduction into the theoretical formalism describing matter wave interferometry based on stimulated RAMAN transitions, and the analysis and comparison of test mass pairs is given in **Chapter 2**. The experimental setup is described in **Chapter 3**. In **Chapter 4** an overview over the techniques necessary to perform matter wave interferometry with potassium is provided and the obtained potassium single species performance are presented. **Chapter 5** analyzes the performed quantum test of the universality of free fall using rubidium

and potassium and its underlying systematic effects in detail. This thesis is closed with an outlook concerning possible improvements of the presented apparatus and a look into the future of matter wave tests of the universality of free fall in **Chapter 6**.

CHAPTER 2

Theoretical description of methods

“Unstreitig wäre es ein Fehler, aus den chemischen Bestandteilen des Weizenkorns die Gestalt der Ähre erforschen zu wollen, die es treibt, da man nur aufs Feld zu gehen braucht, um die Ähren fertig zu sehen. Untersuchung und Beobachtung, Philosophie und Erfahrung dürfen nie einander verachten noch ausschließen; sie leisten einander gegenseitige Bürgschaft.”

— C. VON CLAUSEWITZ, ~1830 [81]

In this Chapter, a description of the underlying theory relevant for this thesis is provided. In Section 2.1, an overview on the theoretical description of matter wave interferometry is elaborated. In Section 2.2 this Chapter closes with a description of two frameworks, which are capable of comparing the choice of test masses in an experiment testing the universality of free fall.

2.1 Brief theoretical description of matter wave interferometry

This Section briefly reviews the central formalism needed to theoretically describe matter wave interferometer. A detailed derivation can for example be found in Ref. [82]. Based on the time evolution of a two-state system induced by the interaction with an electromagnetic field, the beam splitting process is explained in Section 2.1.1. Afterwards, the inertial-sensitive MACH-ZEHNDER geometry [83] and its leading order phase shift are described in Section 2.1.2, and the sensitivity formalism, which allows to translate perturbations of the two-state system into interferometer phase contributions, is introduced in Section 2.1.3.

2.1.1 Beam splitting process

Beam splitters for matter waves can for example be realized by utilizing mechanical gratings, or electromagnetic waves [84, 85]. While the coherent electromagnetic coupling can be realized using single photon electric or magnetic dipole transitions, the following assessment is treating stimulated two-photon RAMAN transitions¹, in which the absorption of a photon of field ω_1 is followed by stimulated emission into the field ω_2 as indicated in Figure 2.1. The time evolution of the internal degrees of freedom of a two-state system $|g\rangle$ and $|e\rangle$ with energies $\hbar\omega_g$ and $\hbar\omega_e$, separated by $\omega_{12} \equiv \omega_e - \omega_g$ and amplitudes $c_e(t)$ and $c_g(t)$,

$$|\psi(t)\rangle = c_e(t) |e\rangle + c_g(t) |g\rangle, \quad (2.1)$$

¹ The formalism is very similar when using a different beam splitting method, e.g. BRAGG diffraction [86, 87].

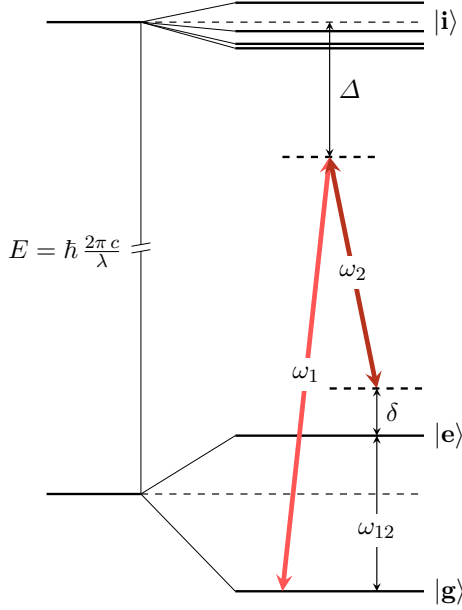


Fig. 2.1: Coherent two-photon transition coupling the states $|g\rangle$ and $|e\rangle$ with energies $\hbar\omega_g$ and $\hbar\omega_e$ at a detuning Δ to the intermediate state $|i\rangle$. The laser frequencies are ω_1 and ω_2 , and their detuning from resonance $\delta = \omega_1 - \omega_2 - \omega_{12}$. The transition wavelength to the intermediate state is $\approx \lambda$.

Here, $\delta = \omega_1 - \omega_2 - \omega_{12}$ accounts for any detuning with respect to the two-photon resonance, e.g. due to light shifts or the DOPPLER shift.

Figure 2.2 shows the time evolution of the RABI oscillations with the system initially prepared in state $|g\rangle$ at time $t = 0$. A RAMAN pulse coupling the two-state system for a duration of $t = \pi/(2\Omega_{\text{eff}}) \equiv \tau_{\pi/2}$ creates a coherent superposition

$$|\psi(\tau_{\pi/2})\rangle = \frac{1}{\sqrt{2}} (|e\rangle + |g\rangle), \quad (2.7)$$

and is called a “ $\pi/2$ -pulse”. Accordingly, a pulse fulfilling $t = \pi/(\Omega_{\text{eff}}) \equiv \tau_{\pi}$ is called “ π -pulse”, and transfers the system into the state $|e\rangle$.

The assessment above exclusively treats the system’s internal degree of freedom. However, due to the photon momentum $p = \hbar k$ that is exchanged during the absorption and emission process, the external degree of freedom of the system has to be analyzed as well. A light field at frequency

when coherently coupled by an electromagnetic field \vec{E} with a corresponding HAMILTONIAN

$$\hat{H} = \hbar\omega_e |e\rangle\langle e| + \hbar\omega_g |g\rangle\langle g| - \hat{d} \cdot \vec{E}, \quad (2.2)$$

where \hat{d} is the dipole operator, and spontaneous emission is neglected, can be derived by solving the SCHRÖDINGER equation [82]. The result is the RABI formula¹ [82]

$$P_e(t) = |c_e(t)|^2 = \left[\frac{\Omega_0}{\Omega_{\text{eff}}} \sin\left(\frac{\Omega_{\text{eff}} t}{2}\right) \right]^2, \quad (2.3)$$

giving the time dependent population probability of state $|e\rangle$. Here, the effective RABI frequency Ω_{eff} is depending on the resonant RABI frequency

$$\Omega_0 = \frac{\Omega_1 \Omega_2^*}{2\Delta}, \quad (2.4)$$

in which Δ is the RAMAN laser detuning, and the related single light field RABI frequencies

$$\Omega_j = \Gamma \sqrt{\frac{I_j}{I_{\text{sat}}}}, \quad (2.5)$$

with the light field intensities I_j , the natural linewidth Γ , and the saturation intensity I_{sat} [82, 88]. The effective RABI frequency is [82]

$$\Omega_{\text{eff}} = \sqrt{\Omega_0^2 + \delta^2}. \quad (2.6)$$

¹ In Equation (2.3), the system is in state $|g\rangle$ at time $t = 0$ without loss of generality. Furthermore, a large detuning $|\Delta| \gg \Gamma$ is assumed allowing to neglect single photon transitions and related decoherence processes.

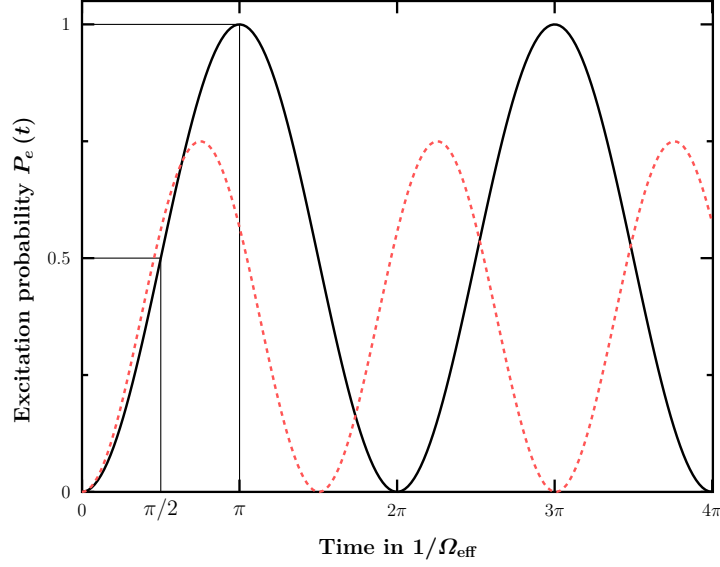


Figure 2.2: Ideal RABI oscillations $P_e(t)$ with the system initially prepared in state $|g\rangle$, plotted for a resonantly driven system (solid black line) and a small detuning δ (red dashed line). For the resonant case, the conditions $t = \pi/(2\Omega_{\text{eff}}) \equiv \tau_{\pi/2}$ (“ $\pi/2$ -pulse”) and $t = \pi/(\Omega_{\text{eff}}) \equiv \tau_{\pi}$ (“ π -pulse”) are marked.

ω_j can be assigned the wave vector

$$k_j = \frac{\omega_j}{c}, \quad (2.8)$$

where c is the speed of light. Accordingly, the effective wave vector

$$k_{\text{eff}} \equiv k_1 - k_2, \quad (2.9)$$

for the two-photon transition in Figure 2.1. While for copropagating fields ω_1 and ω_2 , $k_{\text{eff}} \approx 0$, counterpropagating light fields [83] (see Section 4.3) yield the effective wave vector

$$k_{\text{eff}} = \frac{\omega_1 + \omega_2}{c} \approx \frac{4\pi}{\lambda}, \quad (2.10)$$

in which λ is the transition wavelength, and the transferred two-photon momentum equals

$$p = \hbar k_{\text{eff}}. \quad (2.11)$$

The related recoil velocity [88]

$$v_{\text{rec}} = \frac{\hbar k_{\text{eff}}}{m}, \quad (2.12)$$

and the recoil frequency [88]

$$\omega_{\text{rec}} = \frac{\hbar k_{\text{eff}}^2}{2m}, \quad (2.13)$$

which corresponds to the DOPPLER shift induced by the momentum change.

The two-photon light field couples the states $|g, p\rangle \rightarrow |e, p + \hbar k_{\text{eff}}\rangle$ in a system initially prepared in state $|g, p\rangle$ with momentum p . In the following Section, it will be shown how this interaction can be used as “beam splitters” and “mirrors” for matter waves, which allow to realize interferometer geometries.

2.1.2 Mach-Zehnder geometry

The “separated oscillating fields” method [89], which was introduced by RAMSEY, allowed to significantly increase the resolution of transition frequency measurements. This was made possible by extending a single FOURIER transform-limited electromagnetic pulse interrogation with a second pulse applied after an evolution time, and thus effectively creating a $\pi/2$ - $\pi/2$ -interferometer, which allowed to identify the transition frequency in an interference fringe pattern at a much higher resolution than the FOURIER-broadened line did.

Measuring gravitational acceleration with matter waves can be understood as an interferometric spectroscopy of the gravitationally induced DOPPLER shift of a matter wave with respect to the beam splitting field. In general, the DOPPLER shift ω_D experienced by a particle with velocity v in a field with wave vector k is

$$\omega_D = k \cdot v. \quad (2.14)$$

In a constant gravitational field, a particle’s velocity $v = g \cdot t + v_0$. Without loss of generality, the initial velocity can be set $v_0 = 0$. In a two-photon light field with wave vector k_{eff} , the DOPPLER shift

$$\omega_D(t) = k_{\text{eff}} \cdot g \cdot t, \quad (2.15)$$

$$\Leftrightarrow \alpha_D \equiv \frac{\omega_D(t)}{t} = k_{\text{eff}} \cdot g, \quad (2.16)$$

can be assigned a rate α_D . A spectroscopy of the two-photon resonance spectrum after a free fall time t_{TOF} as performed in Section 4.3.1 allows to calculate the gravitational acceleration $g = \omega_D(t_{\text{TOF}})/k_{\text{eff}}$. In analogy to RAMSEY’S method, however, the resolution of this measurement can be vastly increased by extending the pulse sequence to a MACH-ZEHNDER geometry, which is the most common interferometer topology for measuring accelerations [83], by making use of the beam splitting mechanism as described above.

Figure 2.3 shows a MACH-ZEHNDER geometry consisting of a $\pi/2$ -, π -, and a $\pi/2$ -pulse separated by a pulse separation time T . Stimulated two-photon transitions driven by a field with wave

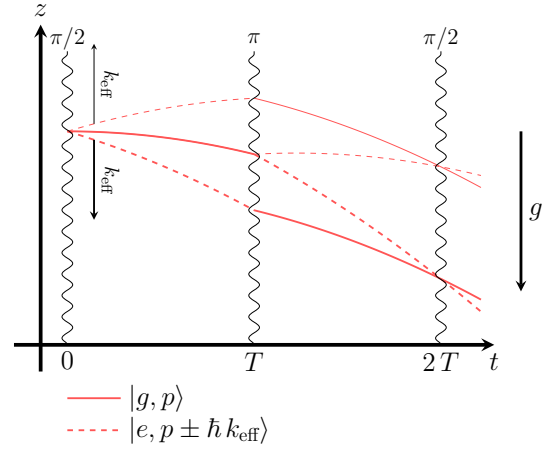


Fig. 2.3: Space-time diagram of a MACH-ZEHNDER matter wave interferometer in a constant gravitational field for the downward (thick lines) and upward (thin lines) direction of momentum transfer. Stimulated RAMAN transitions at times 0 , T , and $2T$ couple the states $|g, p\rangle$ and $|e, p \pm \hbar k_{\text{eff}}\rangle$. The velocity change induced by the RAMAN pulses is not to scale with respect to the gravitational acceleration.

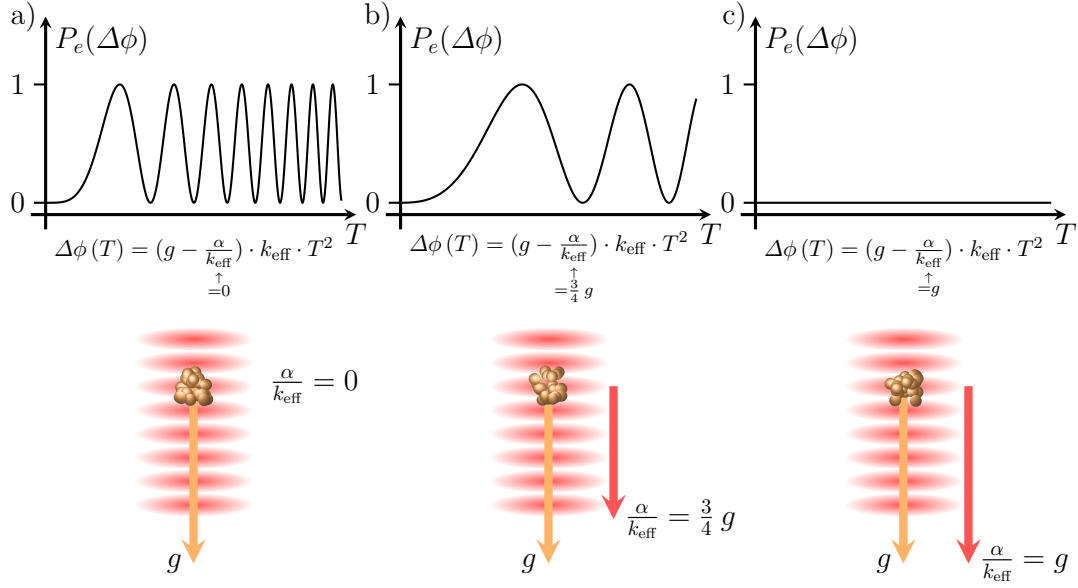


Figure 2.4: Compensating for the gravitationally induced phase shift utilizing effective RAMAN wavefront accelerations a) $\alpha/k_{\text{eff}} = 0$, b) $\alpha/k_{\text{eff}} = 3/4 \cdot g$, and c) $\alpha/k_{\text{eff}} = g$.

vector¹ k_{eff} coherently split, redirect, and recombine a matter wave by coupling the states $|g, p\rangle$ and $|e, p \pm \hbar k_{\text{eff}}\rangle$.

The normalized population of the excited state $|e\rangle$ in dependence of the phase shift $\Delta\phi$ between the interferometer arms is given by a typical fringe pattern

$$P_e(\Delta\phi) \propto \frac{A}{2} [1 - \cos(\Delta\phi)] + B. \quad (2.17)$$

Here, A is the fringe amplitude and B a measurement offset. For small phase noise, the population $P_e(\Delta\phi)$ is a bijective function and can the phase shift can be expressed as

$$\Delta\Phi = \arccos\left(\frac{P_e - B}{A}\right), \quad (2.18)$$

which finds its use for example when evaluating data that is acquires at a “midfringe” position with maximum slope [90].

An analysis up to higher orders of the arising phase shift $\Delta\phi$ is performed in Refs. [91, 92]. Here, the focus is laid on the leading order contribution. The phase acquired during light-matter interaction at time t_n due to a time-dependent frequency change is [82]

$$\phi_n = \int_{t_0}^{t_n} \omega(t') dt', \quad (2.19)$$

where any global phases are disregarded. Inserting the DOPPLER shift $\omega_D(t)$ induced by gravitational acceleration (Equation (2.15)) and summing over the three pulses applied in a

¹ Here, the two-photon light field is treated as a plane wave for simplicity. For deviations, see for example Section 5.2.3.

MACH-ZEHNDER geometry

$$\Delta\phi = \phi_1 - 2\phi_2 + \phi_3, \quad (2.20)$$

the leading order phase contribution

$$\Delta\phi = \vec{k}_{\text{eff}} \cdot \vec{g} \cdot T^2 \quad (2.21)$$

can be determined¹. Throughout this thesis, $\vec{k}_{\text{eff}} \parallel \vec{g}$ will be assumed, unless stated otherwise. Applying a linear frequency change rate α on the RAMAN laser difference frequency creates an effective acceleration

$$a \equiv \alpha/k_{\text{eff}} \quad (2.22)$$

of the RAMAN wavefronts. Thus, matching $\alpha = \alpha_D$ (Equation (2.16)) allows to null the gravitationally induced phase shift

$$\Delta\phi = \left(g - \frac{\alpha}{k_{\text{eff}}}\right) \cdot k_{\text{eff}} \cdot T^2, \quad (2.23)$$

and determine to g . This null measurement principle is further illustrated in Figure 2.4. Here, effective wavefront accelerations a) $\alpha/k_{\text{eff}} = 0$, b) $\alpha/k_{\text{eff}} = 3/4 \cdot g$, and c) $\alpha/k_{\text{eff}} = g$, lead to different dependencies on the pulse separation time T of the population of the excited state $|e\rangle$ at the interferometer output². In specific, in the case depicted in Figure 2.4 c), $\alpha = \alpha_D$, the phase shift is zero with the dependence on T fully lifted, and the interferometer's "central fringe" is determined (see Section 4.4 & Section 5.1).

2.1.3 Sensitivity formalism

As derived in detail in Ref. [93], sensitivity function $g_s(t)$, which describes the response of an interferometer output $\delta P_e(t, \delta\Phi)$ to an infinitesimal phase exertion $\delta\phi$ can be written as

$$g_s(t) \equiv 2 \lim_{\delta\Phi \rightarrow 0} \frac{\delta P_e(t, \delta\Phi)}{\delta\Phi}. \quad (2.24)$$

The sensitivity function can be used to determine interferometer phase shifts caused by any time dependent frequency change $\omega(t)$:

$$\Delta\Phi = \int_{-\infty}^{\infty} g_s(t) \omega(t) dt. \quad (2.25)$$

¹ The derivation of Equation (2.21) can also be understood as measuring the position of the matter wave with respect to the RAMAN wavefronts.

² "Overcompensating" the gravitational acceleration ($\alpha/k_{\text{eff}} > g$) reintroduces a dependency of the interferometer's output signal on the pulse separation time.

For a MACH-ZEHNDER interferometer with a pulse separation time T and a $\pi/2$ -pulse duration $\tau_{\pi/2}$, the sensitivity function $g_{s,\text{MZ}}(t)$ is the piecewise defined function [93]

$$g_{s,\text{MZ}}(t) = \begin{cases} -\sin(\Omega_{\text{eff}} t) & : 0 < t \leq \tau_{\pi/2} \\ -1 & : \tau_{\pi/2} < t \leq T + \tau_{\pi/2} \\ +\sin(\Omega_{\text{eff}}(t - T - 2\tau_{\pi/2})) & : T + \tau_{\pi/2} < t \leq T + 3\tau_{\pi/2} \\ +1 & : T + 3\tau_{\pi/2} < t \leq 2T + 3\tau_{\pi/2} \\ +\sin(\Omega_{\text{eff}}(t - 2T - 2\tau_{\pi/2})) & : 2T + 3\tau_{\pi/2} < t \leq 2T + 4\tau_{\pi/2} \\ 0 & : \text{otherwise} \end{cases} \quad (2.26)$$

It is evident, that the function $g_{s,\text{MZ}}(t)$ consists of two subsequent $\pi/2$ - $\pi/2$ RAMSEY interferometers with inverted phase sensitivity. Utilizing the sensitivity formalism, any external perturbation $d\phi(t)/dt = \omega(t)$ of the two-state system can be translated into an interferometer phase shift $\Delta\phi$. Hence, the formalism explained here is exploited for the systematic error analysis performed in Section 5.2. For example, inserting the DOPPLER shift $k_{\text{eff}} \cdot g \cdot t$ of an ensemble in free fall into Equation (2.25) with the sensitivity function $g_{s,\text{MZ}}(t)$ of a MACH-ZEHNDER interferometer yields the phase shift $k_{\text{eff}} \cdot g \cdot T^2$ (Equation (2.21)) with the assumption $\tau_{\pi/2} \ll T$. Moreover, the propagation of an ensemble in a varying external magnetic field causes a perturbation $\Delta\omega_{\text{clock}}$ (see Section 5.2.2) which, inserted in Equation (2.25) allows to derive the phase shift due to the external perturbation. Further, by adapting $g_s(t)$ such that it is nonzero only for the time during which beam splitting pulses are applied, the AC-STARK phase shift can be inferred (see Section 4.3.2).

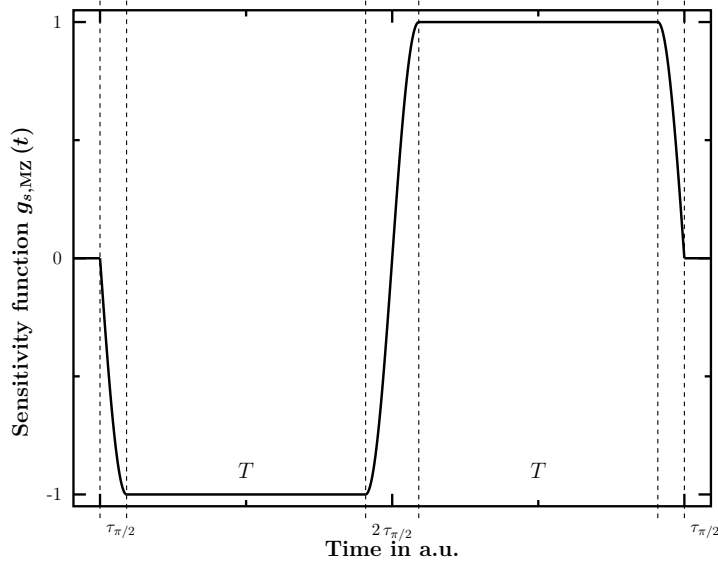


Figure 2.5: Sensitivity function $g_s(t)$ of a MACH-ZEHNDER interferometer with a pulse separation T and a $\pi/2$ -pulse duration $\tau_{\pi/2}$. Unlike in typical experiments, the pulse duration is exaggerated in comparison to the pulse separation time.

2.2 Quantifying violations of the Universality of Free Fall

Various test theories such as the gravitational standard model extension (SME) [64, 75–80] and specific violation scenarios [70, 74] exist that allow to derive quantitative predictions on the level at which a UFF would manifest. Moreover, test theories introduce violation parameters that

Table 2.1: Comparison of test masses A and B analyzed in the dilaton model. The charges $Q_X^{\prime 1}$ and $Q_X^{\prime 2}$ with X being either A or B are calculated according to Ref. [74]. A larger absolute number corresponds to a larger anomalous acceleration and thus higher sensitivity to violations of the EEP. For Ti and Cu natural occurrence of isotopes [73] is assumed.

A	B	Ref.	$Q_A^{\prime 1} - Q_B^{\prime 1}$ $\times 10^4$	$Q_A^{\prime 2} - Q_B^{\prime 2}$ $\times 10^4$
⁹ Be	Ti	[41]	-15.46	-71.20
Cu	²³⁸ U	[42]	-19.09	-28.62
⁸⁵ Rb	⁸⁷ Rb	[48, 49]	0.84	-0.79
⁸⁷ Sr	⁸⁸ Sr	[50]	0.42	-0.39
⁶ Li	⁷ Li ^a	[94]	0.79	-10.07
³⁹ K	⁸⁷ Rb	[51]	-6.69	-23.69

^a A UFF test comparing ⁶Li vs ⁷Li has not yet been performed.

can be constrained by taking account for existing UFF tests that have ruled out violations at a certain level.

In order to quantify violations of the UFF in a test theory, composition-dependent ‘‘charges’’ are assigned to test masses for the assumed UFF-violating interactions by assuming a different coupling of their constituents³. These charges can, for example, be proportional to the neutron excess and the overall baryon number in a given nucleus [95].

In the dilaton model [74], protons and neutrons may experience different accelerations. The EÖTVÖS ratio of test masses *A* and *B* can then be expressed as

$$\eta_{A,B} \sim D_1(Q_A^{\prime 1} - Q_B^{\prime 1}) + D_2(Q_A^{\prime 2} - Q_B^{\prime 2}). \quad (2.27)$$

Here, $Q_X^{\prime 1}$ and $Q_X^{\prime 2}$ represent effective charges of species X, and larger charges correspond to a larger anomalous acceleration. By obtaining bounds on the EÖTVÖS ratio $\eta_{A,B}$, the violation parameters D_1 and D_2 can be constrained accordingly.

Similarly, in the standard model extension [64], EEP violations of neutral matter are described in terms of five parameters, which are zero in the case that the EEP is valid. The EÖTVÖS ratio then is

$$\eta_{A,B} \sim \beta_A - \beta_B \quad (2.28)$$

with violation parameters

$$\beta_X \equiv f_{\beta_X^{e+p-n}} \beta^{e+p-n} + f_{\beta_X^{e+p+n}} \beta^{e+p+n} + f_{\beta_X^{\bar{e}+\bar{p}-\bar{n}}} \beta^{\bar{e}+\bar{p}-\bar{n}} + f_{\beta_X^{\bar{e}+\bar{p}+\bar{n}}} \beta^{\bar{e}+\bar{p}+\bar{n}} \quad (2.29)$$

that are assigned for species X. Again, the sensitivity factors $f_{\beta_X^{e+p-n}}$ ($f_{\beta_X^{\bar{e}+\bar{p}-\bar{n}}}$) and $f_{\beta_X^{e+p+n}}$ ($f_{\beta_X^{\bar{e}+\bar{p}+\bar{n}}}$) can be interpreted as charges proportional to the neutron excess and the overall baryon

³ For instance, in the analysis in the framework of the standard model extension performed in Ref. [64], based on violations of LORENTZ invariance, different couplings are assumed for electrons, protons, and neutrons.

number in a given normal matter (antimatter) nucleus [64]. An interesting feature arises from the SME: Due to an anomalous gravitational redshift in the energy of non-gravitationally bound systems of normal matter, constraints for UFF violations of free antiparticles can be derived from normal matter tests [64].

Table 2.1 shows the sensitivities of a selection of test mass pairs to UFF violations in the dilaton model. In general, a “good” test species pairs fulfills $m_A \gg m_B$ or vice versa, making the sensitivity of tests comparing isotopes worse than dual species experiments, however, in matter wave interferometers dual isotope experiments benefit greatly from common mode rejection and strongly suppressed systematics [49]. It is also worth noting, that for lighter isotopes such as ${}^6\text{Li}$ vs ${}^7\text{Li}$, the sensitivity $Q_{\text{Li-6}}^2 - Q_{\text{Li-7}}^2$ is enhanced as compared to heavier dual isotope tests due to the larger relative difference [74].

When analyzed in the SME, the same test mass combinations show qualitatively different sensitivities as shown in Table 2.2. Dual isotope tests show strongly suppressed sensitivities in both the matter and antimatter sector. Again, a ${}^6\text{Li}$ vs ${}^7\text{Li}$ comparison is the exception due to the large relative difference of the nuclei. In comparison to the torsion balance experiment using ${}^9\text{Be}$ vs Ti [41], a distinct complementarity to the test pair ${}^{87}\text{Rb}$ vs ${}^{39}\text{K}$, which is used in this thesis, is visible. While the torsion balance provides a high sensitivity to the baryon number parameter $f_{\beta_A^{e+p+n}} - f_{\beta_B^{e+p+n}}$, a rubidium vs potassium combination is more sensitive to the neutron excess parameter $f_{\beta_A^{e+p-n}} - f_{\beta_B^{e+p-n}}$. This complementarity also holds for the implications that can be derived for the antimatter sector.

The test mass pair used in the best GALILEAN test Cu vs ${}^{238}\text{U}$ [42] shows a remarkable sensitivity with respect to the neutron excess parameter and the baryon number parameter. Moreover, for the antimatter sector, a very high sensitivity to $f_{\beta_{\text{Cu}}^{\bar{e}+\bar{p}-\bar{n}}} - f_{\beta_{\text{U-238}}^{\bar{e}+\bar{p}-\bar{n}}}$ is given.

When analyzing existing UFF tests in the SME, the the UFF violation parameters are not constrained at the level of the best existing tests [64, 65]. Much rather, the global bounds suffer from the fact that most of the tests are strongly correlated. Conducting a UFF test with a new test mass combination, that is, with a new linear combination of violating gravitational

Table 2.2: Comparison of test masses A and B analyzed in the standard-model extension. The sensitivity factors $f_{\beta_X^{e+p-n}}$, $f_{\beta_X^{e+p+n}}$, $f_{\beta_X^{\bar{e}+\bar{p}-\bar{n}}}$, and $f_{\beta_X^{\bar{e}+\bar{p}+\bar{n}}}$ with X being either A or B are calculated according to Ref. [64]. Relevant nuclide data is taken from Ref. [72]. A larger absolute number corresponds to a larger anomalous acceleration and thus higher sensitivity to violations of the EEP. For Ti and Cu natural occurrence of isotopes [73] is assumed.

A	B	Ref.	$f_{\beta_A^{e+p-n}} - f_{\beta_B^{e+p-n}}$ $\times 10^2$	$f_{\beta_A^{e+p+n}} - f_{\beta_B^{e+p+n}}$ $\times 10^4$	$f_{\beta_A^{\bar{e}+\bar{p}-\bar{n}}} - f_{\beta_B^{\bar{e}+\bar{p}-\bar{n}}}$ $\times 10^5$	$f_{\beta_A^{\bar{e}+\bar{p}+\bar{n}}} - f_{\beta_B^{\bar{e}+\bar{p}+\bar{n}}}$ $\times 10^4$
${}^9\text{Be}$	Ti	[41]	1.48	-4.16	-0.24	-16.24
Cu	${}^{238}\text{U}$	[42]	-7.08	-8.31	-89.89	-2.38
${}^{85}\text{Rb}$	${}^{87}\text{Rb}$	[48, 49]	-1.01	1.81	1.04	1.67
${}^{87}\text{Sr}$	${}^{88}\text{Sr}$	[50]	-0.49	2.04	0.81	1.85
${}^6\text{Li}$	${}^7\text{Li}$ ^a	[94]	-7.26	7.79	-72.05	5.82
${}^{39}\text{K}$	${}^{87}\text{Rb}$	[51]	-6.31	1.90	-62.30	0.64

^a A UFF test comparing ${}^6\text{Li}$ vs ${}^7\text{Li}$ has not yet been performed.

interaction coupling to their constituents, thus allows to further constrain the global bounds even though the sensitivity of the new test might be lower than state-of-the-art. As an example, the pair ^{87}Rb vs ^{39}K is significantly different from all existing tests to allow for an improvement of the SME bounds for neutral matter by two orders of magnitude when performing a comparison at a level of $\approx 10^{-11}$ [65].

CHAPTER 3

Experimental setup

“Hofstadter’s Law: It always takes longer than you expect, even when you take into account Hofstadter’s Law.”

— D. R. HOFSTADTER, 1979 [96]

This Chapter is devoted to the description of the parts of the experimental setup which were used to obtain the results of this thesis related to matter wave interferometry with potassium. The apparatus is designed to enable free fall experiments with a maximum free evolution time of ≈ 200 ms. It is based on a two stage approach in which a three-dimensional magneto-optical trap (3D MOT) [97, 98] is loaded from a transversely cooled atomic beam generated in a two-dimensional magneto-optical trap (2D MOT) [99–101], thus enabling a high repetition rate of the experiment. Moreover, use of a differential pumping tube allows to produce high source vapor pressures in the 2D MOT chamber while maintaining ultra-high vacuum outside of it.

The vacuum system and peripheral installations described in Section 3.1 have been explained in previous theses [90, 102] and are not covered in detail. Similarly, the description of the rubidium part of the apparatus, which is described well in Ref. [90], is reduced to the optical setup that is common to both species. The description in this thesis is rather focused on the laser system necessary for cooling, trapping (see Section 3.2.1), and coherent manipulation (see Section 3.2.3) of potassium which lie at the heart of the performed experiments. In Section 3.3, the Chapter closes with a summary focused on the installed peripheral optics for RAMAN beam shaping and alignment, and the state-selective fluorescence detection system.

3.1 Vacuum system and peripheral installations

The vacuum system [90, 102] (Figure 3.1) consists of three major elements: the chambers for the (i) 2D MOT and (ii) 3D MOT, and (iii) the falling tube with a high numerical-aperture detection zone attached. The chamber is pumped using an ion getter pump [Gamma Vacuum, TiTan-IGP, 401/s] and a titanium sublimation pump [VG-Scienta, ZST23] and its pressure, which typically lies in the region of $\approx 7 \times 10^{-10}$ mbar in the 3D MOT section, is monitored with a cold cathode gauge [Vacuum Generators, ZCR40R]. With its 20 indium-sealed viewports the 3D MOT vacuum chamber features good optical access while maintaining a certain robustness as compared to glass cell-based systems. In the horizontal plane the 3D MOT chamber features two large viewports with 7 cm diameter and four smaller ones with 1.5 cm diameter. During construction of the vacuum chamber, great care was taken to choose materials that are non-magnetic to a large extent: The parts machined in-house, i.e. the lead-sealed MOT chambers, the falling tube, and the detection zone are made of aluminum; Commercial, copper-flange sealed vacuum parts, e.g.

connecting the dual MOT chamber with the pumping section and the vapor source¹, are made of non-magnetic A4-type stainless steel. The complete vacuum system with exception of the ion getter pump is housed inside a magnetic shield to suppress the influence of external magnetic stray fields. On the inside of the magnetic shield, compensation coil pairs are installed in the shield's mounting frame for all three axes to provide the possibility to null residual magnetic fields inside the shield.

3.1.1 Vertical magnetic bias field

A key element for realizing matter wave interferometry is a magnetic bias field. It creates a quantization axis and thus allows to define optical polarizations, granting selection of certain two-photon transitions (see Section 2.1). Moreover, by lifting the degeneracy of m_F states it becomes possible to work with atoms prepared in the $m_F = 0$ state that is not susceptible to the linear ZEEMAN effect. The vertical bias magnetic field is as well used to enable cycling transitions during fluorescence detection (see Section 4.2).

The quantization field is generated using a coil pair in HELMHOLTZ configuration (Figure 3.1) that is mounted around the 3D MOT chamber and the falling tube. The TAYLOR series for the axial magnetic field of a pair of coils with radius R and distance D driven with current I in

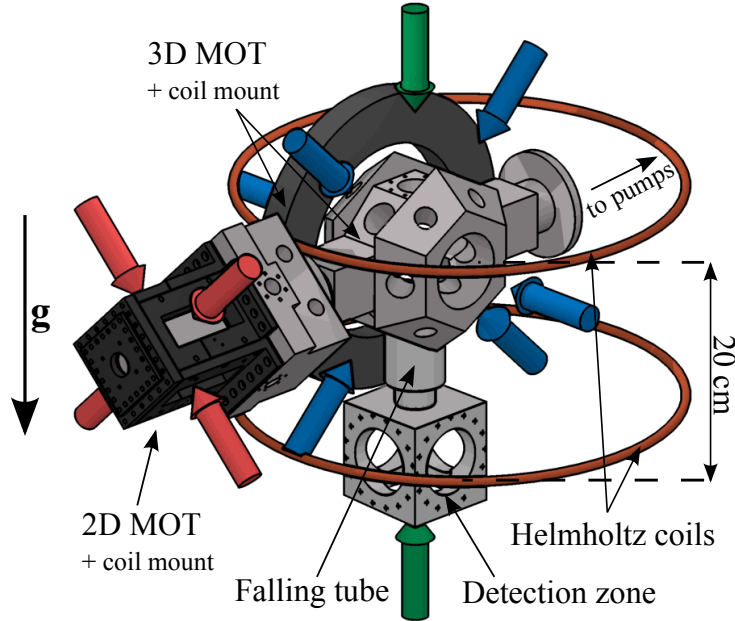


Figure 3.1: Vacuum system with the 2D MOT and 3D MOT chambers, and their magnetic coil mounts, the falling tube, and detection zone as employed in the experiment. In addition, the Helmholtz coil pair generating the quantization magnetic field for the RAMAN beam splitting is shown. For better visibility, one 3D MOT coil, all optical collimators, the rubidium and potassium vapor sources, and the vacuum pumps have been omitted. Colored arrows indicate the light axes of the 2D MOT (red), the 3D MOT (blue), and the RAMAN beam splitting light (green). The falling distance from the 3D MOT geometric center to the detection zone is approximately 20 cm, allowing for a maximum free fall time of ≈ 200 ms.

¹ The potassium vapor source is kept at a constant temperature of ≈ 65 °C. At this temperature, potassium is near its melting point and has a vapor pressure just below $\approx 1 \times 10^{-6}$ mbar [103].

cylindrical coordinates to $\mathcal{O}(3)$ near the origin is [104]

$$B_z(\rho, z) = \mu_0 I \left(\frac{R^2}{(D^2/4 + R^2)^{3/2}} + \frac{3}{2} \frac{R^2(D^2 - R^2)}{(D^2/4 + R^2)^{7/2}} \left(z - \frac{\rho^2}{2} \right) \right). \quad (3.1)$$

In the HELMHOLTZ configuration, $R = D$ and Equation (3.1) is reduced to

$$B_z(\rho, z) = \mu_0 I \frac{8}{5\sqrt{5}R}, \quad (3.2)$$

with the vacuum permeability μ_0 . Hence a HELMHOLTZ coil pair shows no dependency of the vertical or radial position near the origin and generates an ideal homogeneous magnetic field in the direction of z .

The coil pair used in this thesis has a coil radius and distance of $R = D = 20$ cm, and $n = 8$ windings. Various spatial constraints imposed by the vacuum chamber and peripheral installations are taken into account. A vertical distance from the 3D MOT center up to the upper solenoid of 4 cm is kept and the lower coil does not block optical access to the detection zone. Moreover, the coil pair is not centered radially around the falling tube as the presence of the 2D MOT chamber requires a few centimeters offset. The homogeneous magnetic field region allows for a total free fall time from the 3D MOT center to the edge of the lower coil of 180 ms. Substituting $I \rightarrow nI$ in Equation (3.2) for a coil pair with n windings per solenoid, the coil pair yields $B_z(I) = 360$ mG/A.

3.1.2 Radio-frequency manipulation

Inducing ground state electron spin flips in alkali atoms by magnetic dipole interaction [105], ideally with RABI frequencies on the order of a few kilohertz, is a valuable tool to manipulate atomic systems, e.g. for initial state preparation and purposes of system characterization. The ground state hyperfine energy splitting of rubidium corresponds to wavelengths on the order of centimeters. When using metal vacuum chambers, as in this thesis, instead of glass cells, placing microwave antennas close to the atoms can be a challenge due to missing physical access. Moreover, even when placing an antenna at a certain distance outside a metal vacuum chamber viewport, the bore will act as a waveguide¹. Here, the cutoff frequency, that is, the lowest frequency for waves to propagate in the waveguide, for the lowest order transverse magnetic modes [106]

$$\omega_c(r_v) = c \frac{\chi_{0,1}}{r_v} = c \frac{2.4048}{r_v}, \quad (3.3)$$

where $\chi_{0,1}$ is the first root of the BESSEL function $J_0(r_v)$, and r_v the radius of the bore. Consequently, when interpreted as an ideal circular waveguide, the largest available viewport with a bore radius of 3.5 cm imposes a cutoff frequency of $\omega_c(3.5 \text{ cm}) = 3.28$ GHz.

The rubidium hyperfine energy splitting is 6.834 GHz [107]. As this makes the minimum radius of a viewport 1.7 cm, microwave manipulation of rubidium is a straightforward technique².

¹ Strictly speaking, the “depths” of the bores in the vacuum chambers are on the order of only a few wavelengths or less and thus not sufficient to form an ideal waveguide. The approach chosen here thus only provides an estimate for the transmission of electromagnetic radiation through vacuum viewports.

² In fact, the viewport used in the experiment has a radius of 1 cm, just below the cutoff radius. However, no dramatic attenuation effects were observed.

Driving simple loop antennas with sufficient power (≈ 30 dBm) at the antenna in the case of this thesis easily makes kilohertz RABI frequencies feasible. The situation is different when working with bosonic potassium. ^{39}K , which is used in this thesis, has a ground state hyperfine splitting of only 461.7 MHz (see Section 4.1.1) with an associated wavelength of ≈ 65 cm. The hyperfine transition frequency thus lies significantly below the cutoff frequency of the largest available viewports. Consequently, manipulating the atomic spin system is only possible using the evanescent electromagnetic field that reaches into the center region of the 3D MOT chamber.

In the scope of this thesis, two types of antennas were built and tested: a half-wave dipole antenna [108] and a three-element YAGI-UDA antenna [109]. Figure 3.2 a) shows the schematic of a dipole antenna and a radiation diagram in dependence of the angle θ measured from the dipole axis. The radio frequency (RF) is generated by a synthesizer [Giga-tronics 6082A] that is amplified [Mini-Circuits ZHL-1-2W-S] as depicted in Figure 3.3. The amplifier input can be pulsed by two¹ radio frequency switches [Mini-Circuits ZY5WA-2-50DR] in series and the amplifier is protected against back reflections through a circulator [UTE Microwave CT-1501-S] with its third connector shortened via a $50\ \Omega$ load. When pulsed, the setup provides +28 dBm at the antenna and -60 dBm when switched off. For the comparison of antennas, the gain factor G [106] is a good figure of merit. It can be determined by calculating the ratio of the power irradiated per solid angle into the direction of maximum directivity to, e.g., that of an ideal, isotropic radiator. Using

$$G_{\text{dBi}} = 10 \cdot \log_{10}(G) \quad (3.4)$$

for the half-wave dipole antenna, in which $l_{\text{de}} \approx \lambda/2$ and $G(\text{dip}) = 1.65$, one finds $G_{\text{dBi}} = 2.18$ dBi. In turn, the three-element YAGI-UDA antenna displayed in Figure 3.2 b) with the dimensions

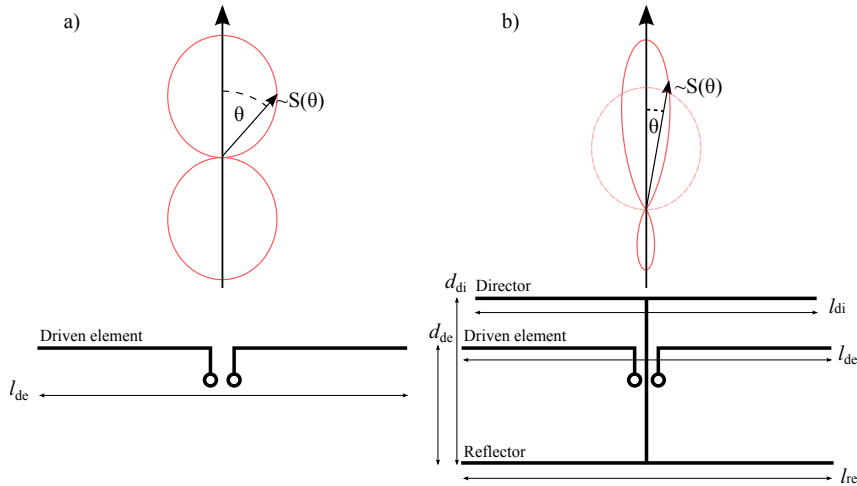


Figure 3.2: Schematics of a) a dipole antenna and b) a three-element YAGI-UDA antenna with characteristic lengths l_x , spacings d_x , and their corresponding radiation diagrams with the irradiated power S per solid angle in dependence of the angle θ measured from the dipole axis. In b), the dashed circle in the radiation diagram compares the directivity to that of a dipole antenna. The dipole antenna consists of a **driven element**, the YAGI-UDA antenna combines a **driven element** with passive **director** and **reflector** elements creating directivity due to interference.

¹ Using only one RF switch, a measurable residual background radiation was observed.

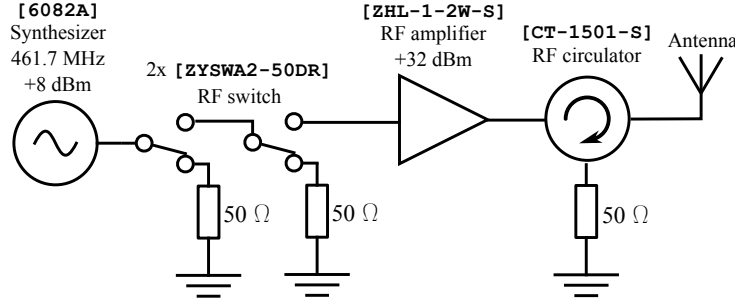


Figure 3.3: Radio-frequency source setup feeding the antenna.

stated in Appendix D yields simulated gain factors of $G(\text{YU}) = 4.94$ and $G_{\text{dBi}} = 6.94$ dBi. A YAGI-UDA antenna can be realized by expanding the driven half-wave dipole element by adding passive elements called directors and reflectors. Choosing the correct spacing of the passive elements and the driven element, constructive interference in the forward direction and destructive interference in the backward direction enhance the directivity of the device. Figure 3.2 b) shows a simple realization of such an antenna consisting of one active and two passive elements. Lengths and spacings applicable for use in the limited space near the vacuum chamber were chosen with the help of simulation tools [110, 111].

In Figure 3.4 a), a typical radio frequency scan driven with the YAGI-UDA antenna around the $|F = 1, m_F = 0\rangle \rightarrow |F = 2, m_F = 0\rangle$ transition is depicted. With a square pulse width of $\tau = 400 \mu\text{s}$, a FOURIER transform-limited line with a $\sin(x)/x$ behavior is expected. However, due to an imperfect square pulse shape with “rounded” corners that is suggested by discrete FOURIER transform of the data set, the function in frequency space is more complex. Figure 3.4 b) shows a comparison of RABI oscillations driven between the potassium states $|F = 1, m_F = 0\rangle$ and $|F = 2, m_F = 0\rangle$ using a half-wave dipole with a length of $l_{\text{de}} = 326.0 \text{ mm}$ (Appendix D) and a three-element YAGI-UDA antenna that were placed in the horizontal directly at the large vacuum viewport above one of the 3D MOT beams. The RABI frequencies are proportional to the irradiated intensity at the location of the atoms and are thus a good measure to test the applicability and performance of an antenna. As both measurements were performed with +28 dBm before the antennas, the ratio of the their gain factors

$$\frac{G(\text{YU})}{G(\text{dip})} = 2.99 \quad (3.5)$$

implies the same ratio when comparing the achievable RABI frequencies, however,

$$\frac{\Omega(\text{YU})}{\Omega(\text{dip})} = 2.54. \quad (3.6)$$

This deviation from the expected value of $\approx 20\%$ can most likely be attributed to inaccuracy of the antenna gain simulation. Estimation of the mismatch loss due to the different antenna impedances yields higher losses for the dipole antenna and can thus not explain the observed RABI frequency ratio.

In comparison to loop antennas that irradiate a mixed magnetic field polarization, the dipole incorporated in the YAGI-UDA antenna features comparably clean linear polarization. The polarization is oriented such that $\vec{e}_{\text{dip}} \perp \vec{k} \perp B_a$ is fulfilled, where \vec{e}_{dip} is the orientation of the antenna dipole, \vec{k} is the direction of radiation, and B_a is the polarization of the irradiated magnetic

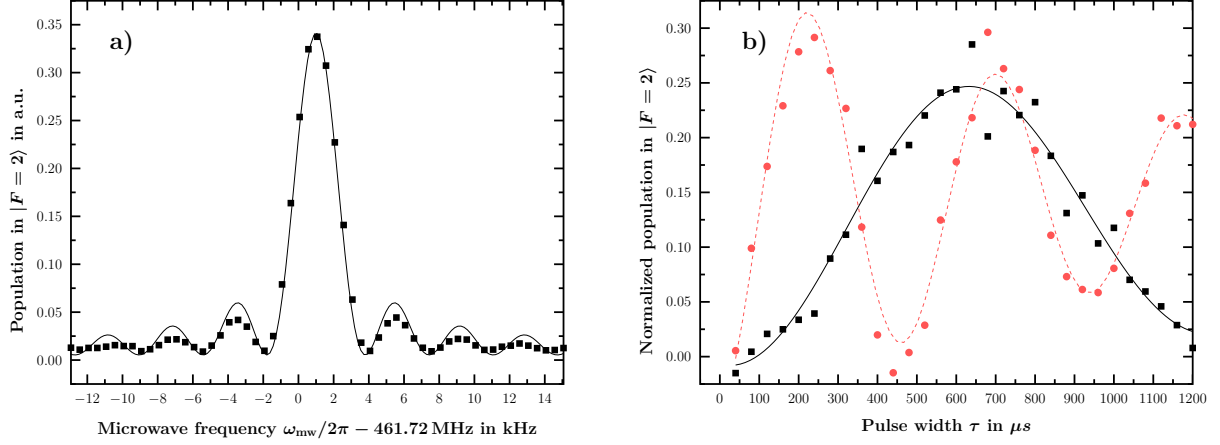


Figure 3.4: a) FOURIER transform-limited radio frequency scan with square pulse width of $\tau = 400 \mu s$ around the $|F = 1, m_F = 0\rangle \rightarrow |F = 2, m_F = 0\rangle$ transition (black squares). A least squares fitting function of the form squared BESSEL $(J_0(\omega_{mw}))^2$ serves as a guide to the eye. A discrete FOURIER transform indicates an imperfect square pulse shape with “rounded corners”. b) Potassium RABI oscillations between $|F = 1, m_F = 0\rangle$ and $|F = 2, m_F = 0\rangle$ driven with radio-frequency radiation in dependence of the pulse width. The half-wave dipole antenna (black squares) yields a RABI frequency of Ω (dip) = 5.2 kHz. In the case of the YAGI-UDA antenna (red circles), Ω (YU) = 13.1 kHz. Also shown are damped sine fitting curves (solid black and dashed red lines). The loss of contrast for longer pulse widths can be explained by the finite temperature of the potassium ensemble and the directivity of the YAGI-UDA antenna.

field. A demonstration experiment is shown in Figure 3.5. The data sets a), b), and c) depict three radio frequency scans with three configurations generating different orientations of \vec{B}_a and \vec{B}_q , namely $\vec{B}_a \perp B_q$ or $\vec{B}_a \parallel B_q$. By selection rules configuration a) with $\vec{B}_a \perp B_q$ can only address σ transitions with $\Delta m_F = \pm 1$ which are separated from the $|F = 1, m_F = 0\rangle \rightarrow |F = 2, m_F = 0\rangle$ transition in frequency space by $g_F \mu_B B_q$ through the linear ZEEMAN effect. Accordingly, switching B_q into the vertical direction in configuration b) yields $\vec{B}_a \parallel B_q$ and suppresses σ transitions and allows π transitions with $\Delta m_F = 0$ in turn. Finally, rotating the antenna by 90° about \vec{k} in configuration c) switches back to σ transitions. Note that small remaining signals of suppressed transitions are visible in all three scans due to slight imperfection in the orientation of the magnetic fields and residual polarization impurity.

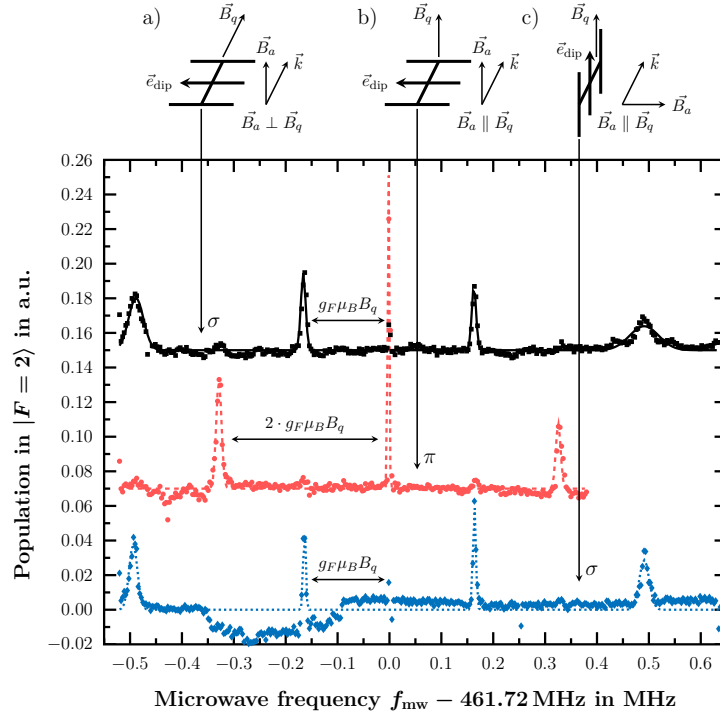


Figure 3.5: Radio frequency scans for three different quantization field and antenna configurations a), b), and c) allowing for σ or π transitions by selection rules. The data sets are shifted by arbitrary signal offsets for better visibility and fitted GAUSS functions are overlaid to guide the eye. Data set c) is subject to a slow drift caused by the detection that is irrelevant for this demonstration.

3.2 Potassium laser system

The potassium laser system is divided into two parts: (i) the cooling and trapping system (see Section 3.2.1) that in combination with the shared fiber distribution system (see Section 3.2.2) provides the light fields for the dual MOT and sub-DOPPLER cooling, and (ii) the coherent manipulation system (see Section 3.2.3), which is utilized for coherent manipulation of potassium by means of stimulated RAMAN transitions. All seed lasers employed are based on an interference-filter stabilized narrow-linewidth external cavity diode laser (ECDL) design [112, 113] with anti-reflection coated ridge waveguide lasers [Eagleyard EYP-RWE-0790-04000-0750-SOT01-0000] at their heart. In order to provide an absolute frequency reference, an ECDL is locked via offset-free frequency modulation spectroscopy of potassium in a vapor cell [114]. The signal of the DOPPLER-free spectroscopy of potassium in its natural abundance is dominated by the $^{39}\text{K} |F = 1/2\rangle \rightarrow |F'\rangle$ crossover transition, which is 49 MHz blue detuned¹ with respect to the $4^2S_{1/2} \rightarrow 4^2P_{3/2}$ fine structure transition [115]. All other lasers are phase locked to this reference laser. Unless stated otherwise, voltage-controlled oscillators (VCO) regulated by computer-controlled voltages are utilized to provide the reference frequency for the phase locks.

In order to phase-lock two lasers, their beat node is picked up on a photo diode [Hamamatsu G4176-03]. All locks used in the experiment are realized using a custom phase-locked loop based on a phase-frequency detector [MCH12140] capable of detecting input signals of up to ≈ 800 MHz.

¹ Taking into account the spectroscopy AOM, which is operated at a frequency of 100 MHz, the reference laser is subject to a total blue detuning of 99 MHz (see Appendix B).

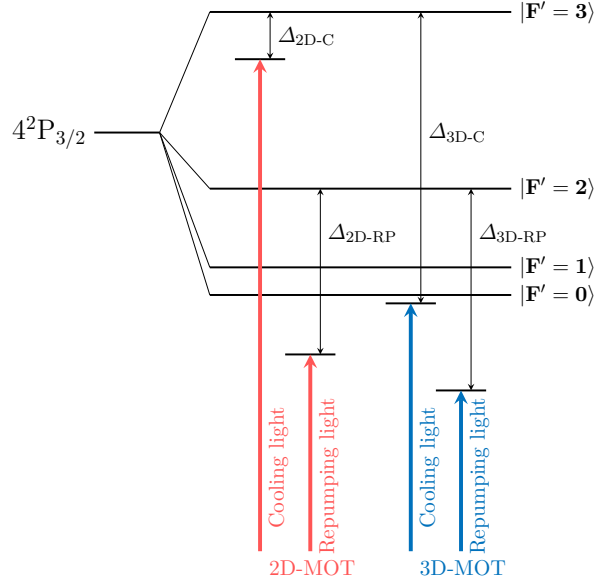


Figure 3.6: Detunings necessary for potassium dual MOT operation. The associated detunings are labeled Δ_x , wherein x stands for the cooling (C) or repumping light (RP) in the 2D MOT or 3D MOT.

For higher frequencies, mixing with local oscillators allows to transfer the beat signals into the accepted frequency regime. The phase lock setup of the potassium RAMAN lasers is explained in more detail in Section 3.2.3 and an overview of all the frequencies used in the experiment can be found in Appendix B.

Owing to the nonlinear behavior of tapered amplifiers (TA), the power ratio of two seed frequencies is often far off from 1:1 when a 1:1 output ratio is wanted, thus requiring flexibility in controlling to input ratio. Moreover, it is important to note, that as this approach is subject to four-wave mixing inside TA waveguide, effectively creating sidebands carrying a few percent of the total output power at a separation in frequency space corresponding to the seed difference frequency in the output spectrum. For the operation of a MOT (see Section 3.2.1) this loss is typically negligible. Furthermore, in the case of a ^{39}K MOT, the sidebands are well detuned by approximately one hyperfine splitting (≈ 460 MHz) and hence their contribution to the cooling process is insignificant due to their low scattering rate. On the contrary, when coherently manipulating an ensemble, the presence of sidebands has to be avoided to mitigate resulting systematic biases through the beam splitting process via additional light shifts and parasitic two-photon transitions [49, 116]. Dual-frequency seeded systems are subject to strong mode competition ultimately resulting in insufficient stability with respect to the output power ratio. In order to avoid mode competition, best possible spatial mode match of the two frequencies has to be ensured, i.e. by using a common single mode fiber as a spatial mode cleaner. In addition, adding an optical isolator before the TA reduces mode competition, and helps suppressing etalon effects that cause self seeding of the TA and other negative behavior.

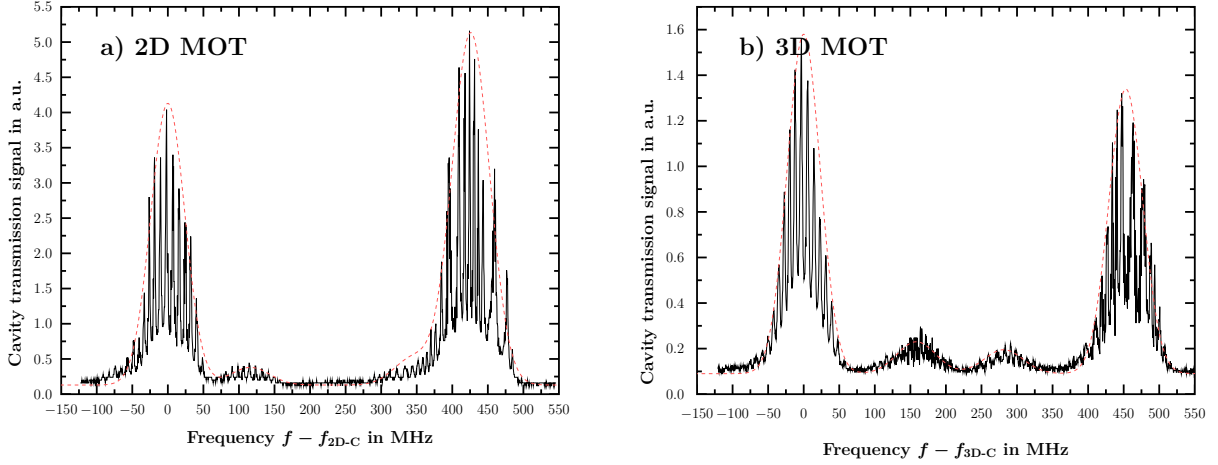


Figure 3.7: Cavity signals of the a) 2D MOT and b) 3D MOT TA outputs (solid black lines) and guides to the eye (red dashed lines). The signals are acquired using a non-confocal cavity, which explains the rich mode spectrum due to excitation of transverse electric modes. The cavity used has a free spectral range of 750 MHz and thus causes the sidebands to occur “reflected” inside of the seed frequencies rather than at the expected frequency difference ≈ 400 MHz outside the seed in the cavity spectrum.

3.2.1 Cooling and trapping

The laser system for cooling and trapping requires four separate light fields (Figure 3.6), two repumping and cooling when generating the transversely cooled beam of potassium, and two repumping and cooling for trapping in the 3D MOT. While it is in principle possible to use identical frequencies for operating the 2D MOT and the 3D MOT, independent control over the detunings Δ_x , wherein x stands for the cooling (C) or repumping light (RP) in the 2D MOT or 3D MOT, with respect to the resonances is required to operate the potassium dual MOT system at optimal performance (see Section 4.1.2). In addition, as opposed to the 2D MOT operation, the 3D MOT setup demands dynamic frequency and power control over the course of a single shot. It is necessary to dynamically vary the overall intensity, the power ratio of the associated cooling and repumping fields, and ramp their detunings, e.g. for sub-DOPPLER cooling techniques (see Section 4.1.3). Figure 3.8 displays a schematic of the potassium laser system supplying the dual MOT system.

Two-dimensional magneto-optical trap

For the 2D MOT, the two necessary laser frequencies for cooling and repumping are generated in a double-pass acousto-optical modulator (AOM) (Figure 3.8). Contrary to standard use of double-pass AOMs where the zeroth diffraction order is blocked, in this setup both the doubly-diffracted and the doubly-undiffracted order are reflected back by a curved mirror and pass the AOM a second time [118]. The AOM [Crystal Technology 3200-124] (AOM1) is driven at a frequency of $f_{\text{AOM}} \approx 213$ MHz that is slightly less than one half of the hyperfine splitting of ^{39}K . With the laser phase-locked near the cooling transition at ≈ 263 MHz red detuning with respect to the reference laser using the beat signal on photo diode PD1, the double-pass AOM setup efficiently shifts a tunable fraction of the injected light (“carrier”) by $2 \times f_{\text{AOM}}$ and creates second frequency (“sideband”) close to the repumping transition. Due to missing degrees of freedom caused by the inherent coupling of both the powers and the frequencies of the “carrier” and the “sideband”, this setup does not grant unlimited flexibility. It is thus only to be applied

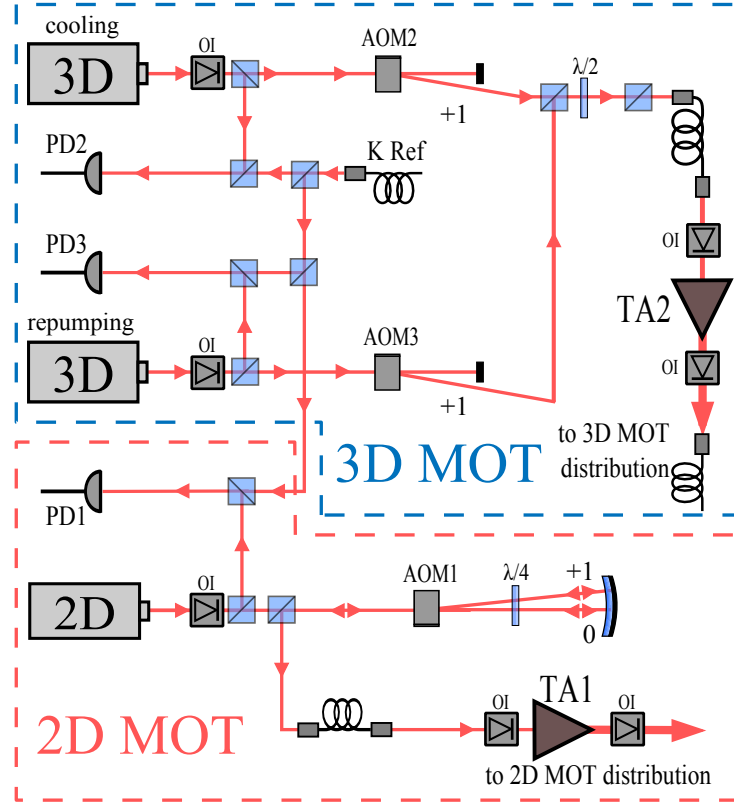


Figure 3.8: Optical setup for generating the light fields necessary to operate the potassium dual MOT system. The schematic is divided into two parts: the light field preparation for the **2D MOT** (dashed red box) and the **3D MOT** (dashed blue box). **2D** and **3D (cooling/repumping)** mark ECDL seed lasers [112, 113], **OI** optical isolators, **AOM** acousto-optical modulators, **PD** photo diodes, and **TA** tapered amplifiers. **K Ref** depicts a fiber output of the reference laser module. Except for the 2D MOT double-pass acousto-optical modulator setup and the wave plate to adjust the power ratio in the 3D MOT seed light, all standard mirrors, lenses, and wave plates have been omitted for clarity. The setup provides two outputs toward the shared fiber distribution system (Figure 3.9) with a total of 200 mW fiber coupled 3D MOT light and a 930 mW free-space output for the 2D MOT. Modified from Ref. [117].

in static frequency and power application with respect to the duration of one experimental cycle. The applicability as a RAMAN frequency source is discussed in Section 3.2.3.

For ideal spatial overlap, the two frequency components are mode matched via injection into a single mode optical fiber and guided to a TA [Eagleyard EYP-TPA-0765-01500-3006-CMT03-0000] (TA1) for amplification afterwards. Figure 3.7 a) shows the frequency resolved output of the 2D MOT TA for a seed ratio of $P_{2D-RP}/P_{2D-C} = 2.7$ at the typical 2D MOT detuning. Finally, the TA output is superimposed with the rubidium 2D MOT light and distributed onto the four 2D MOT optical fibers.

Three-dimensional magneto-optical trap

As opposed to the operation of the 2D MOT laser system, the necessity of variable laser intensity in both the cooling and repumping light and ramps of their detunings make simple solutions such as the aforementioned double-pass AOM unfavorable. In an attempt to ensure a maximum in flexibility, two ECDLs were set up to provide the seed frequencies for the 3D MOT tapered

amplifier (TA2) [Eagleyard EYP-TPA-0765-01500-3006-CMT03-0000]. The 3D MOT laser system is depicted in Figure 3.8. For the cooling laser, a phase lock to 264 MHz red detuning with respect to the reference laser via the beat signal on photo diode PD2 is used for operation of the 3D MOT. The dynamic control needed during sub-DOPPLER cooling [119] is granted in the following way: The phase lock reference frequency is provided by a VCO with tunable control voltage. In order to be able to ramp the laser intensity, the attenuation in the radio-frequency source driving AOM2 [Crystal Technology 3110-120] (Figure 3.8) can be changed over time. The repumping laser is phase locked to +189 MHz with respect to the reference laser for 3D MOT operation via photo diode PD3 and can also be ramped in its intensity via modulation of the attenuation in the radio-frequency source driving AOM3 [Crystal Technology 3110-120] (Figure 3.8).

Both lasers are superimposed and projected onto parallel linear polarization axes before they are coupled into a single-mode fiber and guided to the 3D MOT tapered amplifier (TA2). Figure 3.7 b) shows the frequency resolved output of TA2 for a seed ratio of $P_{3D-RP}/P_{3D-C} = 2.3$ at the typical 3D MOT detuning. After amplification to 1.5 W the TA output light is itself coupled into another fiber and finally superimposed with the rubidium cooling light on a dichroic mirror and distributed onto the six 3D MOT optical fibers.

3.2.2 Shared fiber distribution system

One of the striking benefits of building a dual species experiment with rubidium and potassium is the proximity of the wavelengths of their D₂ lines which lie at $\lambda_K = 766.7$ nm and $\lambda_{Rb} = 780.2$ nm. This small difference of only ≈ 13 nm allows a significant reduction of complexity of the optical setup. After superimposing the two wavelengths, it becomes possible to use optics with a design wavelength $(\lambda_{Rb} + \lambda_K)/2$ centered between the two species or, e.g. in the case of retardation wave plates, dichroic elements that are optimized for both wavelengths.

Figure 3.9 depicts the shared fiber distribution system [90]. Its purpose is to split the high power light fields onto the four 2D MOT and six 3D MOT optical fibers, and one fiber for fluorescence detection. For the 2D MOT distribution, incoming light from TA1 (Figure 3.8) is superimposed with incoming light from the rubidium 2D MOT TA with orthogonal polarization. A subsequent beam splitter consequently yields a 1:1 splitting with parallel polarization for both wavelengths. This allows, after turning the polarization by 45°, for the final 1:1 splitting of the initial two output ports and thus a distribution onto four optical fibers. In order to prevent losses when compensating for unequal splitting at the first beam splitter, the rubidium and potassium light are superimposed on a dichroic mirror. This enables arbitrary orientation of their polarizations and, in specific, parallel polarizations. The beams traverse a beam splitter that separates a small amount of light for the fluorescence detection. Afterwards, a setup of five beam splitters divides the light onto six paths leading toward the 3D MOT optical fibers.

The shared fiber distribution system provides the ability to switch the output fibers and to control their intensities. For operation of the 2D MOT no dynamic alteration of parameters over the course of a single experimental cycle is necessary. Shutter S1 which is common to both species is used to switch off the 2D MOT fiber outputs after loading the 3D MOT. For trapping in the 3D MOT, no dynamic control over the cooling and repumping detunings, their intensity ratio or the overall intensity is necessary. However, the subsequent steps in the experimental sequence, such as sub-DOPPLER cooling and state preparation techniques demand full control over the aforementioned parameters. Prior to superimposing the rubidium and potassium 3D MOT light, AOM4 and AOM5 [Crystal Technology 3080-120] are traversed to provide switching and attenuation abilities independently to both light fields. Before the light fields are split up onto the 3D MOT fibers, a shared shutter (S2) is installed. In addition to the preparation and

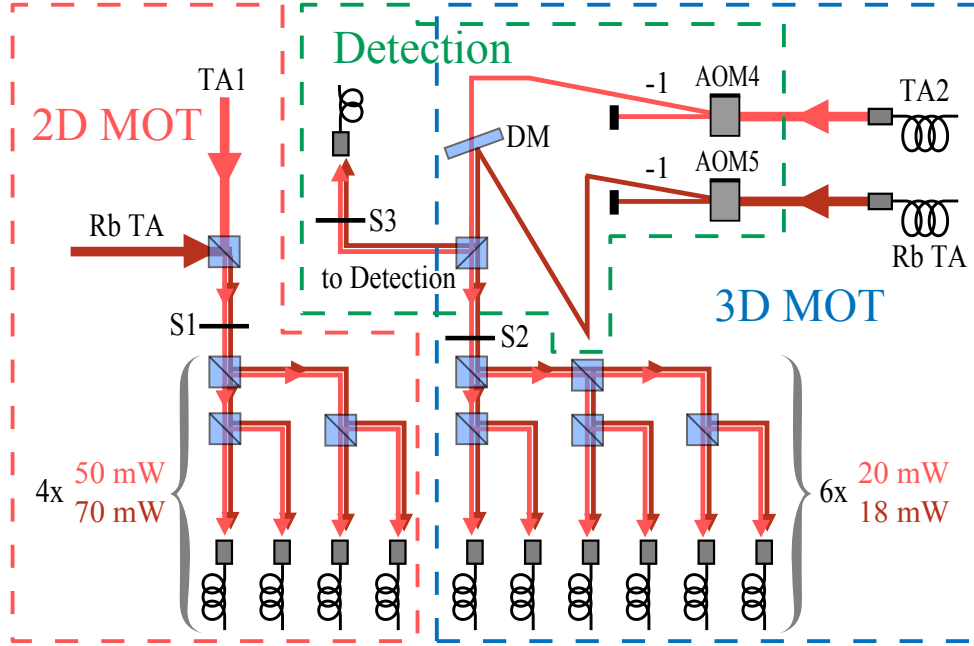


Figure 3.9: Shared fiber distribution system. The schematic is divided into three parts: the light field distribution for the **2D MOT** (dashed red red box), the **3D MOT** (dashed blue box), and the fluorescence detection (dashed green box). Light red (dark red) arrows display potassium light (rubidium light). **AOM** marks acousto-optic modulators, **S** shutters, **DM** a dichroic mirror, and **TA** tapered amplifiers. **Rb TA** labels incoming light from the relevant rubidium parts of the laser system [90]. The input power from **TA1** is 930 mW and is 200 mW from **TA2** (Figure 3.8). All standard mirrors, lenses, and wave plates have been omitted for clarity.

control of the 2D MOT and 3D MOT light, the system is capable of delivering detection light pulses using AOM4 and AOM5 on the vertical detection axis (see Section 4.2).

3.2.3 Coherent manipulation

Opposite to the two-frequency seed approach chosen for cooling and trapping (see Section 3.2.1), two separate TAs are used in order to avoid the drawbacks discussed before¹. The optical setup for coherent two-photon RAMAN coupling is displayed in Figure 3.10. Both the master and slave laser are amplified to 1.5 W in the tapered amplifiers TA3 and TA4 [Eagleyard EYP-TPA-0765-01500-3006-CMT03-0000] and subsequently superimposed with orthogonal polarizations. A following polarizing beam splitter projects both light fields onto parallel polarization axes. An AOM [Crystal Technology 3200-124] is utilized to pulse the RAMAN light that is fiber coupled and guided toward the RAMAN collimator. Likewise, the RAMAN light coupling rubidium is pulsed by a separate AOM superimposed with the potassium beam with parallel polarization on a dichroic mirror. The system yields a typical output power of ≈ 100 mW per potassium frequency after the fiber. In a normal experimental cycle of 1.6 s, the RAMAN light is pulsed up to four times with a typical pulse width of only 15 μ s. The resulting duty cycle of the RAMAN light of less than a part in ten thousand and the considerably high power of ≈ 600 mW in AOM6 and the

¹ The operation of a double-pass AOM setup for generating the RAMAN light fields was demonstrated in Ref. [117]. This approach was omitted due to missing long-term stability and troublesome mode matching of the two orders at high powers.

subsequent fiber coupling optics would cause the system, especially the diffraction efficiency and angle of AOM6, to be thermally unstable. This behavior can be partially suppressed as follows. The RAMAN light is kept switched on over the full experimental cycle except for a time window of ≈ 200 ms beginning with the state preparation (Chapter 4) and ending with the detection (see Section 4.2), thus increasing the duty cycle to almost 90%. Furthermore, rather than switching the RF power driving AOM6 off, the amplifier input is switched from 80 MHz to a secondary RF source at 110 MHz. The conditions for fiber coupling are neither fulfilled for the zeroth diffraction order, nor the 110 MHz diffraction. Hence, when the light is switched off all optical elements before the fiber coupler are exposed to similar optical power as compared to the active state. The same techniques are applied to the rubidium RAMAN laser system.

As derived in Section 2.1, two major requirements are imposed to the RAMAN laser frequencies: (i) An overall RAMAN laser detuning with respect to the D_2 line much larger than the natural linewidth of the intermediate states has to be maintained with the aim to suppress decoherence owing to single photon scattering while driving two-photon transitions. (ii) Sufficiently low laser phase noise has to be ensured as the RAMAN laser phase is imprinted onto the ensemble during atom-light interaction. (iii) Furthermore, the ability to carefully tune the RAMAN laser difference frequency allows to choose from the manifold of allowed two-photon transitions. Specifically, the capability to linearly ramp the difference frequency to compensate for the gravitationally induced DOPPLER shift has to be given.

Figure 3.11 shows the RAMAN frequency generation concept. The RAMAN master laser beat note with reference laser light on PD4 (Figure 3.10) is mixed with a VCO [Minicircuits ZX95-3360+] oscillating at $f_{VCO} = 3.4$ GHz. Afterwards, the resulting beat is phase-locked onto a frequency reference at $f_{Ref} = 100$ MHz [Spectra Dynamics DLR-100]. The polarity of the feedback loop and a blue or red detuning with respect to the reference laser determine the RAMAN master laser detuning:

$$\frac{\Delta}{2\pi} = \pm f_{VCO} \pm f_{Ref}. \quad (3.7)$$

With the RAMAN master laser phase-locked loop preserving the overall RAMAN laser detuning, a second feedback loop locks the difference frequency $\omega_R = \omega_1 - \omega_2$ of the RAMAN master and slave laser. The required agility of ω_R is established as follows: The beat note near 462 MHz of

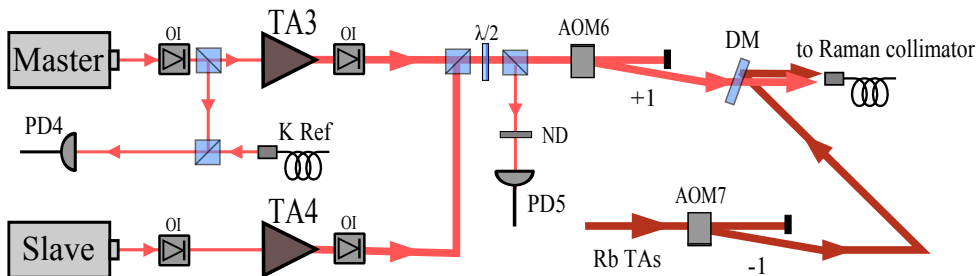


Figure 3.10: Potassium RAMAN optical setup. Both, the master and slave laser lights, are amplified by tapered amplifiers **TA3** and **TA4**, superimposed with orthogonal polarizations and projected onto parallel polarization axes at a subsequent polarizing beam splitter. **AOM6** is used to pulse the power coupled into an optical fiber guiding the light to the RAMAN collimator. The rubidium RAMAN light, itself having parallel polarization, is pulsed using **AOM7** and superimposed with the potassium RAMAN light with parallel polarization. The photo diodes **PD4** (Master) and **PD5** (slave) pick up the required beat notes employed in Figure 3.11. **OI** marks optical isolators.

both RAMAN lasers on PD5 is filtered and subsequently mixed with a signal $f_{\text{Mult}} = 400 \text{ MHz}$ that is generated by multiplying the frequency reference $f_{\text{Ref}} = 100 \text{ MHz}$ [Spectra Dynamics DLR-100] by a factor of four using a frequency multiplication chain [Rupptronik GMU69124LN]. The derived frequency is phase-locked to a direct digital synthesis (DDS) synthesizer [Spectra Dynamics LNFS-100] frequency at $f_{\text{DDS}} \approx 62 \text{ MHz}$ that is capable of generating the desired linear frequency ramps. Therefore, with the correct polarity of the feedback loop and a blue detuning with respect to the master laser, the frequency difference is

$$\frac{\omega_R}{2\pi} = f_{\text{Mult}} + f_{\text{DDS}} \approx 462 \text{ MHz} . \quad (3.8)$$

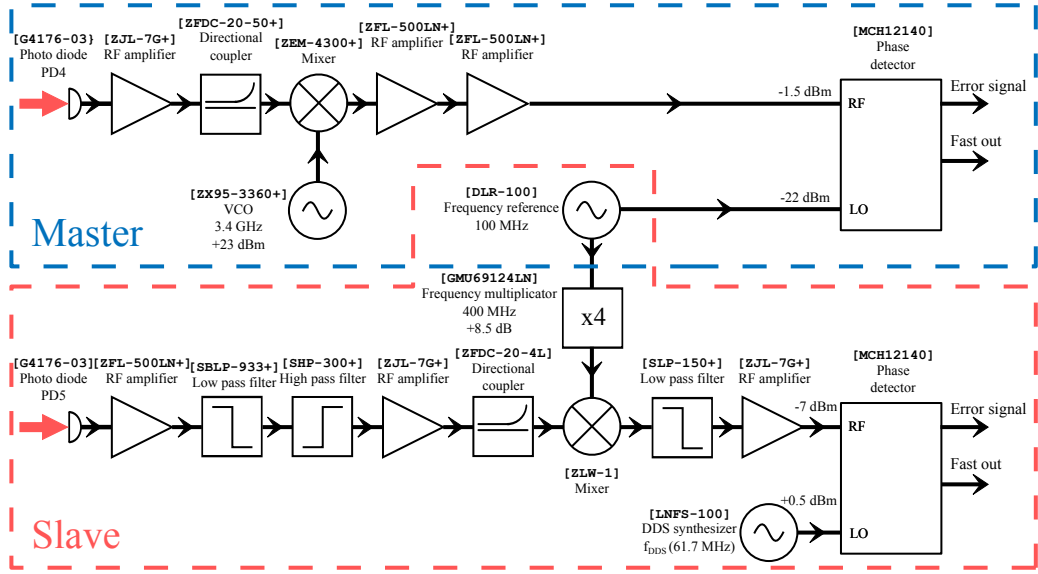


Figure 3.11: Schematic of RAMAN master and slave phase locks. The labels **PD4** and **PD5** correspond to the photo diodes marked in Figure 3.10.

3.3 Shared interferometry and detection optics

The peripheral optics necessary for operating the matter wave interferometer are depicted in Figure 3.12. They can be split into two parts: (i) The RAMAN laser light path, including beam shaping optics, mirrors for vertical beam pointing, and the adjustable retroreflection mirror on a vibration isolation platform; (ii) The state-selective fluorescence detection setup featuring a vertical detection beam, and an upper and a lower detection system.

The RAMAN laser light is guided to the vacuum system in the common fiber. After the fiber, the beam is collimated to a diameter of 2.0 cm with a single achromatic lens of focal length $f = 100$ mm [Thorlabs AC508-100-B]. A subsequent adjustable diaphragm allows to choose the beam diameter such that no aperture thereafter, in specific the vacuum viewports, are clipping the beam. With the two RAMAN frequencies leaving the fiber with parallel polarizations, a quarter-wave plate is placed in the beam path such that both frequency components are circularly polarized with same helicity afterwards (σ/σ polarization; Section 2.1). Two protected silver mirrors are utilized to align the beam parallel to gravity and such that it traverses the vacuum chamber. At the bottom end, the chamber is angled by 5° with respect to the top viewport. In this way, parasitic standing waves and etalon effects caused by the coplanar exit viewport are avoided. Shielded from air turbulences the RAMAN beam enters an acoustic isolation housing and is retroreflected by an adjustable mirror [Fichou] with a specified peak-to-valley flatness of $\lambda/20$ that is resting on a commercial vibration isolation platform [Minus K 150BM-1].

The apparatus features two separate systems for state-selective fluorescence detection (see Section 4.2). The laser light employed for state-selective fluorescence detection is expanded to a beam diameter of 2.0 cm and superimposed with the RAMAN beam on a polarizing beam splitter to allow common use of optics and the vertical magnetic quantization field (see Section 3.1.1). Although the bottom HELMHOLTZ coil is located a few centimeters above the center of the lower detection zone, this is possible as the magnetic field is not instantly zero in direct vicinity outside of the coil pair. The upper detection is based on a bare photo diode (PD7) [OSI Optoelectronics PIN-10D] directly attached to a viewport in the horizontal plane that is collecting fluorescence light emitted by the atoms. It is used for short times of flight of up to a hundred milliseconds,

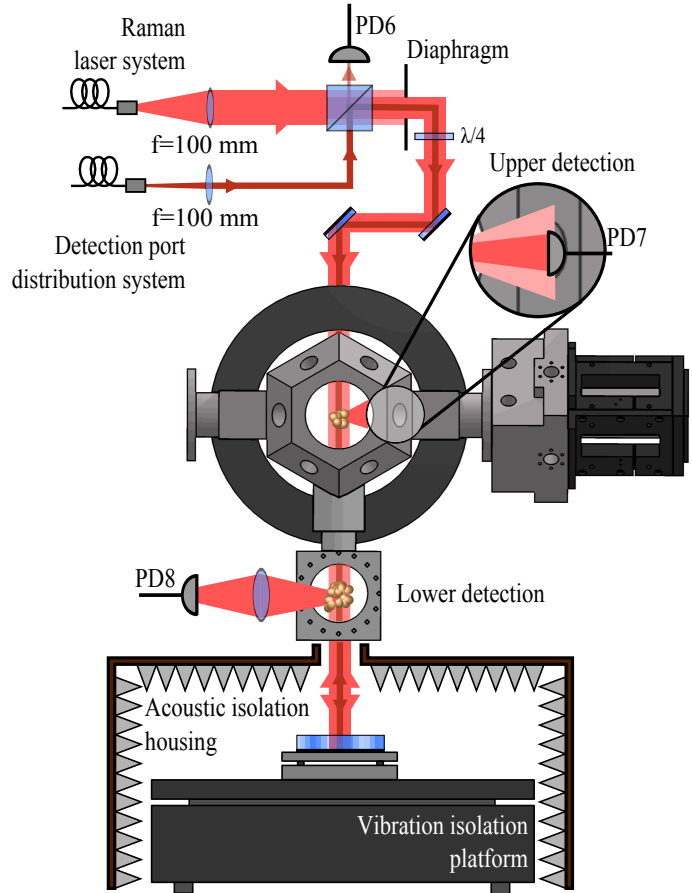


Fig. 3.12: Interferometry and detection optics. The fiber outputs are labeled with respect to Figure 3.10 and Figure 3.9. The displayed beam diameters of the RAMAN and detection light fields are not to scale.

e.g. when using hot ensembles with no state-selection. The lower detection utilizes an optical system collecting fluorescence light with a large aperture lens ($f = 200$ mm) and imaging it onto a photo diode (PD8) [OSI Optoelectronics PIN-10D]. The lower detection system has to be used when working with the apparatus's maximum times of flight on the order of two hundred milliseconds. The resulting photo currents are amplified by a current amplifier [Femto DLPCA-200] and then fed into a post-processing computer system.

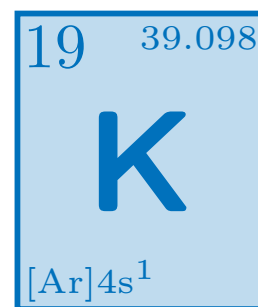
CHAPTER 4

Matter wave interferometry with potassium

In this Chapter, single species operation of the experiment with potassium is described. In preparation for the dual species experiments performed in this thesis (Chapter 5), a thorough introduction of all relevant experimental techniques employed in matter wave interferometers is provided, and differences of potassium apparatuses in comparison to typical rubidium or cesium experiments are pointed out. In Section 4.1, a general overview on properties of potassium in the context of laser cooling is provided and followed by a characterization of the potassium dual MOT system with a focus on the performed sub-DOPPLER cooling technique in Section 4.1.3, and state-selective fluorescence detection in Section 4.2. Based on Section 2.1, all tools for coherent manipulation of potassium employed in this thesis are described from a technical point of view in Section 4.3. Methods of input state preparation, coherent coupling of the potassium hyperfine ground states with stimulated two-photon RAMAN transitions are explained. The Chapter closes with Section 4.4 which elaborates on the results obtained with potassium single-species interferometry, and finally a general discussion of the possibilities and challenges when performing matter wave interferometry with potassium in Section 4.5.

4.1 Laser cooling of potassium

The boson ^{39}K was chosen as the second species next to ^{87}Rb [88] due to its large natural abundance (Table A.2) and its electronic energy level structure with respect to laser cooling compared to the other two stable isotopes ^{40}K and ^{41}K [120]. On the one hand, bosonic potassium features an $m_F = 0$ state that is insensitive to magnetic fields to first order. On the other hand, the excited state hyperfine splitting plays an important role for handling potassium as will be described below¹. The properties and techniques described here are focused on the isotope ^{39}K . Most of the underlying physics are, however, very similar for the other boson, ^{41}K , and can thus be transferred with only minimal adaptations [119]. Due to the much larger excited state hyperfine splitting, the integer nuclear spin, and the inverted hyperfine structure the fermion ^{40}K acts differently and requires other approaches [121]. Below, the energy level structure of ^{39}K is introduced and the results for the operation of the dual MOT system and sub-DOPPLER cooling are presented. A full overview on all frequencies typically employed in the experiment is given in Appendix B.



¹ Figure A.1 provides a comparison of the three potassium isotope energy levels.

4.1.1 Energy level structure of ^{39}K

The isotope ^{39}K features a typical alkali metal energy level structure (Figure 4.1). Due to its three closed electronic shells, the weakly bound s -orbital photoelectron dominates the optical spectrum. Compared to the two neighboring bosonic alkali species¹ ^{23}Na , ^{85}Rb , and ^{87}Rb , ^{39}K and ^{41}K are subject to an anomalously low hyperfine energy splitting, in both the ground state and the excited states. The peculiar behavior of bosonic potassium can be attributed to their anomalously small nuclear magnetic moments (Table A.2) [123, 124]. Low hyperfine splitting of the ground state² has an impact on the AC-STARK shift imposed by the potassium RAMAN lasers (see Section 4.3.2). It moreover dictates the magnitude of the quadratic ZEEMAN effect (see Section 5.2.2). Likewise, the magnitude of the excited state splitting scales as the ground state splitting. Correspondingly, in terms of laser cooling, a crucial difference to rubidium is posed by the fact that the full $^2\text{P}_{3/2}$ state in ^{39}K only spans³ $\omega_{0'3'} \approx 5.5 \Gamma_{\text{K}}$, where $\Gamma_{\text{K}} = 2\pi \cdot 6.035 \text{ MHz}$ is the natural linewidth [120]. When treating random polarization as typically seen by an atom in a MOT, this proximity of neighboring states in the excited manifold causes by two

orders of magnitude stronger optical pumping into $|F = 1\rangle$ as compared to rubidium when shining in a near-resonant light field coupling $|F = 2\rangle \rightarrow |F' = 3\rangle$ [125]. Likewise, standard sub-DOPPLER cooling techniques [62, 63] rely critically on the condition $\omega_{0'3'} \gg \Gamma$, as in the case of sodium, rubidium, and cesium, or $\omega_{0'3'} \ll \Gamma$ as in the case of strontium [119]. For ^{39}K , where $\omega_{0'3'} \approx \Gamma_{\text{K}}$, photon reabsorption and heating forces inhibit efficient sub-DOPPLER cooling and the cooling process becomes more complicated [119] as is explained in detail in Section 4.1.3.

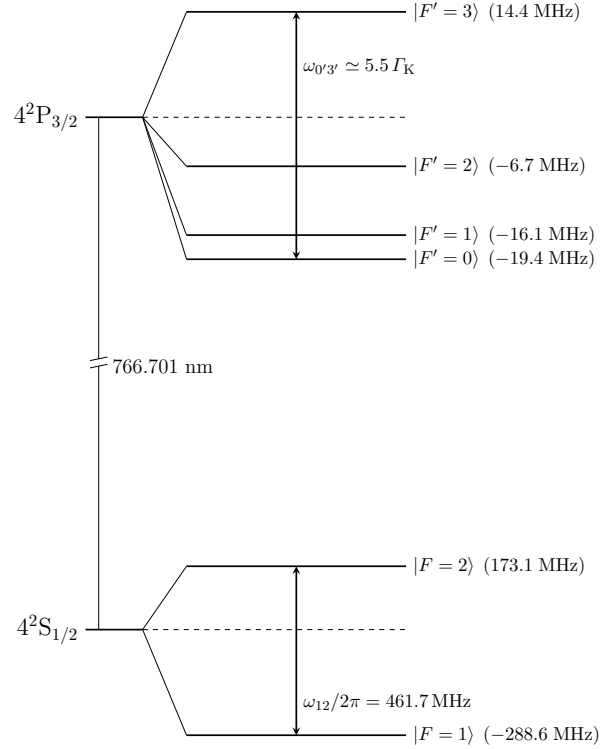


Fig. 4.1: D₂ line energy diagram of ^{39}K . Numerical values are taken from Refs. [107, 122] and are stated in ordinary frequency.

¹ All mentioned nuclei have a nuclear spin $I = 3/2$ except for ^{85}Rb , which has $I = 5/2$.

² The splitting is $\omega_{12} \approx 2\pi \cdot 462 \text{ MHz}$ for ^{39}K , which is a factor of ≈ 15 smaller than in the case of ^{87}Rb with $\omega_{12} \approx 2\pi \cdot 6.834 \text{ GHz}$.

³ Throughout this thesis, $\hbar\omega_{jk}$ is the energy difference of two states $|F = j\rangle$ and $|F = k\rangle$ within a hyperfine multiplet.

4.1.2 Dual MOT performance

As a consequence of the strong decay channel into $|F = 1\rangle$ when shining in cooling light on the $|F = 2\rangle \rightarrow |F' = 3\rangle$ transition, the repumping transition $|F = 1\rangle \rightarrow |F' = 2\rangle$ has to be driven equally strong when realizing a MOT¹. This is substantially different from the rubidium MOT case, where repumping intensities on the order of a few $\mu\text{W}/\text{cm}^2$ are sufficient.

The energy level structure of potassium allows for two detuning ranges (regions I and IV in Figure 4.2) for the cooling light in which DOPPLER cooling on the $|F = 2\rangle \rightarrow |F' = 3\rangle$ transition is dominant [119, 126]. For small detunings on the order of one linewidth, DOPPLER cooling can be achieved in the low intensity regime employing only a few saturation intensities. In this case power broadening is negligible and the scenario is comparable to atomic systems with much larger excited state hyperfine splitting and practically no interplay with neighboring states. In the high intensity regime, where power broadening has to be accounted for, a second DOPPLER cooling region exists for detunings larger than the excited state hyperfine splitting. While much higher intensities are required for this regime to keep up a reasonable scattering rate, the velocity capture range is about an order of magnitude larger as compared to the low intensity regime.

The characterization of the dual MOT system used in this thesis is performed in the following way: With fixed laser detunings, power ratio, magnetic field gradient of the 3D (2D) MOT, the 2D (3D) MOT cooling and repumping frequencies were scanned beginning from resonance toward increasing red detuning in steps of half the natural linewidth. Figure 4.3 a) depicts the normalized results of the 2D MOT characterization with a magnetic field gradient of 8 G/cm. With a summed intensity of cooling and repumping light of $3.2 I_{\text{sat}}$ per beam, the 2D MOT is clearly in the low intensity regime². Accordingly, efficient loading is only possible within a detuning range of the cooling laser $\Delta_{2\text{D-C}} \approx -0.5 \dots -2 \Gamma_K$ near resonance with a small velocity capture range as compared to the high intensity regime where $\Delta_{2\text{D-C}} \geq -5.5 \Gamma_K$. This distinction of the low and high intensity regime is resembled in Figure 4.3 b) showing the normalized loading performance of the 3D MOT with a magnetic field gradient of 6.8 G/cm. Here the dashed white line marks the scan range of Figure 4.3 a) and a very similar behavior is visible. For the 3D MOT with its smaller beams, a summed intensity of cooling and repumping light of $7.5 I_{\text{sat}}$ per beam is available and the performance optimum is shifted toward larger detunings of $\Delta_{3\text{D-C}} \approx -5 \Gamma_K$

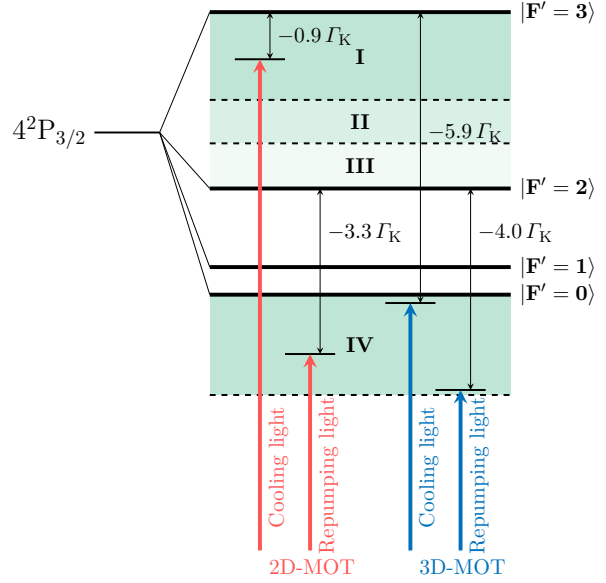


Fig. 4.2: Detunings for potassium dual MOT operation. Regions I and IV mark laser detunings for which DOPPLER cooling is active. In regions I and II sub-DOPPLER cooling is possible [119, 126]. Tuning the laser into region III causes heating.

¹ In fact, it is unfortunate to label these transitions in potassium “cooling” and “repumping” transitions [126] instead of two “cooling” transitions. Throughout this thesis, however, the former case will be used for better distinction and similarity to the natural nomenclature used in the case of rubidium.

² For comparison, 35 I_{sat} per 2D MOT beam are reported in Ref. [125].

and a correspondingly larger velocity capture range as expected.

Based on the performed characterization, the typical dual MOT operation parameters are chosen as marked in Figure 4.2. Deviations from the characterization can be explained by fine tuning performed to optimize dual species operation, long-term variations in the MOT beam power balancing, and drifts of the overall power available. Additionally, the optimal 3D MOT magnetic field gradient was found to be 4.5 G/cm. In dual species operation, the dual MOT system typically yields 3×10^7 atoms of ^{39}K within a loading time of 1 s using the stated parameters [51]. When optimized for single species operation with potassium, the loading rate can be up to 1×10^8 atoms within 1 s.

4.1.3 Sub-Doppler cooling

Temperatures commonly achieved in a ^{39}K 3D MOT are on the order of a few millikelvin and hence too high for matter wave interferometry. For example, an ensemble of ^{39}K released from a 3D MOT with a temperature of 3 mK expands at a rate of 0.8 m/s. Given the maximum free fall time in the present apparatus of 200 ms, this yields a final cloud size of 16 cm which exceeds the spatial limitations of the vacuum chamber by far and strongly amplifies phase contributions generated due to transverse motion of the cloud [127]. Moreover, the momentum width in frequency space (Equation (4.2) & Section 4.3.3) negatively affects the excitation probability of a single beam splitting pulse.

Several methods exist to significantly reduce the temperature of bosonic potassium ensembles [119, 128, 129]. These approaches are qualitatively different and demand various degrees of technical effort, such as additional lasers resonant with the D_1 line, or at ultraviolet wavelengths. In this thesis, the dark optical molasses scheme as described in Ref. [119] is implemented. Although the feasible final temperatures of $\approx 25 \mu\text{K}$ [119] are a factor of ≈ 4 higher than in the D_1 line based scheme reported in Ref. [129], it features the advantage that no additional lasers are necessary. It makes use of a ramping strategy for the cooling laser detuning and intensity that induces a dynamical transition from DOPPLER cooling to sub-DOPPLER cooling. During the cooling sequence, controlled repumping from the dark $|F = 1\rangle$ state allows to limit heating processes

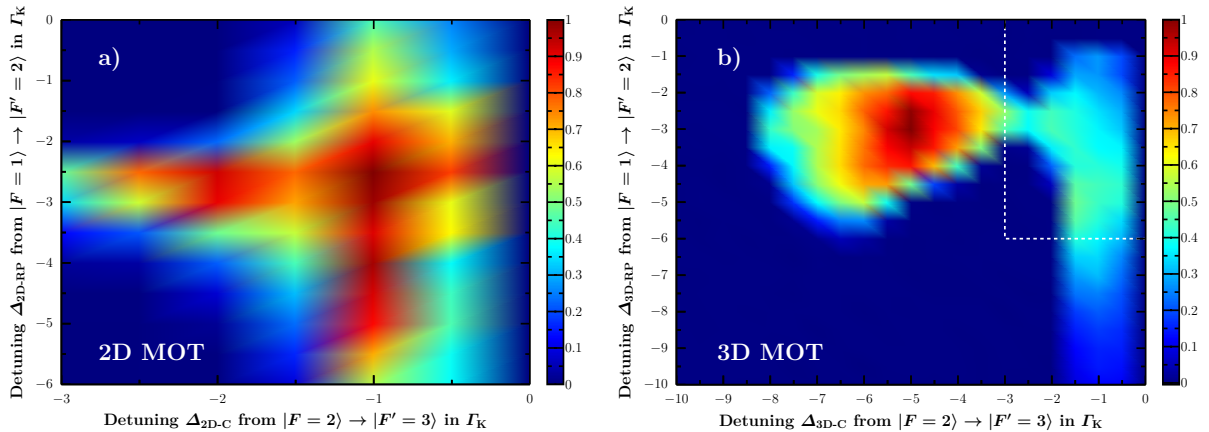


Figure 4.3: Normalized loading performance in dependence of the detunings Δ_x of the cooling and repumping lasers of the a) 2D MOT and b) 3D MOT. The summed intensity of cooling and repumping light is $3.2 I_{\text{sat}}$ for the 2D MOT and $7.5 I_{\text{sat}}$ for the 3D MOT. Data points are available at a step size of $0.5 \Gamma_K$ in both Figures and the presented surface plot is interpolated. The dashed white line in Figure b) encloses the plot area shown in Figure a).

caused by photon reabsorption and spontaneous emission [119].

Figure 4.4 a) shows the cooling sequence as employed in this thesis. The cooling process is initiated at time $t = 0$ ms by turning off the 3D MOT magnetic field and reducing the repumping intensity to $\approx 1/100 I_{3D-C}$ while changing its frequency onto resonance, and jumping onto a cooling laser detuning $\Delta_{3D-C} = -0.7 \Gamma_K$. Over a time span of 15 ms the detuning is subsequently linearly increased to a final value $\Delta_{3D-C} = -2.3 \Gamma_K$, smoothly changing the detuning from region I, in which DOPPLER cooling is dominant, into region II, where sub-DOPPLER cooling becomes the leading cooling force (Figure 4.2). Simultaneously, the cooling laser intensity $I_{3D-C}/I_{sat} = 7.5 \dots 0.9$ is decreased over the same time interval. Figure 4.4 b) shows a time-of-flight series with a CCD camera [ALLIED vision technologies Guppy GF 033B] imaging the ensemble expansion in horizontal and the vertical (beam splitting) direction after applying the cooling sequence. From linear fits of the squared ensemble radius over the squared time-of-flight temperatures of $T_x = 28.1 \mu\text{K}$ for the horizontal and $T_z = 25.8 \mu\text{K}$ for the vertical direction can be inferred [130].

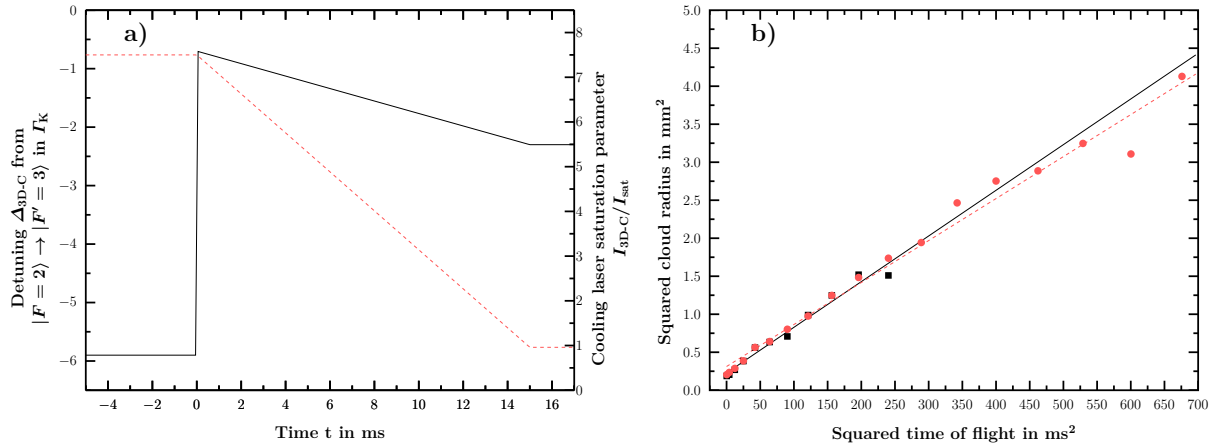


Figure 4.4: Figure a) shows the sub-DOPPLER cooling time sequence [119] for the cooling laser detuning (solid black line) and its intensity (dashed red line) as implemented in the experiment. Figure b) displays the results of a time-of-flight series obtained after cooling. The squared ensemble radius in horizontal (vertical) direction over the squared time of flight is marked by black squares (red circles). Due to the limited field of view in the horizontal direction caused by the aspect ratio of the CCD chip the fitting algorithm does not converge for times longer than 15 ms. The related temperatures can be inferred from linear fits and yield $T_x = 28.1 \mu\text{K}$ for the horizontal direction (black solid line) and $T_z = 25.8 \mu\text{K}$ for the vertical direction (red dashed line).

4.2 Fluorescence detection

Both the population difference of the internal states as well as the spatial distribution of an ensemble can hold valuable information such as atom number, ensemble temperature and the interferometer phase. For purposes of atom number detection and temperature measurements, the system features a CCD camera [ALLIED vision technologies Guppy GF 033E] to record spatially resolved fluorescence images of the atomic ensembles in the horizontal 3D MOT plane. Reading out an interferometer phase, however, requires readout of the population difference of the two output states. Next to spatially resolved absorption or fluorescence imaging [130] which is applicable whenever atomic ensembles to be imaged are optically dense enough and spatially well separated, state-selective fluorescence detection is a standard technique that can be applied whenever the interferometer output ports are assigned different internal states. This is naturally the fact in an interferometer based on stimulated RAMAN transitions, in which the two external momentum states are entangled with the two internal hyperfine ground states (see Section 2.1). The state-selective fluorescence detection principle aims to extract the normalized population $P_{|F=2\rangle}$ from fluorescence signals picked up by photo diodes, which do not require spatial resolution or sufficient spatial separation¹ of the output states. Figure 4.5 a) displays a typical detection sequence for a single species interferometer. A cooling light pulse resonant with the $|F = 2\rangle \rightarrow |F' = 3\rangle$ transition is applied, delivering a fluorescence signal proportional to the number of atoms $N_{|F=2\rangle}$ populating the $|F = 2\rangle$ output state. Afterwards, a repumping pulse $|F = 1\rangle \rightarrow |F' = 2\rangle$ transfers all atoms into $|F = 2\rangle$. A subsequent second cooling light pulse is then proportional to the total atom number $N_{|F=1\rangle+|F=2\rangle}$. After a waiting time to allow all atoms to leave the detection zone, a background pulse without atomic fluorescence c_{bg} is recorded. This detection scheme features immunity against total atom number fluctuations, as it is normalized:

$$P_{|F=2\rangle} = \frac{N_{|F=2\rangle} - c_{\text{bg}}}{N_{|F=1\rangle+|F=2\rangle} - c_{\text{bg}}}. \quad (4.1)$$

Furthermore, a post correction algorithm for intensity changes between the different cooling pulses and the background detection is implemented to minimize the influence of detection beam power fluctuations. For this purpose, a signal proportional to the intensity of the detection pulses is recorded by picking up leakage light on photo diode PD6. Afterwards, possible background variations due to intensity fluctuations between the pulses and the background detection are corrected for by normalization. Typically, detection laser frequency noise, and arrival time jitter which varies the overlap of the of the imaging region with the detection beam and the atomic cloud, remain the dominating noise sources. For the case of two-species detection, a nested scheme as shown in Figure 4.5 b) is applied. Here, the rubidium detection that is much more robust than the one for potassium is placed around the potassium pulses in order not to change the potassium detection sequence. To conserve full contrast in an interferometer output measurement, mixing of the two states, e.g. by repumping the lower hyperfine ground state to enhance the scattering rate, must be avoided at all costs. Reading out the population of the upper interferometer output state with a high signal-to-noise ratio typically relies on the ability to drive a cycling transition without any repumping of the lower interferometer state. This maximizes the scattering cross section and fully suppresses losses into the dark lower state. The optical pumping scheme is depicted in Figure 4.6. As parasitic excitations to $|F' = 1\rangle$ and

¹ Sufficient spatial separation is given, when the ensemble is at or below the recoil temperature in the direction of separation and hence drifts apart faster than the ensembles expand.

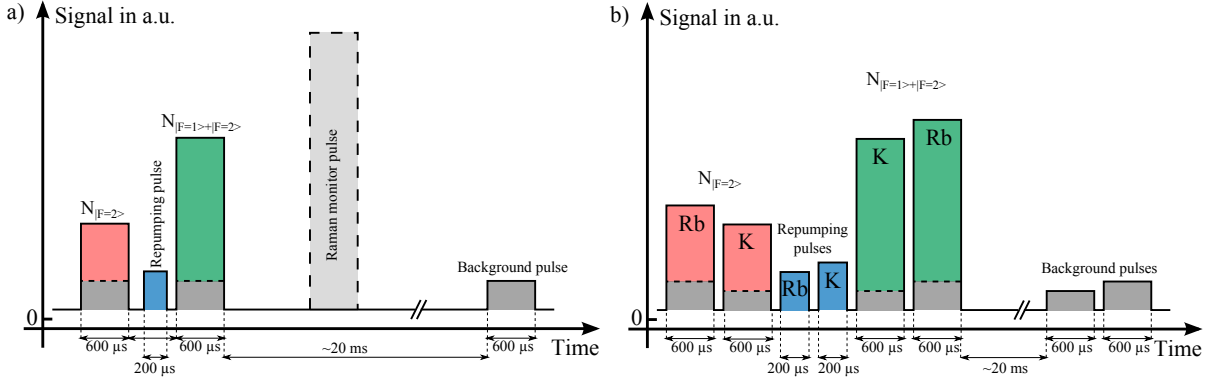


Figure 4.5: Typical detection pulse sequence for a) the single species case and b) the dual species case. A cooling pulse $|F = 2\rangle \rightarrow |F' = 3\rangle$ (red), repumping all atoms into $|F = 2\rangle$ (blue), and a total atom number cooling pulse (green) allow to extract the normalized population $P_{|F=2\rangle}$ after subtraction of the background. As an additional feature, both detection photo diodes, PD7 and PD8, can as well be used to provide a measure for the long-term stability of the RAMAN light power by triggering a RAMAN light pulse after completion of the state detection.

$|F' = 2\rangle$ open up a decay channel into the dark ground state $|F = 1\rangle$, the probability of an atom reaching the closed $|F = 2, m_F = 2\rangle \rightarrow |F' = 3, m'_F = 3\rangle$ transition before a dark state in this scheme scales with the excited state hyperfine splittings over the natural linewidth $\omega_{1'3'}/\Gamma$ and $\omega_{2'3'}/\Gamma$.

For ^{87}Rb , $\omega_{2'3'}/\Gamma \approx 44$ whereas for ^{39}K , $\omega_{2'3'}/\Gamma \approx 3$, yielding a factor of 15 difference in this figure. It is thus much more likely for a ^{39}K atom to decay into a dark state, thus inhibiting

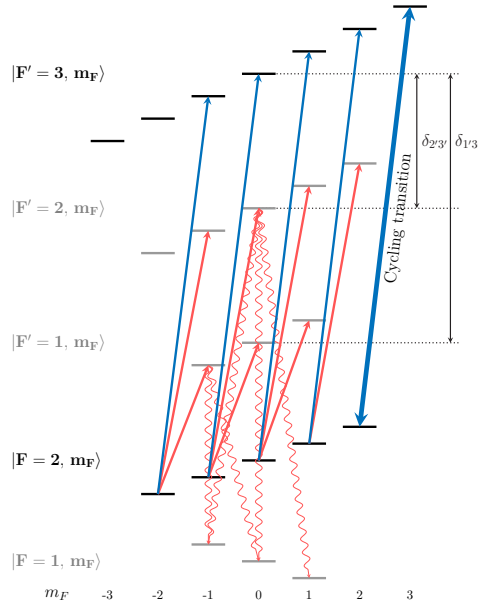


Figure 4.6: Optical pumping scheme with cycling $|F = 2, m_F = 2\rangle \rightarrow |F' = 3, m'_F = 3\rangle$ transition and dark $|F = 1\rangle$ ground state in a homogeneous magnetic field. Solid blue (red) lines display wanted (unwanted parasitic) optical transitions. Excitations to $|F' = 1\rangle$ and $|F' = 2\rangle$ open up possible decay paths into the dark $|F = 1\rangle$ state. Exemplary decay routes into $|F = 1\rangle$ are depicted by wavy red lines. Ideal σ^+ -polarization is assumed. For σ^- -polarization the system behaves fully symmetrically.

its contribution to a desired continuous fluorescence signal. In addition, the narrow excited state hyperfine splitting adds a comparably strong dependence of the detection laser detuning when making assumptions on the probability of reaching a cycling transition before a dark state is reached. This dependency is analyzed in a fully numerical simulation for ^{39}K yielding the fractional loss of an atom into $|F = 1\rangle$ over the detection laser detuning Δ_{det} and is shown in Figure 4.7.

Due to its narrow excited state hyperfine splitting, intuitive assumptions and experimental experiences are confirmed by the simulation. In order to minimize parasitic excitations to $|F' \neq 3\rangle$, a tight window for the detection laser detuning centered around $\approx \Gamma/4$ blue detuning to $|F' = 3\rangle$ remains. Tuning the laser closer to $|F' = 1, 2\rangle$ rapidly increases the scattering probability into these states and thus the decay probability into $|F = 1\rangle$. For larger detuning, that is blue detuned to all states, the difference in the scattering probability into $|F' = 3\rangle$ becomes negligible, thus increasing the loss rate again.

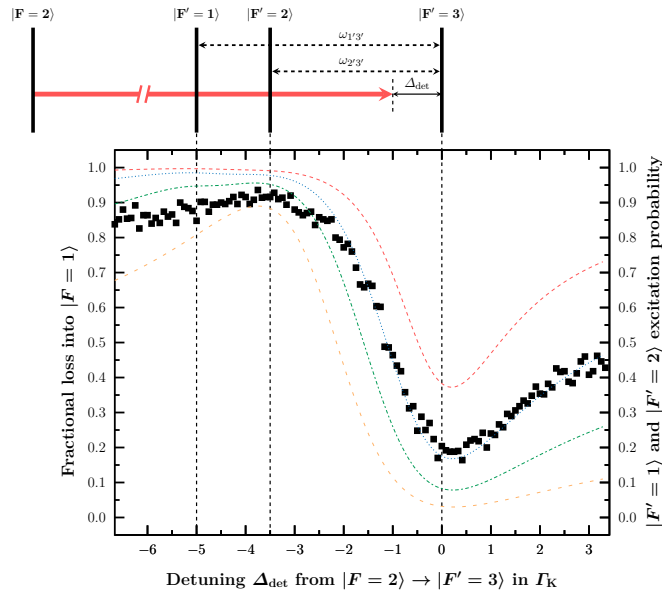


Figure 4.7: Loss simulation for fluorescence detection of ^{39}K . Black squares show the simulation result for the fractional loss into $|F = 1\rangle$ over the detuning. The red dashed, blue dotted, green dash-dotted, and orange loosely dashed curves display the scattering probability into $|F' \neq 3\rangle$ for states $|F = 2, m_F = -2 \dots 1\rangle$.

4.3 Coherent manipulation

In this Section, the coherent manipulation of potassium by means of stimulated RAMAN transitions will be introduced. Contrary to the theoretical assessment in Section 2.1, the approach chosen here will take a technical point of view. While the analysis in Section 4.3.1 holds for arbitrary species, a focus lays on the challenges imposed by the specific use of potassium when realizing a RAMAN matter wave interferometer. The importance of input state preparation and different methods for it, are discussed and compared in Section 4.3.3. The Section closes with a thorough overview of the first results obtained with the fully operational single species potassium interferometer (see Section 4.4).

4.3.1 Stimulated Raman transitions

Acting as the matter wave analogue to beam splitters and mirrors, stimulated RAMAN transitions [83] are the central instrument utilized for matter wave interferometry in this thesis. In the employed retroreflection setup with σ/σ -polarization¹ (see Section 3.3), a set of four parameters, namely: the ensemble temperature T_a , the quantization field B_q , the time of flight t_{TOF} before the pulse, and the degree of degeneracy n of the lower hyperfine state², qualitatively³ dictates the resulting two-photon transition spectrum. This spectrum can be obtained by applying a single RAMAN pulse with an overall detuning⁴ Δ with a fixed pulse width onto an ensemble prepared in the $|F = 1\rangle$ manifold and carefully tuning the RAMAN detuning from resonance $\delta = \omega_1 - \omega_2 - \omega_{12}$ around the hyperfine transition frequency as indicated in Figure 4.8. The RAMAN laser polarizations in this experiment exclusively allow transitions that fulfill $\Delta m_F = 0$. The light fields at frequencies ω_1 and ω_2 are retroreflected and thus yield three possible combinations. Starting from the $|F = 1\rangle$ manifold with a degree of degeneracy $n = 3$, each m_F substate, whose degeneracy is lifted by the quantization field, can hence be addressed with a triple of resonances. For the present configuration⁵, Figure 4.9 clarifies how

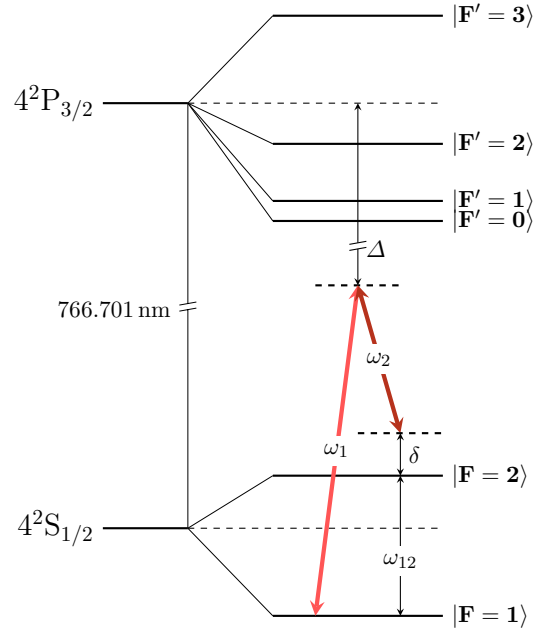


Fig. 4.8: Two-photon RAMAN transition coupling the hyperfine states $|F = 1\rangle$ and $|F = 2\rangle$ of $4^2S_{1/2}$ at a detuning Δ to the $4^2P_{3/2}$ multiplet. The RAMAN laser frequencies are ω_1 and ω_2 , and their detuning from resonance $\delta = \omega_1 - \omega_2 - \omega_{12}$. In this thesis, numerical values for Δ are stated with respect to the reference laser (see Appendix B).

¹ An overview on allowed transitions based on selection rules for a given combination of polarizations is for example provided in Ref. [131].

² More precisely: The state with lowest F .

³ Explicitly calculating the amplitude of the DOPPLER-sensitive transitions requires knowledge of the spatial overlap of the RAMAN beam and the atomic ensemble and is discussed in full detail below.

⁴ In this thesis, numerical values for Δ are stated with respect to the reference laser (see Appendix B). For calculations of the AC-STARK shift, for example, the effective detuning with respect to the ground state $|F = 2\rangle$ is lower due to the spectroscopy AOM, the crossover position, and the RAMAN switching AOM.

⁵ This analysis focuses on the special case in which the atomic center of mass velocity v , the gravitational acceleration g , and k_1, k_2 fulfill $v \parallel g \parallel k_1 \parallel k_2$.

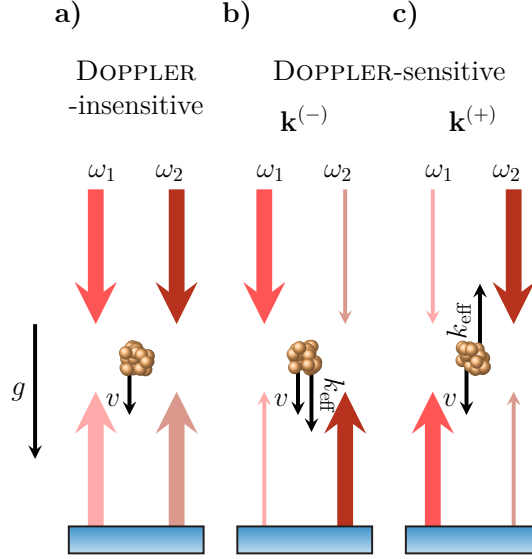


Figure 4.9: Two-photon transitions driven by light fields at frequencies ω_1 and ω_2 as evident in a retroreflected setup. An ensemble with center of mass velocity v and a constant gravitational acceleration g is assumed. For the DOPPLER-insensitive case (a), the transition is driven by both pairs of **copropagating** light fields yielding a net momentum transfer near zero. In Figures b) and c), DOPPLER-sensitive transitions with net momentum transfer of two photon momenta driven by **counterpropagating** light fields can be addressed by tuning $\delta = \omega_1 - \omega_2 - \omega_{12}$ such that the DOPPLER shift $\omega_D = k_{\text{eff}} \cdot v$ is compensated. With the atoms initially prepared the $|F = 1\rangle$ manifold ω_1 is absorbed first. Thus, the convention of naming the momentum transfer b) downward (c) upward) direction of momentum transfer $\mathbf{k}^{(-)}$ ($\mathbf{k}^{(+)}$) is followed.

these triples are composed. On the one hand, a single DOPPLER-insensitive transition¹ can be driven by the copropagating light fields as indicated in Figure 4.9 a). On the other hand, two pairs of the counterpropagating light fields at frequencies ω_1 and ω_2 with opposite signs in their DOPPLER shift can be resonant and drive DOPPLER-sensitive transitions (Figure 4.9 b) & c)). The terminology originates from the fact that the DOPPLER shift induced by relative motion with velocity v of the atomic ensemble with respect to a single light field (Equation (2.14))

$$\omega_D = k \cdot v$$

is common to a part in one million for the copropagating configuration and thus largely cancels out. In turn, for the counterpropagating case k_1 and k_2 have opposite signs. Thus, with $v = g \cdot t$ for a time t of free fall in a constant gravitational field and zero initial velocity, the DOPPLER shift and its time derivative for the two-photon light field $k_{\text{eff}} = k_1 - k_2$ are (Equation (2.16))

$$\alpha_D \equiv \frac{\omega_D(t)}{t} = k_{\text{eff}} \cdot g,$$

causing the DOPPLER shift per time of free fall to be typically on the order of $\alpha_D \approx 2\pi \cdot 25$ MHz/s. With the atoms initially prepared the $|F = 1\rangle$ manifold, the photon of frequency ω_1 is always

¹ In fact, this “single” transition is composed by two degenerate, copropagating transitions generated in the retroreflection setup.

absorbed first. Thus, the DOPPLER-sensitive transitions can be labeled following the convention $k^{(+)}$ for a momentum kick parallel to the gravitational acceleration and $k^{(-)}$ for the antiparallel direction.

Figure 4.10 shows a RAMAN resonance spectrum obtained by applying a single square-shaped RAMAN pulse with fixed width $\tau = 15 \mu\text{s}$ corresponding to a resolvable minimum temperature of $T_a = 440 \text{ nK}$ onto an ensemble prepared in the $|F = 1\rangle$ manifold. As explained above, a total of nine two-photon resonances is evident. Furthermore, another difference between the DOPPLER-sensitive and -insensitive transitions becomes evident. While the insensitive transitions are FOURIER transform limited¹, the DOPPLER-sensitive transitions naturally show a DOPPLER-broadening originating from the ensemble temperature due to their velocity-selective character [132]. For a free ensemble with temperature T and atomic mass m , the $1/\sqrt{e}$ radius in frequency space is [133]

$$\sigma_D = \frac{k_{\text{eff}}}{2\pi} \sqrt{\frac{k_B T}{m}}. \quad (4.2)$$

It is thus possible to infer the ensemble temperature in beam splitting direction from the frequency spectrum. For example, the $k^{(-)}$ transition addressing $m_F = 0$ in Figure 4.10 yields a temperature in vertical direction of $T_z = 32.6 \mu\text{K}$ corresponding to a deviation of $\approx 20\%$, as compared to the temperatures derived from a time-of-flight series in Section 4.1.3.

The preceding analysis allows to draw conclusions on how to constrain a sensible parameter space when taking preparations for matter wave interferometry². As a first prerequisite, this parameter space must allow for opening and closing an interferometer solely with the magnetically insensitive $m_F = 0$ state, i.e. the ‘‘comoving’’ DOPPLER-sensitive transitions exciting the $m_F = \pm 1$ must be lifted out of degeneracy. Furthermore, whenever the DOPPLER-sensitive $m_F = 0$ transition is degenerate with any magnetically sensitive transition, a corresponding magnetically sensitive excitation background causes normalization noise when detecting the interferometer output. As a second prerequisite, it is necessary to choose the free fall time before the first interferometer pulse t_{TOF} such that the DOPPLER shift due to gravity is larger than the ZEEMAN splitting of the $m_F = 0$ and $m_F = \pm 1$ states.

As evaluated in Section 2.1, lifting the m_F degeneracy and operating an interferometer on the $|F = 1, m_F = 0\rangle \leftrightarrow |F = 2, m_F = 0\rangle$ is desirable because of the vanishing linear ZEEMAN shift. With knowledge of Equation (4.2), one can derive a criterion on the minimum magnetic field amplitude to resolve the DOPPLER-broadened transitions for a given ensemble temperature. Defining ‘‘resolution’’ as a transition center separation of two times the $1/\sqrt{e}$ width, the quantization field must meet the condition

$$\begin{aligned} \Delta f_{\text{Zeeman}} &\stackrel{!}{=} 2\sigma_D, \\ \Leftrightarrow B_{q,\text{min}} &= \frac{h}{2g_F\mu_B} \frac{k_{\text{eff}}}{\pi} \sqrt{\frac{k_B T}{m}}. \end{aligned} \quad (4.3)$$

1 The natural linewidth of the two-photon transition is much narrower than the FOURIER transform of the excitation pulse.

2 The study presented here focuses on the ‘‘lowest possible’’ magnetic field amplitude. Scenarios in which the magnetic field is much higher are possible but shall not be discussed here.

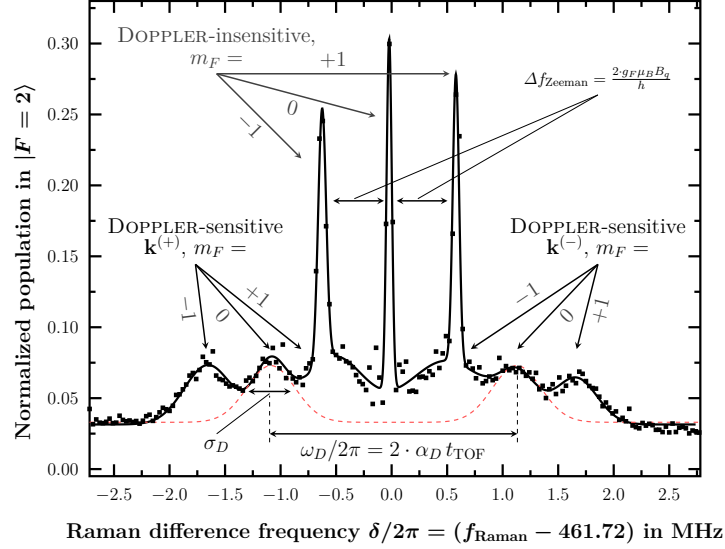


Figure 4.10: Typical RAMAN resonance spectrum obtained by scanning $\delta = \omega_1 - \omega_2 - \omega_{12}$ and applying single RAMAN pulses. The spectrum is acquired at the following parameters: $\tau = 15 \mu\text{s}$, $B_q = 430 \text{ mG}$, $t_{\text{TOF}} = 43.25 \text{ ms}$, $T_z = 32.6 \mu\text{K}$. To guide the eye, a fit function is plotted (solid black line). For simplicity, GAUSS functions are assumed for the DOPPLER-insensitive transitions. In addition, a DOPPLER-sensitive spectrum calculated with the aforementioned parameters for a purified $m_F = 0$ state is plotted (dashed red line). In the retroreflected setup using σ/σ -polarization, a total of nine resonances with $\Delta m_F = 0$ are visible, three of which form one subset of DOPPLER-**insensitive** transitions. The remaining two subsets of three DOPPLER-**sensitive** transitions each are labeled $k^{(+)}$ for upward and $k^{(-)}$ for downward momentum transfer. The separation of two neighboring m_F states within one subset is $2 \cdot g_F \mu_B B_q$, the $k^{(+)}$ and $k^{(-)}$ transitions addressing $m_F = 0$ are separated by $\omega_D/2\pi = 2 \cdot \alpha_D t_{\text{TOF}}$.

with g_F being the LANDÉ g -factor and μ_B the BOHR magneton, to fulfill the first criterion described above. Equation (4.3) yields $B_{q,\text{min}} = 311 \text{ mG}$ in the case of a potassium ensemble temperature of $T_a = 32.6 \mu\text{K}$. In order to satisfy the second condition, the free fall time before the first interferometer pulse t_{TOF} has to be chosen such that

$$\begin{aligned} \omega_D(t_{\text{TOF},\text{min}}) &\stackrel{!}{=} \Delta f_{\text{Zeeman}} + \sigma_D, \\ \Leftrightarrow t_{\text{TOF},\text{min}} &= \frac{2\pi}{g k_{\text{eff}}} 2g_F \mu_B B_q + \frac{1}{g} \sqrt{\frac{k_B T}{m}}, \end{aligned} \quad (4.4)$$

for given temperature T and quantization field B_q . Here, the first term accounts for the linear ZEEMAN shift the DOPPLER-insensitive magnetic transitions are subject to; The second term resembles an additional contribution maintaining a transition center separation of one $1/\sqrt{e}$ width. For typical parameters, Equation (4.4) gives $t_{\text{TOF},\text{min}} = 32 \text{ ms}$. Substituting $B_q \rightarrow B_{q,\text{min}}$ from Equation (4.3), Equation (4.4) can be simplified to

$$t_{\text{TOF},\text{min}} = \frac{3}{g} \sqrt{\frac{k_B T}{m}}. \quad (4.5)$$

Accordingly, cold ensemble temperatures reduce the minimum time required before applying the first RAMAN pulse. Not only because of making full use of available free fall time for the

interferometer cycle, but also achieving a cold ensemble temperature and performing an m_F purification relaxes constraints imposed on the experiment. There exist several input state preparation strategies to ease the operation of an atom interferometer. These methods and the influence of the ensemble temperature shall be discussed in Section 4.3.3.

4.3.2 One-photon AC-Stark shift

Besides the desired coupling of two states, the RAMAN light field exerts energy shifts onto an atomic system by off-resonant coupling. On the one hand, coupling of off-resonant one-photon transitions changes transition frequencies of the two-photon transitions that are driven in an interferometer. Correspondingly, this AC-STARK shift causes phase shifts that affect an interferometer. Because of the inherent differences to rubidium, the one-photon AC-STARK shift is treated in this Section. On the other hand, the two-photon light shift, which imposes phase shifts due to coupling of off-resonant two-photon transitions, is explained in Section 5.2. In general, the frequency shift induced by an off-resonant light field with related RABI frequency Ω and detuning ω coupling two states is given by [133]

$$\omega^{\text{AC}} = \frac{\Omega^2}{4\omega}. \quad (4.6)$$

In Figure 4.11, a two-photon light field with frequencies ω_1 and ω_2 via an intermediate state $|i\rangle$ at a red overall detuning¹ Δ coupling a system of two states $|g\rangle$ and $|e\rangle$ with energy difference ω_{12} is considered. Using Equation (4.6) and summing over the coupling of $|j\rangle$ ($j \in e, g$) to the excited state multiplet states $|k\rangle$, e.g. the $4^2P_{3/2}$ fine structure state, via the light fields ω_1 and

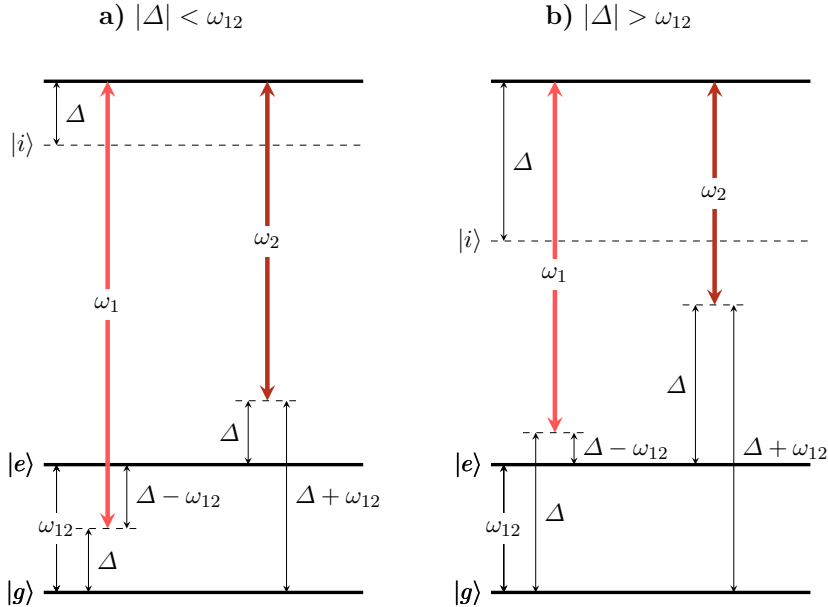


Figure 4.11: Two-photon light field coupling states $|g\rangle$ and $|e\rangle$, which are separated by $h\omega_{12}$, via the intermediate state $|i\rangle$ for the case a) $|\Delta| < \omega_{12}$ and b) $|\Delta| > \omega_{12}$. Modified from Ref. [117].

¹ The assessment in this Section behaves completely symmetric for the case in which the overall detuning is blue with respect to the single-photon transitions.

ω_2 , the AC-STARK shift is

$$\omega_j^{\text{AC}} = \sum_k \frac{\Omega_{k,1}^2}{4\omega_{k,1}} + \sum_k \frac{\Omega_{k,2}^2}{4\omega_{k,2}}. \quad (4.7)$$

Here, $\omega_{k,1}$ and $\omega_{k,2}$ are the detunings of light fields ω_1 and ω_2 to the multiplet state $|k\rangle$. Taking into account the selection rules for circular polarization of the RAMAN laser light and weighing the contributions by their CLEBSCH-GORDON coefficients [88], the AC-STARK shifts of states $|g\rangle$ ($|F=1\rangle$) and $|e\rangle$ ($|F=2\rangle$) in the case of ^{39}K are expressed using Equation (4.7):

$$\begin{aligned} \omega_g^{\text{AC}} = & \frac{|\Omega_1|^2}{4} \left(\frac{5}{24\Delta_{1'}} + \frac{1}{8(\Delta_{1'} - \omega_{1'2'})} \right) \\ & + \frac{|\Omega_2|^2}{4} \left(\frac{5}{24(\Delta_{1'} - \omega_{12})} + \frac{1}{8(\Delta_{1'} - \omega_{1'2'} - \omega_{12})} \right), \end{aligned} \quad (4.8)$$

$$\begin{aligned} \omega_e^{\text{AC}} = & \frac{|\Omega_2|^2}{4} \left(\frac{1}{120\Delta_{1'}} + \frac{1}{8(\Delta_{1'} - \omega_{1'2'})} + \frac{1}{5(\Delta_{1'} - \omega_{1'3'})} \right) \\ & + \frac{|\Omega_1|^2}{4} \left(\frac{1}{120(\Delta_{1'} + \omega_{12})} + \frac{1}{8(\Delta_{1'} - \omega_{1'2'} + \omega_{12})} + \frac{1}{5(\Delta_{1'} - \omega_{1'3'} + \omega_{12})} \right), \end{aligned} \quad (4.9)$$

where $\omega_{1'k'}$ is the difference frequency between state $|F'=1\rangle$ and $|F'=k\rangle$, and $\Delta_{1'}$ is the overall RAMAN detuning with respect to the excited hyperfine state $|F'=1\rangle$. In Figure 4.11 a) & b), two cases, $|\Delta| < \omega_{12}$ and $|\Delta| > \omega_{12}$, are depicted. For $|\Delta| < \omega_{12}$, ω_1 is red-detuned to $|g\rangle \rightarrow |i\rangle$ and blue-detuned to $|e\rangle \rightarrow |i\rangle$, and exerts frequency shifts with opposite signs on these transitions. The field ω_2 is red-detuned to both transitions. In this case, the differential AC-STARK shift, which is proportional to measurable phase shifts in an interferometer,

$$\omega_{\text{diff}}^{\text{AC}} \equiv \omega_g^{\text{AC}} - \omega_e^{\text{AC}} \quad (4.10)$$

can be nulled making use of the proportionality $\Omega_j \propto \sqrt{I_j}$ in Equation (2.5) and choosing an intensity ratio I_2/I_1 such that $\omega_{\text{diff}}^{\text{AC}} = 0$. On the contrary, if $|\Delta| > \omega_{12}$, both ω_1 and ω_2 are red-detuned to $|g\rangle \rightarrow |i\rangle$ and $|e\rangle \rightarrow |i\rangle$ and the differential AC-STARK shift can not be nulled.

Figure 4.12 shows the calculated intensity ratios I_2/I_1 yielding $\omega_{\text{diff}}^{\text{AC}} = 0$ in dependence of the detuning Δ for a) ^{39}K , and b) ^{87}Rb . Given two criteria, namely a high RABI frequency $\Omega_{\text{eff}} \propto \sqrt{I_1 \cdot I_2}$ (Equation (2.6)), which requires a ratio $I_2/I_1 \approx 1$, and a detuning Δ large enough to keep single-photon scattering causing decoherence at a minimum. Unfortunately, in the case of ^{39}K detunings Δ yielding a ratio $I_2/I_1 \approx 1$ are in the range of $\Delta \approx 2\pi \cdot 200$ MHz yielding an unacceptably high single photon scattering rate. In turn, use of ^{87}Rb conveniently allows one to choose detunings of up $\Delta \approx 2\pi \cdot 2.5$ GHz with an intensity ratio for $I_2/I_1 \approx 2.5$.

The analysis present here shows the inherent problems that occur, when working with species that have a small hyperfine energy splitting, e.g. bosonic potassium¹. Effectively, the condition $\Delta < \omega_{12}$ for AC-STARK compensation dictates very low detunings Δ for ratios I_2/I_1 that keep up a reasonably high RABI frequency and practically inhibits AC-STARK compensation. Instead, a

¹ A related problem concerning the AC-STARK shift will rise in future experiments [59, 60] employing ultracold ensembles or non-classical states demanding very large RAMAN detunings in order to further suppress single photon scattering.

large detuning $\Delta \gg \omega_{12}$ is chosen in this thesis and a ratio $I_2/I_1 = 1$ allows a maximum effective RABI frequency.

Estimation of the AC-Stark-induced phase shift

An estimate for the phase shift induced by the AC-STARK effect in a potassium interferometer can be computed by evaluating the spatial convolution of $\omega_{\text{diff}}^{\text{AC}}(t)$ (Equation (4.10)) induced by a GAUSS-shaped RAMAN beam and a freely expanding atomic ensemble in dependence of the evolution time. The result yields a mean AC-STARK shift, which can then be employed to evaluate the phase shift on an interferometer utilizing the sensitivity formalism described in Section 2.1. Numerically evaluating the integral

$$\Delta\Phi^{\text{AC}} = \int_{-\infty}^{\infty} g_{s,\text{MZ}}(t) \zeta(t) \omega_{\text{diff}}^{\text{AC}}(t) dt \quad (4.11)$$

with the sensitivity function $g_{s,\text{MZ}}(t)$ (Equation (2.26)) an additional function $\zeta(t)$, that $\equiv 1$ during the RAMAN light pulses, allows to infer the phase shift due to the AC-STARK shift. For typical parameters¹, a phase shift of $\Delta\Phi^{\text{AC}} = -114 \text{ mrad}$ and a related bias acceleration of $-1.74 \times 10^{-5} \text{ m/s}^2$ can be expected. Assuming RAMAN power and detuning drifts² that are sufficiently slow compared to the time required to obtain to fringes with opposite sign of k_{eff} , phase shifts $\Delta\Phi^{\text{AC}}$ induced by the AC-STARK shift can be suppressed by using the k -reversal scheme (see Section 4.4.2). An analysis of the total RAMAN power fluctuations on a single cycle

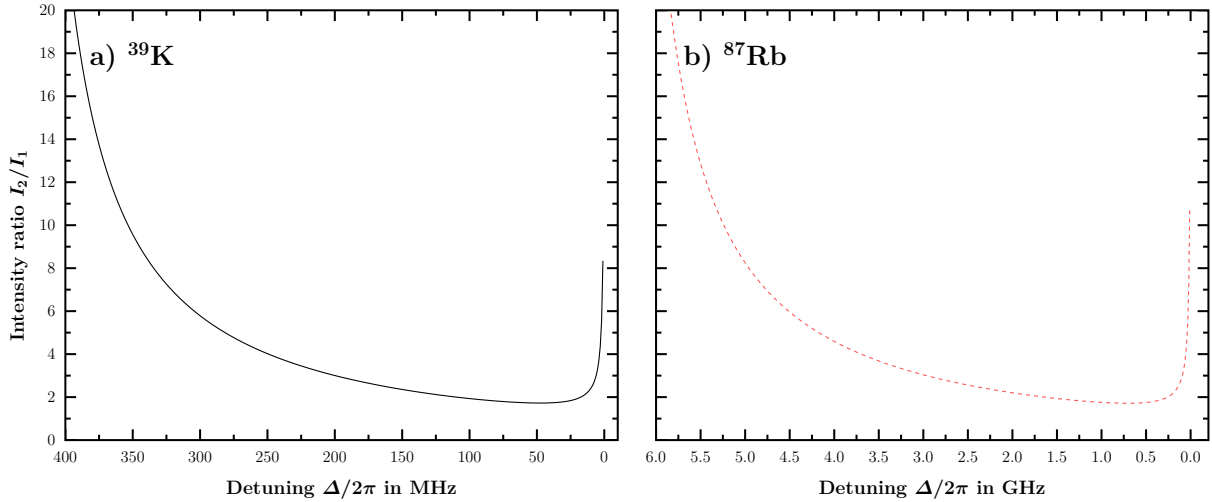


Figure 4.12: RAMAN laser frequency intensity ratio I_2/I_1 yielding a nulled differential AC-STARK shift $\omega_{\text{diff}}^{\text{AC}}$ in dependence of the detuning Δ for a) ^{39}K , and b) ^{87}Rb .

- 1 The calculation is based on a freely expanding ^{39}K ensemble with a temperature of $T_a = 32 \mu\text{K}$, a $1/\sqrt{e}$ initial size of $\sigma_0 = 1 \text{ mm}$, and a free fall time $t_{\text{TOF}} = 43 \text{ ms}$ before the first RAMAN pulse. For the beam splitting light field, a total RAMAN power of 200 mW at a 1:1 power ratio of the two frequencies, a $1/e^2$ radius of 9.6 mm, a red detuning $\Delta = 2\pi \cdot 3.3 \text{ GHz}$, a pulse separation time of $T = 20 \text{ ms}$, and a π -pulse width $t_\pi = 15 \mu\text{s}$ are assumed.
- 2 Here, the assumption that fluctuations of the RAMAN pulse width, the pulse separation time, and the RABI frequency, all of which change the sensitivity function, and fluctuation of the RAMAN power ratio, are negligible as compared to total power fluctuations, is made.

time scale using a monitor pulse at the end of a sequence (see Section 4.2) yielded a shot-to-shot noise of 0.92% corresponding to AC-STARK-induced noise at a level of $\approx 1.60 \times 10^{-7} \text{ m/s}^2$. The inferred noise can hence not be resolved at the current level of short-term stability (see Section 4.4.2). Furthermore, no power drift limiting the suppression of the AC-STARK bias on the time scale one k -reversal cycle could be observed. A measurement of the long-term power drift allows to derive a suppression of the AC-STARK bias term by 4 orders of magnitude to a level of $\approx 1.32 \times 10^{-9} \text{ m/s}^2$.

4.3.3 Input state preparation

One lever to increase the relative excitation in a single pulse or the contrast of an interferometer is reducing the degree of degeneracy n of the ensemble by m_F purification. For example, applying a pulse onto the $|F = 1\rangle$ manifold with a degree of degeneracy $n = 3$ as displayed in Figure 4.10 yields a maximum relative excitation probability $1/n \approx 0.33$. Equally important, the ensemble temperature plays an essential role when driving DOPPLER-sensitive transitions. It imposes constraints on experimental parameters such as the quantization field and the time of free fall before the first RAMAN pulse. Furthermore it affects the maximum excitation that is feasible in a single pulse and thus is an important factor when estimating the contrast that is achievable in an interferometer. Finally, for a finite RAMAN beam size with GAUSSIAN profile, the ensemble expansion transverse to the direction of beam splitting induces a spatially inhomogeneous RABI frequency and leads to dephasing and a loss of maximum excitation for larger expansion times.

Optical pumping

Any deviation from a pure input state diminishes the achievable contrast when projecting the interferometer states in the detection process [82]. After loading the potassium 3D MOT, the final sub-DOPPLER cooling step (see Section 4.1.3) naturally accumulates a large fraction in the $|F = 1\rangle$ state making use of a gray molasses technique [119]. In order to initialize a pure input state, the repumping light is switched off completely for a duration of 1 ms causing optical pumping into the dark $|F = 1\rangle$ state by the end of the cooling sequence. The outcome is a pure $|F = 1\rangle$ state with the atoms equidistributed over the m_F substates that can be used as an input for the interferometer. Likewise, it is possible to pump all atoms into the $|F = 2\rangle$ manifold by turning off the cooling laser in the final stage of the sub-DOPPLER cooling sequence. However, because of the higher degree of degeneracy ($n = 5$) this is typically unfavorable unless combined with subsequent state preparation steps.

Magnetic substate purification

As mentioned above, reducing the degree of degeneracy allows for higher contrast in a relation inversely proportional at the cost of removing a fraction of the initial atom number. Once lifted out of degeneracy by a magnetic field, the different magnetic substates can be addressed by means of magnetic dipole transitions employing a radio frequency source (see Section 3.1.2). Both hyperfine ground states are very long-lived causing the natural linewidth to be extremely narrow. In this regime, spontaneous emission is practically zero and resolving the transition is always FOURIER transform limited allowing for a very high fidelity.

Figure 4.13 shows a typical magnetic substate purification sequence. Initially, the atomic ensemble is optically pumped into the $|F = 2\rangle$ manifold with all magnetic substates equally populated. Subsequently, an m_F state selection is performed by applying a high fidelity radio frequency π -pulse on the $|F = 2, m_F = 0\rangle \rightarrow |F = 1, m_F = 0\rangle$ transition that ideally transfers a fraction of 20% of all atoms. Finally, the atoms remaining in the $|F = 2\rangle$ manifold are removed by resonant scattering of photons on the $|F = 2\rangle \rightarrow |F' = 3\rangle$ transition. Commonly a traveling wave is used

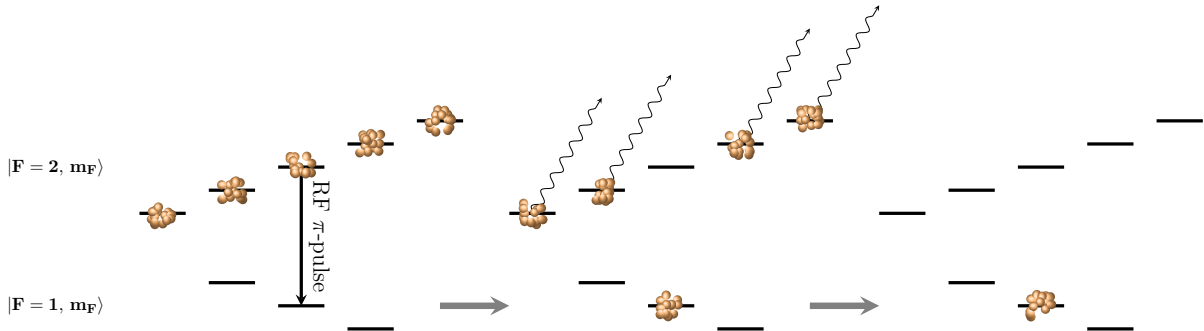


Figure 4.13: Simplified magnetic substate purification sequence. The ensemble is initially prepared in the $|F = 2\rangle$ manifold with the atoms equidistributed over all magnetic substates. Coherent radio frequency manipulation allows to transfer a fraction of 20 % of all atoms in to the $|F = 1, m_F = 0\rangle$ state. Finally, atoms remaining in $|F = 2\rangle$ are removed using resonant scattering of photons.

to remove unwanted atoms by imbalanced light pressure. As the energy level structure requires well defined polarization and quantization axis to address cycling transitions (see Section 4.2), a standing wave created using the detection light path (see Section 3.3) is used. A separate traveling wave, e.g. in the horizontal plane, could be used to apply light pressure for atom removal and has been demonstrated in the present apparatus for rubidium. For potassium, however, this approach is linked to adiabatically switching to a horizontally oriented magnetic field which would impose additional constraints to the timing and make the experimental sequence more complicated. Contrary to light pressure, this mechanism removing the atoms is based on heating the unwanted fraction. Sufficient heating causes much higher expansion rates as compared to the remaining atoms. In this way the heated fraction is prone to losses when colliding with the walls of the falling tube. Residual heated atoms fall into the detection zone at very low densities and thus do not contribute strongly to the detection signal. The removal mechanism is relying on cycling transitions which do not exist for the $|F = 1\rangle$ manifold. All state preparation techniques are hence designed such that at the end of the sequence the fraction to be removed is situated in the $|F = 2\rangle$ state.

Alternatively, the described state preparation process can be enhanced in terms of the final atom number by enrichment of the $m_F = 0$ state via additional optical pumping. Starting from the $|F = 1\rangle$ manifold, a first radio frequency π -pulse transfers $\approx 33\%$ of all atoms into the $|F = 2, m_F = 0\rangle$ state. Afterwards, a repumping pulse allows to redistribute all remaining atoms from $|F = 1\rangle$ over the $|F = 2\rangle$ manifold, hence adding an additional fraction of $2/3 \cdot 1/5 \approx 13\%$. A second radio frequency pulse and a following removal of the remaining atoms as described in the simplified sequence above yields a total of $\approx 46\%$ prepared in $|F = 1, m_F = 0\rangle$.

Velocity selection

Already in 1991 it was shown in Ref. [132] that the velocity-selective character of two counterpropagating lasers can be used to select a narrow velocity slice out of an atomic ensemble with a given velocity distribution with width σ_D . Here, advantage is taken of the fact that the two-photon transition can be applied for long time scales τ such that the FOURIER transform width $\sigma_p \propto 1/\tau$ of the pulse fulfills the relation $\sigma_p \ll \sigma_D$. The velocity interval in beam splitting direction that is selected by σ_p can then be assigned a temperature equivalent to the analysis in Section 4.3.1. Recalling the generalized DOPPLER shift (Equation (2.14)) & Equation (4.2) can

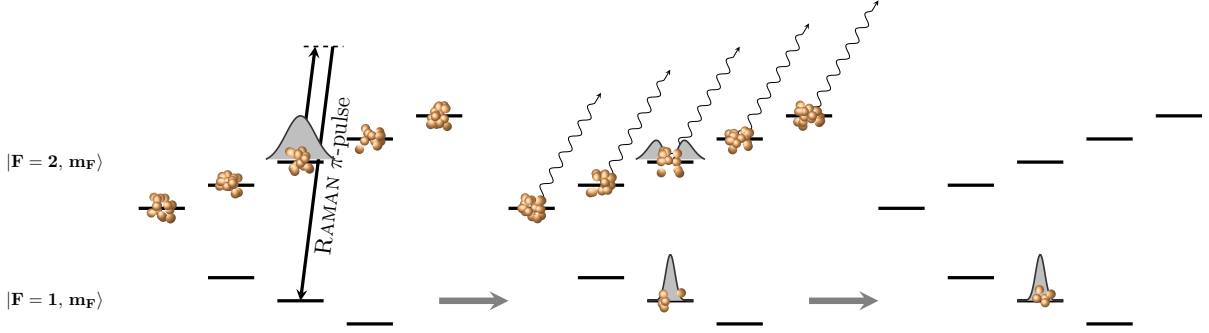


Figure 4.14: Simplified velocity selection sequence. The ensemble is initially prepared in the $|F = 2\rangle$ manifold with the atoms equidistributed over all magnetic substates. A velocity-selective RAMAN pulse allows to transfer a narrow velocity class into $|F = 1, m_F = 0\rangle$. In the subsequent step, atoms remaining in $|F = 2\rangle$ are removed using resonant scattering of photons.

be solved for the temperature yielding

$$T_z = \frac{m}{k_B} \left(\frac{2\pi\sigma_p}{k_{\text{eff}}} \right)^2. \quad (4.12)$$

In the following, an ideal square pulse of full width τ with the associated power spectrum in frequency space

$$F(f) = A \cdot \left(\frac{\sin(\pi\tau \cdot f)}{\pi\tau \cdot f} \right)^2 \quad (4.13)$$

with a normalization factor A is assumed. The $1/\sqrt{e}$ radius¹ σ_p then is

$$\begin{aligned} F(\sigma_p) &= \frac{A}{\sqrt{e}}, \\ \Leftrightarrow \sigma_p &\approx 0.38 \cdot \frac{1}{\tau}. \end{aligned} \quad (4.14)$$

Hence for a square pulse with width τ , Equation (4.12) can be rewritten as

$$T_z \approx \frac{m}{k_B} \left(\frac{0.76\pi}{k_{\text{eff}}\tau} \right)^2. \quad (4.15)$$

A typical temperature corresponding to a potassium ensemble velocity-selected with a square pulse $\tau = 15 \mu\text{s}$ is thus $T_z = 440 \text{ nK}$ in beam splitting direction; significantly lower temperatures have been accomplished with longer pulses using sodium and cesium [46, 132]. A simple velocity selection process is depicted in Figure 4.14. The sequence is indeed very similar to the magnetic substate purification (Figure 4.13). Instead of the radio frequency pulse, a velocity-selective RAMAN transition is employed to transfer a narrow velocity class into $|F = 1, m_F = 0\rangle$ before clearing the $|F = 2\rangle$ state from remaining atoms. Clearly, the described sequence performs an m_F state selection as well. However, as assessed in detail in Section 4.3.4 the fraction of atoms

¹ Equation (4.12) only holds for equilibrium temperature distributions with GAUSSIAN shape, however, for the central peak of a distribution $\propto \sin(x)/x$ a GAUSS function is a good approximation.

that can be transferred by a velocity selection pulse is strongly limited by the convolution of the ensemble's initial velocity distribution with the RAMAN pulse FOURIER transform. Hence, the transferable fraction is far away from the $\approx 46\%$ that can be achieved in a purely radio frequency based state preparation. Schemes based on a combination of radio frequency transfer and velocity selection can enhance the fraction that is prepared as shown in Figure 4.15.

4.3.4 Influence of the ensemble temperature in a Doppler-sensitive transition

It is obvious, that the reduction in the effective temperature, which can be realized by velocity selection as described in Section 4.3.3, has to come at a cost. Naturally, the convolution of an ensemble's velocity and spatial distribution with the RAMAN pulse FOURIER transform and the spatial profile of the beam also determine the relative excitation probability that can be attained [134]. Accordingly, the temperature decrease accomplished with two-photon velocity selection is directly linked to an atom number reduction. With knowledge of the RAMAN beam and pulse characteristics, the ensemble temperature and its expansion time dynamics it is possible to quantitatively understand the influence of the ensemble temperature on the maximum possible excitation that can be achieved in a RAMAN pulse.

The spatially dependent RABI frequency in a GAUSSIAN beam with a $1/e^2$ radius of σ_L is

$$\Omega_0(r) = \Omega_0 \cdot e^{-2\left(\frac{r}{\sigma_L}\right)^2} \quad (4.16)$$

with a maximum frequency of $\Omega_0 = \pi/\tau_\pi$. For an atom with subject to a DOPPLER shift induced by velocity v in beam splitting direction (Equation (2.14)), the off-resonant effective RABI frequency [82]

$$\Omega_{\text{eff}}(r,v) = \sqrt{(\Omega_0(r))^2 + (k_{\text{eff}} \cdot v)^2} \quad (4.17)$$

allowing to express the excitation probability of an atom at radial position r with velocity v [135]:

$$p(r,v,t) = \left(\frac{\Omega_0(r)}{\Omega_{\text{eff}}(r,v)}\right)^2 \cdot \sin\left(\frac{\Omega_{\text{eff}}(r,v)}{2}t\right). \quad (4.18)$$

The velocity probability distribution for an ensemble with particles of mass m and and temperature T^z is given by the 1D MAXWELL-BOLTZMANN distribution [136]

$$f(v) = \sqrt{\frac{m}{2\pi k_B T^z}} \cdot e^{-\frac{1}{2} \frac{mv^2}{k_B T^z}}. \quad (4.19)$$

For a thermal ensemble with two-dimensional spatial distribution

$$n(r,t) = \frac{1}{2\pi \sigma_a^2(t)} \cdot e^{-\frac{1}{2}\left(\frac{r}{\sigma_a(t)}\right)^2} \quad (4.20)$$

the expansion dynamics are fully described by [130]

$$\sigma_a(t) = \sqrt{\frac{k_B T^{x,y}}{m} t^2 + \sigma_{a,0}^2} \quad (4.21)$$

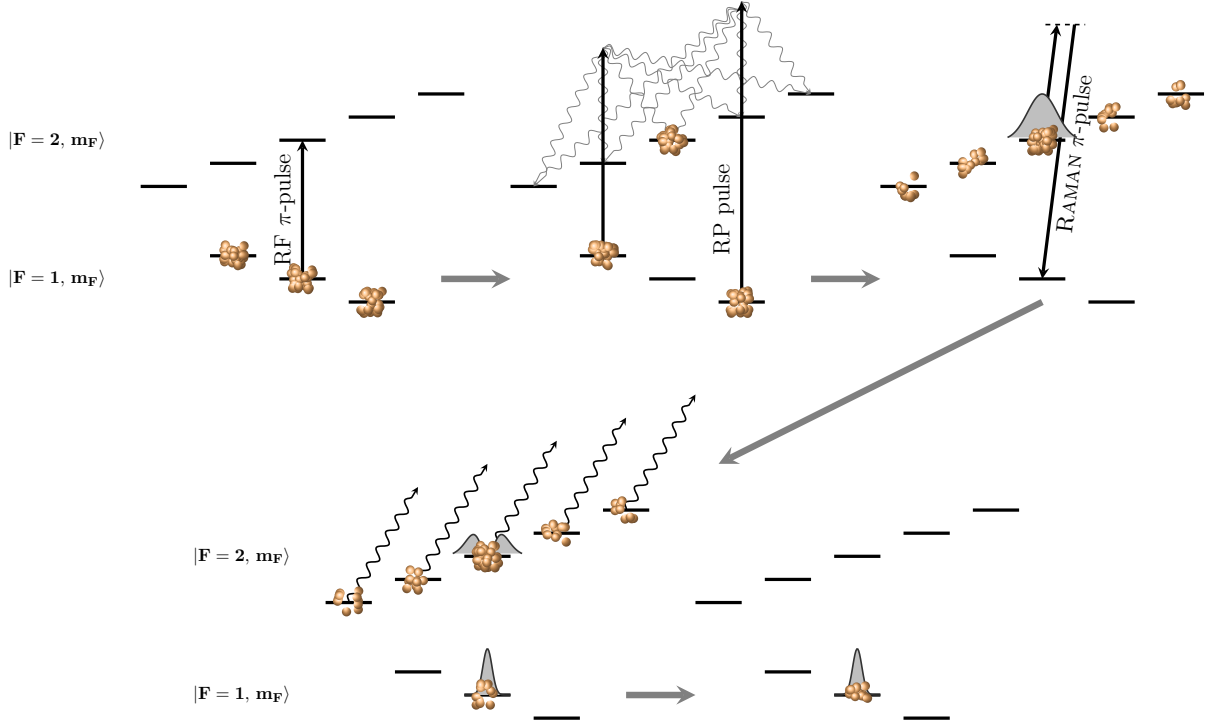


Figure 4.15: Enhanced velocity and magnetic selection sequence. The ensemble is initially prepared in the $|F=1\rangle$ manifold with the atoms equidistributed over all magnetic substates. Coherent radio frequency manipulation allows to transfer a fraction of $\approx 33\%$ of all atoms in to the $|F=2, m_F=0\rangle$ state and the following optical pumping distributes remaining $|F=1\rangle$ atoms over the $|F=2\rangle$ manifold, adding $\approx 13\%$ to $|F=2, m_F=0\rangle$. A subsequent velocity-selective RAMAN pulse allows to transfer a narrow velocity class back into $|F=1, m_F=0\rangle$. Finally, atoms remaining in $|F=2\rangle$ are removed using resonant scattering of photons.

with $\sigma_{a,0}$ being the initial cloud size. Equation (4.21) includes the characteristic expansion velocity of a thermal ensemble

$$v_{\text{exp}} = \sqrt{\frac{k_B T^{x,y}}{m}}. \quad (4.22)$$

Using the foregoing analysis, the excitation that can be accomplished with a DOPPLER-sensitive pulse can be obtained by calculating the convolution [135]

$$P(t, t_{\text{exp}}) = 2\pi \iint r \cdot f(v) \cdot n(r, t + t_{\text{exp}}) \cdot p(r, v, t) \, dr \, dv. \quad (4.23)$$

Here, arbitrary times t_{exp} can be chosen as a time offset such that free expansion in the RAMAN beam during free fall prior to the pulse is taken into account. As an example, numerically evaluating Equation (4.23) allows to derive the time dynamics of the relative population of $|F=2\rangle$. Figure 4.16 a) depicts RABI oscillations for a ^{39}K ensemble at temperature $T_K^{3D} = 25 \mu\text{K}$ and $t_{\text{exp}} = 0 \text{ ms}$ with an assumed RABI frequency of $\Omega_0 = \pi/15 \mu\text{s}$. As a cause of dephasing induced by the inhomogeneous effective RABI frequency (Equation (4.17)) due to the ensembles velocity spread, the RABI oscillations are damped. In Figure 4.16 b), experimental data obtained by scanning the RAMAN pulse width applied on to magnetically purified state (Figure 4.13) after

$t_{\text{exp}} = 43$ ms can be well correlated when taking into account spontaneous emission¹ and correcting for an offset caused by the detection. More generally, evaluating the integral Equation (4.23) allows to map the feasible maximum RAMAN excitation onto a two-dimensional parameter space consisting of the ensemble's expansion time and its temperature. Figure 4.17 a) shows the feasible RAMAN excitation in a contour plot over the parameters: expansion time t_{exp} and the expansion velocity v_{exp} of the $1/\sqrt{e}$ width of an atomic ensemble. Here, using the expansion velocity instead of the temperature using Equation (4.22) is favorable in order to provide a way to compare the resulting data independently of the atomic species. Figure 4.17 a) was computed numerically for a range of expansion velocities corresponding to potassium ensemble 3D temperatures² between $T^{3\text{D}} = 50$ nK . . . 50 μK , and expansion times $t_{\text{exp}} = 0$ ms . . . 200 ms constrained by the maximum free fall time in the vacuum chamber used in this thesis. For the simulation, the expansion dynamics of a free thermal gas with a degree of degeneracy of $n = 1$ and a fixed initial size of $\sigma_{a,0} = 1$ mm are assumed for simplicity. As the effective RABI frequency varies throughout the parameter space, the displayed excitation values represent global maxima obtained by scanning the corresponding pulse width around $\tau_{\pi} = 15$ μs . In Figure 4.17 b), a RAMAN π -pulse width of $\tau_{\pi} = 15$ μs is considered and the maximum excitation over the expansion time is plotted for two typical 3D temperatures, namely ^{39}K at $T_{\text{K}}^{3\text{D}} = 25$ μK and ^{87}Rb at $T_{\text{Rb}}^{3\text{D}} = 5$ μK . While the low expansion time limit is governed by the ensemble temperature in beam splitting direction, the influence of transverse expansion of the gas is dominating for longer expansion times and explains the more benign behavior of ^{87}Rb with its higher mass and typically lower temperature

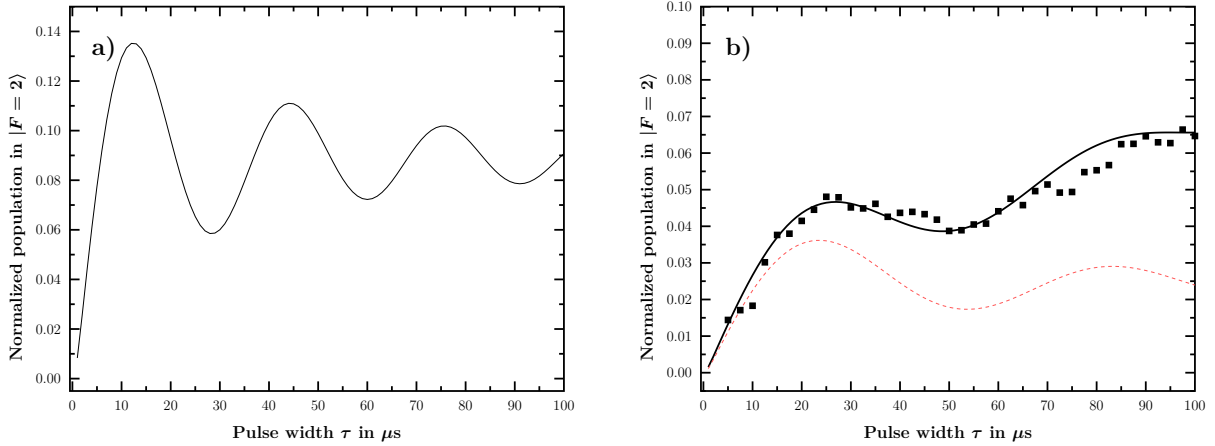


Figure 4.16: a) RABI oscillations for a ^{39}K ensemble at temperature $T_{\text{K}}^{3\text{D}} = 25$ μK and $t_{\text{exp}} = 0$ ms with an assumed RABI frequency of $\Omega_0 = \pi/15$ μs . b) RABI oscillations ($t_{\text{exp}} = 43$ ms) obtained by scanning the RAMAN pulse width applied on to magnetically purified state (black squares) and corresponding simulated data taking into account spontaneous emission (solid black line). The data is corrected for a signal offset caused by the detection. The dashed red line represent the simulation data without spontaneous emission.

- 1 The simulation data in Figure 4.16 b) is altered by adding a spontaneous emission component that is linear in time and based on experimental data. It represents a first order approximation of the optical pumping of the two level system by single photon scattering.
- 2 For the calculation of Figure 4.17 a), isotropic temperatures are explicitly assumed in order to emulate the conditions before a state preparation RAMAN pulse or the first interferometer pulse without further state preparation. For the two specific examples, the degree of degeneracy $n \neq 1$ has to be taken into account.

as compared to ^{39}K . The influence of transverse motion becomes even more significant in the third case plotted in Figure 4.17 b) which displays a ^{39}K ensemble with anisotropic temperature $T_{\text{K}}^{x,y} = 25 \mu\text{K}$ and $T_{\text{K}}^z = 440 \text{ nK}$ after velocity selection with a pulse $\tau = 15 \mu\text{K}$. Due to the low temperature in beam splitting direction the excitation probability is near unity for low expansion times. For longer times however a crossing with the curve plotted for ^{87}Rb is imminent already at $t_{\text{exp}} \approx 60 \text{ ms}$.

One obvious conclusion of this simulation is that even though velocity selection can help in realizing temperatures in beam splitting direction that are significantly lower than the initial temperature, the transverse expansion plays a very important role when facing long expansion times that are inherently linked to interferometers with long pulse separation times. As can be seen from Equation (4.22), the transverse expansion plays an increasingly important role when working with atoms with lighter mass. Moreover, while velocity selection can increase the maximum excitation for short times, lines as marked in Figure 4.17 a) may only be parallel shifted yielding higher excitation when realizing lower three-dimensional temperatures, e.g. when using BOSE-EINSTEIN condensates or applying techniques such as delta-kick cooling [58, 137] as discussed in Chapter 6.

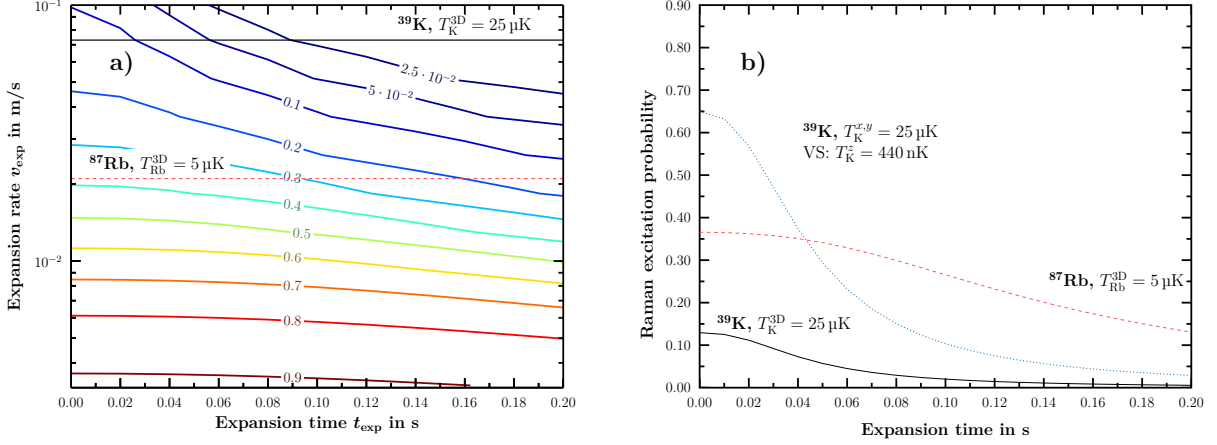


Figure 4.17: a) Surface plot of simulation of RAMAN excitation probability in dependence of the expansion time and velocity. The dashed lines mark two typical expansion velocities for ^{87}Rb ($T_{\text{Rb}}^{3\text{D}} = 5 \mu\text{K}$) and ^{39}K ($T_{\text{K}}^{3\text{D}} = 25 \mu\text{K}$). The corresponding maximum RAMAN excitations in dependence of the expansion time are plotted in b) (solid black line and dashed red line). For comparison, the blue dotted line shows a ^{39}K ensemble with anisotropic temperature after velocity selection ($T_{\text{K}}^{x,y} = 25 \mu\text{K}$ and $T_{\text{K}}^z = 440 \text{ nK}$).

4.4 Measurements of local gravitational acceleration

Using the methods explained in this Chapter, it was possible to perform the first inertial-sensitive measurements using potassium. In this Section, an introduction into the measurement protocol is provided and the first results are presented. A long term measurement was performed yielding an absolute value for the local gravitational acceleration.

4.4.1 Experimental methods

A typical measurement cycle is performed as follows. Within 1 s, the 3D MOT is loaded with $\approx 1 \times 10^8$ atoms of ^{39}K , and the ensemble is subsequently cooled down to $T_a \approx 20 \mu\text{K}$ using the methods described in Section 4.1. After optically pumping all atoms into the $|F = 1\rangle$ manifold at the end of the sub-DOPPLER cooling stage, the atoms are released into free fall by turning off all cooling light fields using the responsible acousto-optical modulator and shutter (see Section 3.2.1). The RAMAN detuning, that coherently couples $|F = 1, m_F = 0\rangle \rightarrow |F = 2, m_F = 0\rangle$ is operated at a RAMAN detuning $\Delta = 2\pi \cdot 3.3 \text{ GHz}$ and the typical π -pulse width is $\tau_\pi = 15 \mu\text{s}$. Applying a pulse sequence consisting of a $\pi/2$ -, a π -, and a $\pi/2$ -pulse, transferring $\hbar k_{\text{eff}}$ momentum each, and separated in time by the pulse separation time T , and simultaneously applying a constant frequency change rate α on the RAMAN difference frequency, the atomic wave packet can be coherently split, redirected, and recombined, leading to interference at the final beam splitting pulse (Figure 4.18). Afterwards, the population of the interferometer output ports is read out using state-selective fluorescence detection in the upper detection zone (see Section 4.2 & Section 3.3). A full experimental cycle takes $\approx 1.6 \text{ s}$, limited by the 3D MOT loading time.

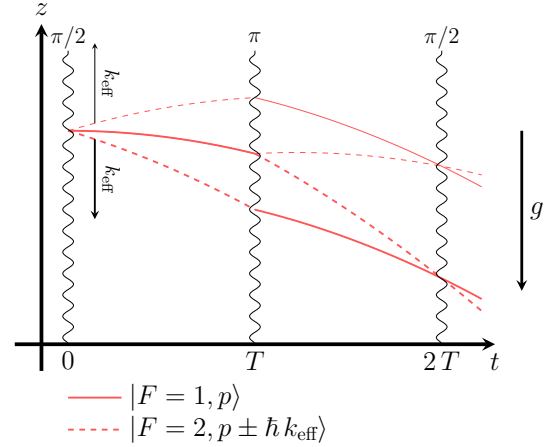


Fig. 4.18: Space-time diagram of a MACH-ZEHNDER matter wave interferometer in a constant gravitational field for the downward (thick lines) and upward (thin lines) direction of momentum transfer. Stimulated RAMAN transitions at times 0, T , and $2T$ couple the states $|F = 1, p\rangle$ and $|F = 2, p \pm \hbar k_{\text{eff}}\rangle$. The velocity change induced by the RAMAN pulses is not to scale with respect to the gravitational acceleration.

4.4.2 Suppression of phase shifts using the k -reversal method

In the presence of external perturbations, additional contributions enter the interferometer phase shift besides the gravitationally induced phase shift $\Delta\phi$. As indicated in Figure 4.18 and explained in Section 4.3.1, the direction of momentum transfer of a RAMAN transition, upward or downward, can be chosen by adequately tuning the difference frequency of the two light fields onto the corresponding two-photon resonance. Classifying additional phase shift contributions into components that are dependent or independent of the direction of momentum transfer, the total interferometer phase shift is

$$\Delta\phi_{\text{tot}}^{(+)} = \Delta\phi + \Delta\phi_{\text{ind}} + \Delta\phi_{\text{dep}}, \quad (4.24)$$

$$\Delta\phi_{\text{tot}}^{(-)} = -\Delta\phi + \Delta\phi_{\text{ind}} - \Delta\phi_{\text{dep}}, \quad (4.25)$$

where the superscript (\pm) marks the phase shift for the downward $k^{(-)}$ and upward $k^{(+)}$ directions of momentum transfer¹. In consequence, obtaining the total phase shifts $\Delta\phi_{\text{tot}}^{(\pm)}$ with different directions of momentum transfer (“ k -reversal”) allows to compute the half difference phase

$$\Delta\phi_{\text{tot}} \equiv \frac{\Delta\phi_{\text{tot}}^{(+)} - \Delta\phi_{\text{tot}}^{(-)}}{2} = \Delta\phi + \Delta\phi_{\text{dep}}, \quad (4.26)$$

in which all phase shifts $\Delta\phi_{\text{ind}}$ independent of the sign of k_{eff} are canceled [127, 138]. Common examples for phase shifts that are independent of the direction of k_{eff} are the quadratic ZEEMAN shift² and the one-photon AC-STARK shift. Bias contributions that are dependent on the direction of momentum transfer are, e.g., shifts due to wavefront distortions, the CORIOLIS force, and the two-photon light shift³. As the k -reversal method requires at least two single shots, biases can only effectively be rejected if the bias contribution that shall be canceled is constant, or changing sufficiently slowly over the duration of acquiring one data point pair. The strong suppression of bias effects is demonstrated in Figure 4.19. The displayed measurements of acceleration in Figure 4.19 a) are obtained by subsequently acquiring 10 data points per direction of momentum transfer ($\Delta a^{(+)}$ & $\Delta a^{(-)}$) while scanning the interferometer phase across a full fringe. Tracking the position of the fringe minimum then allows to determine the change in acceleration. The signals for the upward and downward direction of momentum transfer are subject to both, an oscillation and a time-independent bias, which can for example be caused by time-dependent magnetic field changes or AC-STARK shifts induced by fluctuating RAMAN

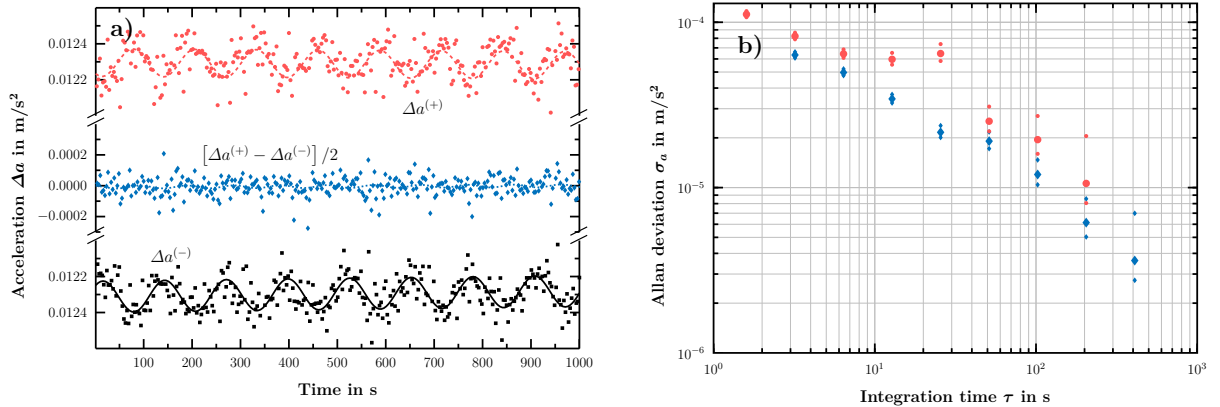


Figure 4.19: a) Measurements of local acceleration $\Delta a^{(-)}$ for the downward (black squares and solid black line) and $\Delta a^{(+)}$ for the upward direction (red circles and dashed red line) of momentum transfer obtained by repetitively scanning across a full fringe with alternating direction of momentum transfer, and the half difference signal $[\Delta a^{(+)} - \Delta a^{(-)}]/2$ (blue diamonds and dotted blue line). Sinusoidal functions with a linear offset drift have been fitted to better stress the periodic behavior the signals are subject to. b) ALLAN deviations of $\Delta a^{(-)}$ (red circles) and $[\Delta a^{(+)} - \Delta a^{(-)}]/2$ (blue diamonds).

- 1 Throughout this Chapter, $-\Delta\phi^{(-)}$ is plotted for the downward direction of momentum transfer in order to yield a positive value $g > 0$.
- 2 The k -reversal method does not allow to cancel shifts induced by magnetic field gradients (see Section 5.2).
- 3 Based on the linear scaling of the two-photon light shift with the RABI frequency, utilizing a measurement protocol using a linear combination of a data point taken at full RABI frequency Ω_{eff} and a point at half frequency $\Omega_{\text{eff}}/2$ allows to extrapolate the shift to zero at the cost of a $\sqrt{10}$ larger instability [127].

beam powers. Calculating their half difference signal allows to reject these disturbances. This is emphasized in Figure 4.19 b), where the ALLAN deviations of $k^{(-)}$ -signal and the half difference signal are plotted. In this example, short-term fluctuations as well as slower drifts are suppressed by a factor of 2 or more on average and long-term drifts over the whole data set are rejected by a factor of ≈ 3 . Specifically when using potassium, which typically is subject to larger systematic shifts than, e.g. rubidium (see Section 5.2), the k -reversal method is of great value. For example, due to its smaller hyperfine energy splitting, ^{39}K is subject to a second-order ZEEMAN effect that is larger by a factor of 15 as compared to rubidium.

4.4.3 Data analysis

The leading order phase shift of a MACH-ZEHNDER interferometer as depicted in Figure 4.18 is (Equation (2.23))

$$\Delta\phi = \left(g - \frac{\alpha}{k_{\text{eff}}}\right) \cdot k_{\text{eff}} \cdot T^2$$

under the consideration of a constant frequency change rate α of the RAMAN laser difference frequency as shown in Section 2.1. Here, linearly changing the RAMAN difference frequency gives rise to an effective acceleration of the RAMAN wavefronts (Equation (2.22))

$$a \equiv \alpha/k_{\text{eff}}$$

and thus allows to null the gravitationally induced phase shift for $\alpha(g)/k_{\text{eff}} = \alpha_D/k_{\text{eff}} = g$. Vice versa, at this chirp rate $\alpha(g)$ the interferometer phase is independent of the pulse separation time T . By carefully changing α , the interferometer phase can be carefully controlled and typical fringe patterns can be observed.

Figure 4.21 shows a typical determination of the local gravitational acceleration g under the use of the k -reversal measurement protocol. Typical fringes are acquired using the experimental sequence described above using no additional state preparation. Operating the interferometer for pulse separation times $T = 18, 20, 22$ ms for the upward and downward direction of momentum transfer, two central fringe positions for effective accelerations $a^{(\pm)}(g)$ of the RAMAN wavefronts

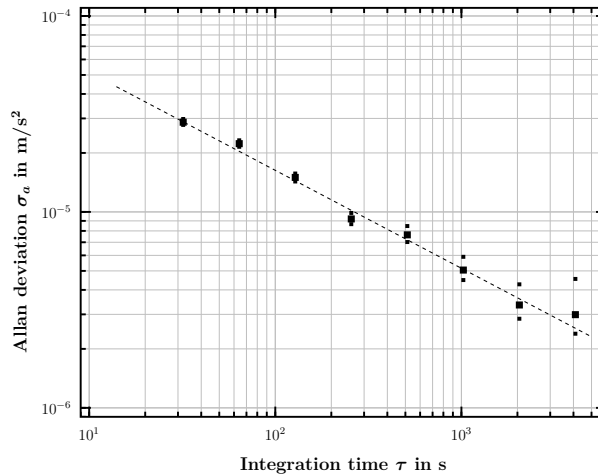


Figure 4.20: Allan deviation of a potassium long-term measurement of local gravitational acceleration.

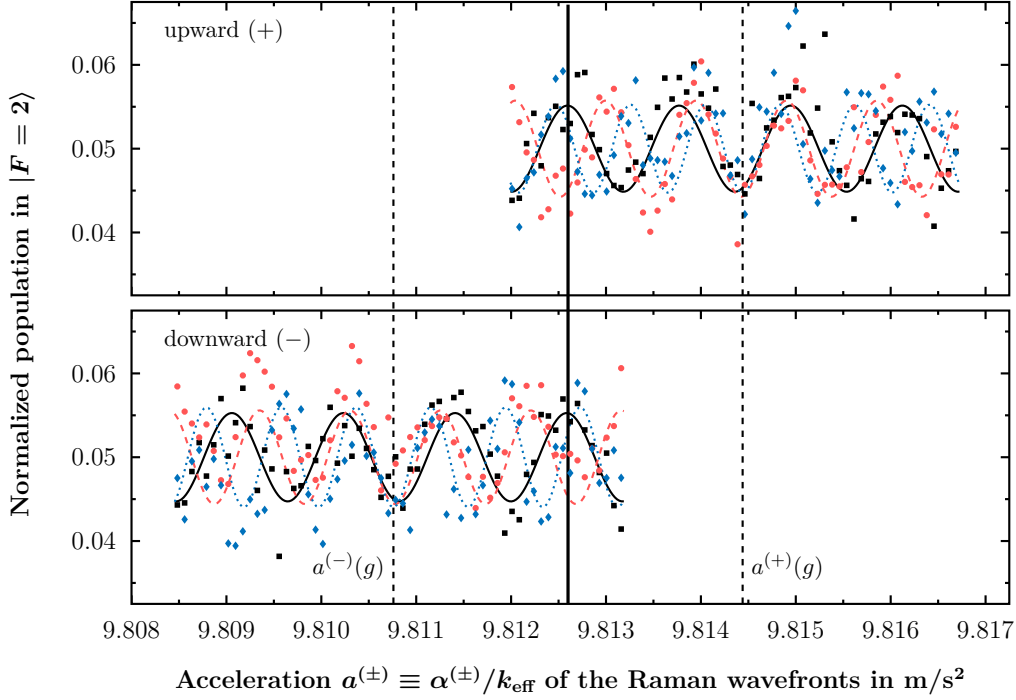


Figure 4.21: Determination of gravitational acceleration with potassium. Typical fringe signals and sinusoidal fit functions are plotted in dependence of the effective RAMAN wavefront acceleration for pulse separation times $T = 18$ ms (black squares and solid black line), $T = 20$ ms (red circles and dashed red line), and $T = 22$ ms (blue diamonds and dotted blue line) for upward (+) and downward (-) direction of momentum transfer. The central fringe positions $\mathbf{a}^{(\pm)}(\mathbf{g})$ (dashed vertical lines) are shifted symmetrically around $g = [a^{(+)}(g) - a^{(-)}(g)]/2$ (solid vertical line). The data sets are corrected for slow linear drifts and offsets.

manifest for which the interferometer phase is independent of the pulse separation time. These accelerations are shifted symmetrically around the local gravitational acceleration g including bias contributions that are dependent on the sign of k_{eff} . The systematic shift moving $a^{(\pm)}(g)$ away from g can mainly be attributed to the second-order ZEEMAN shift¹. After identification of the central fringe positions, these accelerations are continuously monitored by tuning the effective acceleration α/k_{eff} across $a^{(\pm)}(g)$ in 10 steps for both signs of k_{eff} in alternating order at fixed pulse separation time $T = 22$ ms. Subsequently, the resulting phases $\Delta\phi^{(\pm)}$ are used to calculate the half difference signal yielding the gravitational acceleration g . In Figure 4.20, the ALLAN deviation of the resulting time series is computed. After $\tau = 4096$ s integration, a minimum instability of $\sigma_a = 3 \times 10^{-6}$ m/s² is achieved. Taking the systematics assessment in Section 5.2 into account, it can be seen that the systematic uncertainty of this measurement lies well below the achieved statistical resolution. Averaging over the time series, the local gravitational acceleration $g = 9.81260 \pm 3.0 \times 10^{-6}$ m/s² is calculated.

¹ A more detailed assessment of systematics shifts in the context of the performed dual species measurement is described in Section 5.2.

4.5 Discussion

In this Section, recent data inferring improvements of the short-term stability by more than one order of magnitude is shown. Finally, an overview on fundamental challenges, giving rise to technical consequences for a matter wave interferometer based on potassium, is provided.

Recent improvements

An increase of the short-term stability of the potassium interferometer by about one order of magnitude were recently achieved. Two changes mainly contributed to this improvement. Replacing the voltage-controlled oscillator generating the mixing frequency of the overall RAMAN detuning $\Delta \approx 2\pi \cdot 3.3$ GHz (see Section 3.2.3) with a frequency-doubled synthesizer oscillating at $2\pi \cdot 1.7$ GHz increased the frequency stability of the RAMAN master laser. Previously, the frequency instability induced by the voltage-controlled oscillator was found to have a disadvantageous effect on the slave laser phase lock. Figure 4.22 shows a comparison of the $\pi/2$ -pulse beam splitting instability σ_P before and after replacing the voltage-controlled oscillator and yields an improvement by a factor of > 3 . Furthermore, the use of a velocity selection sequence (see Section 4.3.3) significantly increased the maximum achievable contrast, thus reducing the influence of noise caused by spontaneous emission and by the detection. With the described improvements, it was possible to obtain inertial-sensitive fringes (Figure 4.23) with pulse separation times $T = 25$ ms with a contrast $C \approx 6\%$, and even $T = 50$ ms with a contrast $C \approx 2\%$. This data constitutes an improvement over the data shown above of about one order of magnitude and gives rise to very promising extrapolations for future tests of the universality of free fall (see Chapter 6).

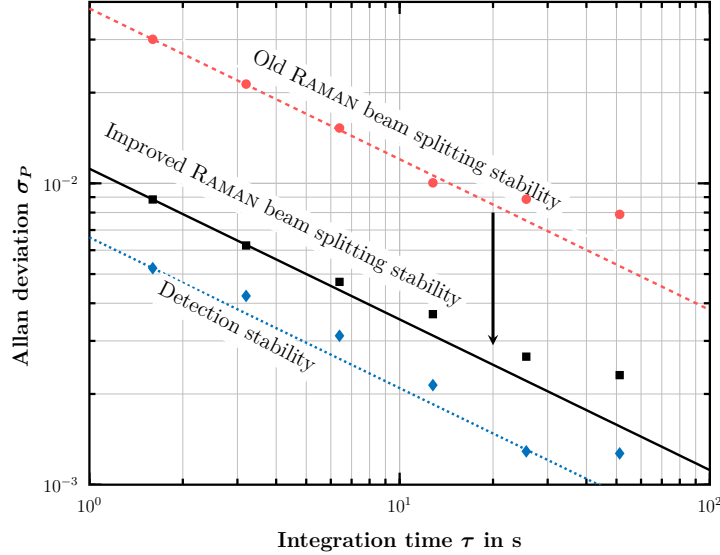


Figure 4.22: ALLAN deviations of the RAMAN beam splitting stability before (red circles and red dashed line) and after (black squares and solid black line) replacing the voltage-controlled oscillator generating the mixing frequency realizing the RAMAN detuning $\Delta \approx 2\pi \cdot 3.3$ GHz. The data is obtained by acquiring a series of $\pi/2$ -pulses. An improvement by a factor of ≈ 3 is achieved. For comparison the detection stability is plotted (blue diamonds and dotted blue line).

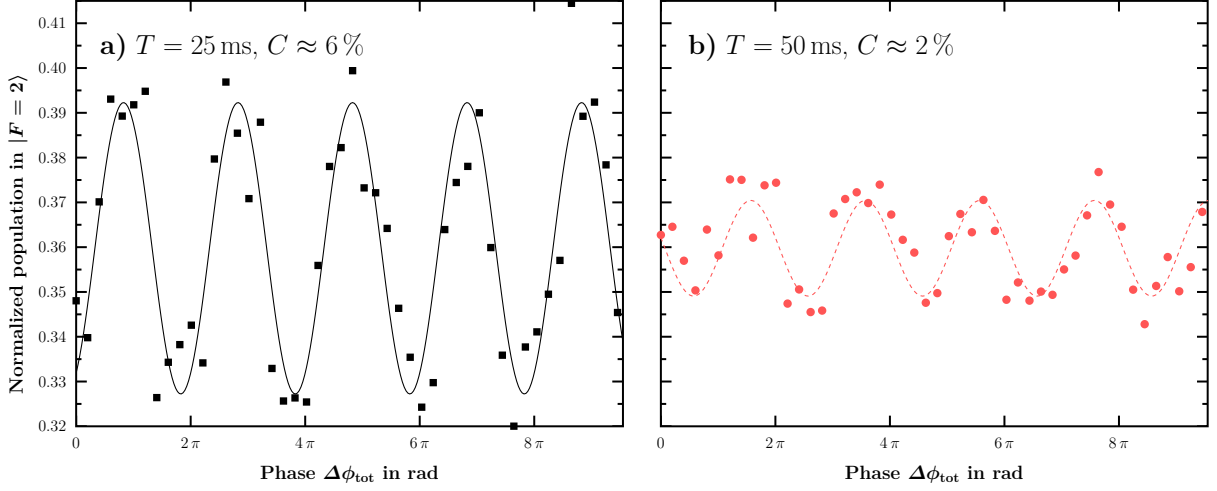


Figure 4.23: Inertial-sensitive potassium fringes with pulse separation times $T = 25$ ms, $C \approx 6\%$, and $T = 50$ ms, $C \approx 2\%$. The offset of the data obtained at $T = 50$ ms is adjusted.

Fundamental potassium challenges

The choice of potassium as a test mass in a matter wave interferometer is mainly driven by the application in a dual species UFF test in combination with rubidium. On the one hand, potassium benefits strongly from previously demonstrated applications of rubidium-potassium mixtures, the proximity of its D_2 line to the one of rubidium, and the good mass ratio. On the other hand, however, operating a matter wave interferometer with potassium imposes various technical challenges, that find their origin in the fundamental properties of potassium:

1. Ensemble expansion

Potassium does not provide the closed transitions essential for efficient free space cooling. The achievable temperatures with straightforward approaches are limited to the $20\ \mu\text{K}$ regime [119]. Even more sophisticated schemes yield temperatures that lie a factor of 2-3 above typical sub-DOPPLER temperatures accessible with rubidium [129]. In combination with its lighter mass, potassium is subject substantially higher expansion rates even in the case of lowest free space cooling temperatures (see Section 4.3.4).

2. Fluorescence detection

Due to the narrow excited state hyperfine splitting, fluorescence detection of potassium is subject to increased losses into the dark $|F = 1\rangle$ state. Besides the signal-to-noise ratio suffering from this fact, as shown in Section 4.2, detection frequency noise leads to errors in the normalized signal. As the excited state splitting is smaller than for ^{39}K , these issues are even more significant when using ^{41}K . Furthermore, after free fall on the order of a few hundred milliseconds, the low densities make absorption imaging practically impossible without further cooling.

3. Systematic effects

With its low hyperfine splitting, ^{39}K is inherently subject to a second-order ZEEMAN shift that is about a factor of 15 larger than the one for rubidium (see Equation (5.2)). Without matching the effective wave vectors $k_{\text{eff,K}}$ and $k_{\text{eff,Rb}}$, the ensembles propagate on different trajectories mainly due to the factor of ≈ 2 difference in mass. Magnetic field gradients that impose phase shifts cannot be compensated for by the k -reversal method and require precise

analysis of the magnetic field. The analysis in Section 4.3.2 showed that for sufficiently large detunings, the one-photon light shift induced by the RAMAN lasers cannot be compensated for in the case of potassium. While the k -reversal scheme (see Section 4.4.2) allows to reject any constant AC-STARK shifts, high frequency RAMAN laser power fluctuations will not be canceled and increase the technical noise level of the interferometer (see sec:acstarkK).

The described challenges lead to technical consequences, such as the higher potassium RAMAN laser power (≈ 100 mW per frequency) as compared to rubidium, in order to cope with the higher temperatures and get a reasonable excitation probability. Moreover, in the case of rubidium, the influence of AC-STARK shifts can be strongly reduced by setting the correct intensity ratio of the two RAMAN laser frequencies. Next to reducing the constant bias, this also reduces the effect of short-term fluctuations of the laser power. As highlighted in Chapter 6, ultimately the use of a common optical dipole trap will ease up the issues related to the expansion of potassium. At the same time, such a trap will help to constrain various systematic effects.

The demonstration of the first potassium gravimeter yielded $g = 9.81260 \pm 3.0 \times 10^{-6} \text{ m/s}^2$. While this performance is yet far away from state-of-the-art gravimeters based on matter wave interferometry with rubidium and cesium, the results presented in this Chapter form a solid foundation for the first quantum test of the universality of free fall using two species as described in the following Chapter.

CHAPTER 5

Testing the Universality of Free Fall with rubidium and potassium

In this Chapter, the first quantum test of the universality of free fall using two species, rubidium and potassium [51], is described in detail. In Section 5.1, the experimental methods are described using the tools explained in Chapter 4. Further on, Section 5.1.1 explains the data analysis. A thorough review on the systematic effects affecting the measurement is provided in Section 5.2, and the Chapter closes with a short discussion of the results in Section 5.3.

5.1 Experimental methods

Performing a dual species measurement implies certain constraints on the experimental sequence, as different requirements of the two test species have to be fulfilled. Compared to rubidium, the operation of a potassium matter wave interferometer is more demanding, mostly due to the lighter mass, and higher temperatures that can be achieved with free space cooling. Moreover, a typically lower potassium atom number makes an optimization of the apparatus for better potassium loading rates and cooling necessary in order to match the performance as compared to rubidium. Hence, in contrast to a single species interferometer the compatibility of laser cooling methods has to be assured and trade-offs have to be accepted concerning timing of the sequence, e.g. regarding switching of magnetic fields, the duration of a cooling phase, or optical pumping.

The experimental sequence for testing the universality of free fall with rubidium and potassium is composed as follows. Within a loading time of 1 s, 8×10^8 atoms of ^{87}Rb and 3×10^7 atoms of ^{39}K are collected in the 3D MOT. Afterwards, the ensembles are cooled down to sub-DOPPLER temperatures. For potassium, this is accomplished utilizing the techniques described in Section 4.1, and optimized beam balancing in favor of potassium cooling. For rubidium, standard methods are employed [62, 63]. In comparison to the optimum rubidium

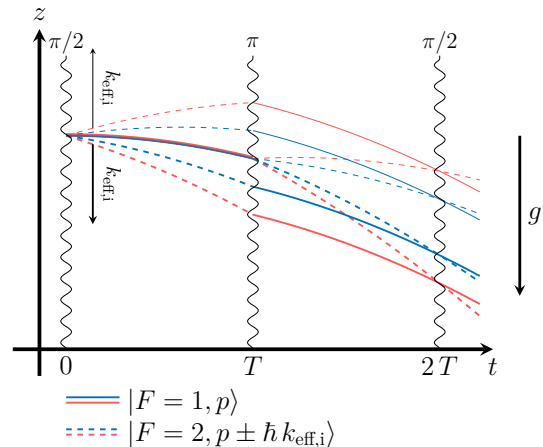


Fig. 5.1: Space-time diagram of a dual-species MACH-ZEHNDER matter wave interferometer in a constant gravitational field for the downward (thick lines) and upward (thin lines) direction of momentum transfer. Stimulated RAMAN transitions at times 0, T , and $2T$ couple the states $|F_i = 1, p\rangle$ and $|F_i = 2, p \pm \hbar k_{\text{eff},i}\rangle$, where i stands for Rb (blue lines) or K (red lines). The velocity change induced by the RAMAN pulses is not to scale with respect to the gravitational acceleration.

cooling parameters [90], the timing of the rubidium cooling is adapted in favor of the potassium sequence. The sub-DOPPLER cooling phase yields temperatures $T_{\text{Rb}} = 27 \mu\text{K}$ and $T_{\text{K}} = 32 \mu\text{K}$ after a duration of 15 ms, and is followed by a 1.5 ms long optical pumping phase. In this stage, both the rubidium and potassium repumping lasers are switched off to transfer all atoms into the $|F_i = 1\rangle$ manifold (throughout this Chapter, i is Rb or K). By switching off all cooling light fields, the atoms are subsequently released into free fall.

Stimulated RAMAN transitions are utilized to coherently couple the states $|F_i = 1, p\rangle$ and $|F_i = 2, p \pm \hbar k_{\text{eff},i}\rangle$, where $m_{F,i} = 0$. At a RAMAN detuning of $\Delta_{\text{K}} = 3.3 \text{ GHz}$, the typical π -pulse width for potassium is $\tau_{\pi} = 15 \mu\text{s}$. For rubidium, the detuning $\Delta_{\text{Rb}} = 1.6 \text{ GHz}$, and an identical pulse width is chosen. After a free fall time of $t_{\text{TOF}} = 43 \text{ ms}$ (see Section 4.3.3), a MACH-ZEHNDER interferometry sequence (see Section 4.4) is driven as indicated in Figure 5.1 with a common pulse separation time T while applying a constant frequency change rate α on the RAMAN difference frequency. No additional input state preparation measures are performed. Afterwards, normalized detection signals are obtained by state-selective fluorescence detection in the upper detection zone (see Section 3.3 & Section 4.2). In total, an experimental cycle takes $\approx 1.6 \text{ s}$, mainly limited by the 3D MOT loading time.

In direct analogy to Section 4.4.2, the gravitationally induced phase shift for the two species (Equation (2.23))

$$\Delta\phi_i = \left(g_i - \frac{\alpha_i}{k_{\text{eff},i}}\right) \cdot k_{\text{eff},i} \cdot T^2$$

is determined by identifying the central fringe positions $a_i^{(\pm)}(g)$ for the upward (+) and downward (-) direction of momentum transfer, at which the interferometer phase is independent of the pulse separation time T . For this purpose, the interferometers are operated at $T = 8, 15, 20 \text{ ms}$ and their phase is scanned around $a_i^{(\pm)}(g)$ in Figure 5.2¹. The central fringe determination is performed simultaneously for rubidium and potassium in order to account for any common biases or inter-species systematic contributions, such as the light shift that is imposed by the RAMAN laser light of one species to the other. Systematic bias contributions (see Section 5.2) independent of the direction of momentum transfer shift the positions $a_i^{(\pm)}(g)$ symmetrically around the unshifted position. Moreover, in the case of potassium, bias contributions, that are dependent of the pulse separation time T , for example caused by the second-order ZEEMAN effect and the AC-STARK shift, can introduce an effective shift² of the acceleration $a_i^{(\pm)}(g)$. However, as the shifts do not depend on the sign of k_{eff} , they are suppressed by the k -reversal scheme regardless if they can be analyzed in detail, as long as a central fringe position $a_i^{(\pm)}(g)$ can be identified symmetrically around the unshifted position.

5.1.1 Data analysis

For testing the universality of free fall, the central fringe positions $a_i^{(\pm)}(g)$ are monitored continuously over $\approx 4 \text{ h}$. For this purpose, the effective acceleration of the RAMAN wavefronts

1 Throughout this Chapter, $-\Delta\phi_i^{(-)}$ is plotted for the downward direction of momentum transfer in order to yield a positive value $g_i > 0$.

2 Differential bias contributions in dependence of the pulse separation time T can shift fringe minima out of phase at the “real” position $a_i^{(\pm)}(g)$ and cause the signals to rephase at an effective larger shift.

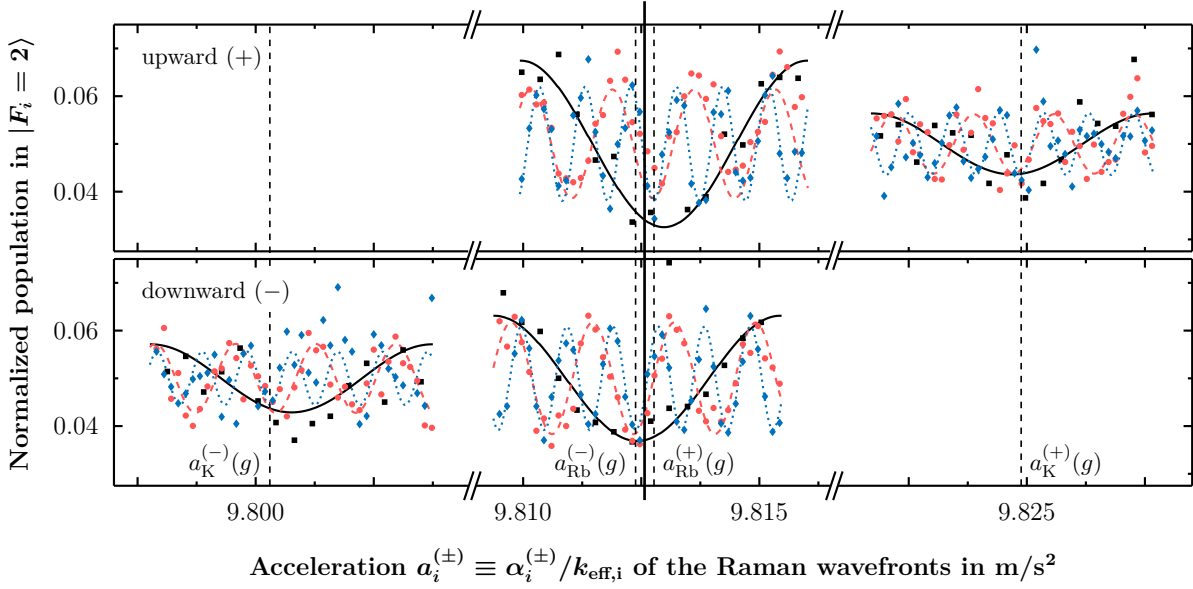


Figure 5.2: Determination of the differential gravitational acceleration of rubidium and potassium. Typical fringe signals and sinusoidal fit functions are plotted in dependence of the effective RAMAN wavefront acceleration for pulse separation times $T = 8$ ms (black squares and solid black line), $T = 15$ ms (red circles and dashed red line), and $T = 20$ ms (blue diamonds and dotted blue line) for upward (+) and downward (-) direction of momentum transfer. The central fringe positions $\mathbf{a}_i^{(\pm)}(\mathbf{g})$ (dashed vertical lines), where i is Rb or K, are shifted symmetrically around $g_i = [a_i^{(+)}(g) - a_i^{(-)}(g)]/2$ (solid vertical line). The data sets are corrected for slow linear drifts and offsets.

$\alpha_i^{(\pm)}/k_{\text{eff},i}$ is tuned around $a_i^{(\pm)}(g)$ in 10 steps per direction of momentum transfer¹ simultaneously for rubidium and potassium with a pulse separation time of $T = 20$ ms. Accordingly, the acquisition of $g_i = [a_i^{(+)}(g) - a_i^{(-)}(g)]/2$ takes 32 s in total and yields one data point for the EÖTVÖS ratio (Equation (1.2)). The statistical error of the EÖTVÖS ratio measurement, and of the single species interferometers is analyzed in the ALLAN deviation in Figure 5.3. After 4096 s of integration, the statistical uncertainty of the EÖTVÖS ratio determination is $\sigma_\eta = 5.4 \times 10^{-7}$. The contrast of the rubidium interferometer suffers from the matched pulse width, which is optimized for potassium. Taking into account the performance of the single species measurements it can be seen that the statistical uncertainty of the potassium interferometer is dominating the integration of the EÖTVÖS ratio signal. The rubidium interferometer, although affected by a drift caused by the detection, is about a factor 5 more stable than the potassium measurement. The contrast of the potassium interferometer is mainly limited by the high ensemble temperature, as no state preparation methods are applied. The obtained fringe oscillations are furthermore affected by non-inertial technical noise², as fluctuations of the RAMAN laser power and instabilities of the master and slave laser phase locks cause excitation variations of the beam splitting process (Section 4.5). Accordingly, as the dominant noise source affecting the rubidium and potassium measurement, no common mode suppression [49, 139, 140] can be observed.

1 A data acquisition at the mid-fringe position (see Section 2.1.2) was inhibited by the limited stability of the measurement contrast.

2 Phase noise induced by the AC-STARK shift due to RAMAN power fluctuations is only expected to affect the measurement at a single shot resolution on a 10 parts per billion level (see Section 4.3.2).

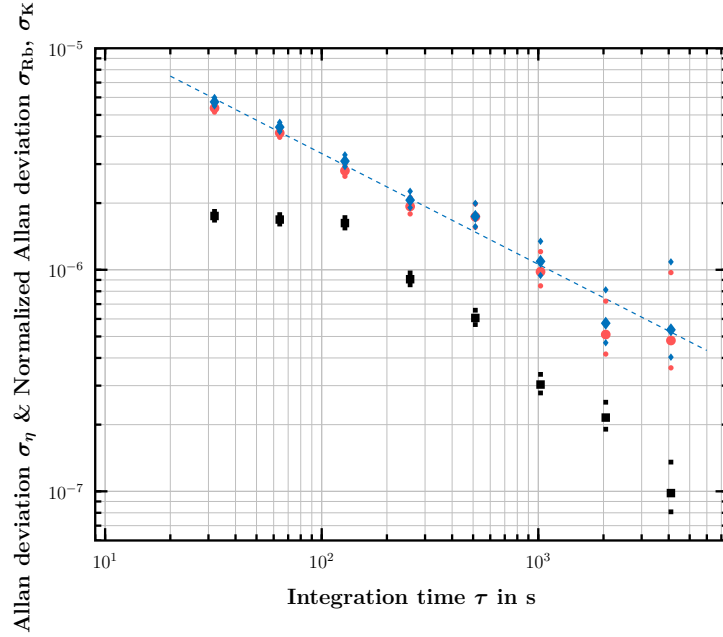


Figure 5.3: ALLAN deviation σ_η of the EÖTVÖS ratio $\eta_{\text{Rb,K}}$ (blue diamonds) and its asymptotic behavior (dashed blue line) in dependence on the integration time τ . After 4096 s of integration, the statistical uncertainty of the EÖTVÖS ratio is $\sigma_\eta = 5.4 \times 10^{-7}$. The measurement is solely limited by the stability of the potassium signal as can be seen from the ALLAN deviations of the rubidium signal g_{Rb} (black squares) and the potassium signal g_{K} (red circles), which are normalized to their mean acceleration.

5.2 Analysis of systematic effects

Before extracting a result for the EÖTVÖS ratio $\eta_{\text{Rb,K}}$, a variety of bias contributions $\Delta\eta$ and their related uncertainties $\delta\eta$ affecting the determination of the EÖTVÖS ratio have to be taken into account. Given the phase shifts ϕ_i , the EÖTVÖS ratio (Equation (1.2)) can be written as

$$\eta_{\text{Rb,K}} = 2 \frac{k_{\text{eff,K}} \phi_{\text{Rb}} - k_{\text{eff,Rb}} \phi_{\text{K}}}{k_{\text{eff,K}} \phi_{\text{Rb}} + k_{\text{eff,Rb}} \phi_{\text{K}}} = 2 \frac{\frac{k_{\text{eff,K}}}{k_{\text{eff,Rb}}} \phi_{\text{Rb}} - \phi_{\text{K}}}{\frac{k_{\text{eff,K}}}{k_{\text{eff,Rb}}} \phi_{\text{Rb}} + \phi_{\text{K}}}. \quad (5.1)$$

Accordingly, knowledge of differential phase biases and uncertainties due to systematic effects can be expressed in terms of the EÖTVÖS ratio. In Sections 5.2.1 – 5.2.6, the dominant perturbations influencing the measurement are discussed with respect to their origin, and analyzed quantitatively using the experimental parameters listed in Table C.1. The effects are treated to the lowest order unless stated otherwise.

5.2.1 One-photon light shift

The AC-STARK shift can be suppressed to a level with no relevance for the presented test of the universality of free fall by utilizing the k -reversal scheme. As choosing an adequate power ratio of the two RAMAN frequencies allows to null the one-photon AC-STARK shift of rubidium, a calculation according to Section 4.3.2 yields a current bias level of $\approx 6.23 \times 10^{-12} g$. Furthermore, the inter-species AC-STARK shifts imposed by the RAMAN beam splitting light field of one species onto the other one are *per se* suppressed by 3 orders of magnitude since

they are subject to a detuning in the terahertz regime corresponding to the difference in wavelength $\Delta\lambda \approx (780 - 767) \text{ nm}$, and the leading contribution affecting an EÖTVÖS ratio measurement remains the light shift perturbing the potassium interferometer. A calculation following Section 4.3.2 allows to infer a suppression of the AC-STARK bias by 4 orders of magnitude to a level of $\approx 1.35 \times 10^{-10} g$, limited by a linear power drift examined in a long-term power measurement. For example, acquiring single data points for the two directions of momentum transfer in alternating order ($k^{(+)} - k^{(-)} - k^{(+)} \dots$) instead of switching the sign of k_{eff} after 10 shots ($10 \times k^{(+)} - 10 \times k^{(-)} - 10 \times k^{(+)} \dots$) reduces this limit by one order of magnitude. Furthermore, a slightly more complex scheme ($k^{(+)} - k^{(-)} - k^{(-)} - k^{(+)} - k^{(+)} \dots$) allows to fully suppress linear drifts and constrains residual biases to higher order contributions.

5.2.2 Zeeman effect

As both interferometers are exclusively operated in states with $m_{F,i} = 0$, the linear ZEEMAN shift vanishes and thus imposes no phase contribution onto the EÖTVÖS ratio measurement. The second-order ZEEMAN shift (“clock shift”) between the hyperfine ground state $m_F = 0$ states in a small magnetic field B [141]

$$\Delta\omega_{\text{clock}} = \frac{(g_J - g_I)^2 \mu_B^2}{2\hbar^2 \omega_{12}} B^2, \quad (5.2)$$

with the LANDÉ g -factors g_J and g_I , and hyperfine transition frequency ω_{12} , however, induces a frequency shift of the unperturbed hyperfine transitions of potassium and rubidium. When analyzing the residual bias for the EÖTVÖS ratio determination, a distinct delineation between spatial and temporal changes of the magnetic field has to be made. Following the sensitivity formalism (see 2.1), any shifts induced by temporal changes $B(t)$ at the center of mass position in the magnetic field that do not cancel due to symmetry over the duration of the interferometer, cause an acceleration bias. This bias, which lies on the order of $1 \times 10^{-4} g$ for potassium in the present experiment, is strongly suppressed in the k -reversal scheme (see Section 4.4.2) as it imposes a phase shift independent of the direction of momentum transfer. In contrast, spatial changes of the magnetic field will lead to a frequency shift dependent on the *specific trajectory* of the center of mass (Figure 5.1), and thus the experienced recoil due to the interaction with the beam splitter. As a result, after applying the k -reversal scheme, a non vanishing dependency on v_{rec} and the magnetic field susceptibility remains, which can be analyzed to first order using the local magnetic field gradient $\partial B(t)/\partial z$. The frequency shift induced by the splitting of the two interferometer arms is

$$\Delta\omega_{\text{rec}(\pm),i}(t) \equiv \pm \frac{\Delta\omega_{\text{clock},i}}{B^2} \cdot \frac{\partial B(t)}{\partial z} \cdot B(t) \cdot v_{\text{rec},i} t, \quad (5.3)$$

with the clock shift $\Delta\omega_{\text{clock},i}$ (Equation (5.2)) and recoil velocity $v_{\text{rec},i}$ (Equation (2.12)) for the upward and downward direction of momentum transfer. Computing the convolution with the sensitivity function

$$\Delta\Phi_i^{\text{rec}} \equiv \int_{-\infty}^{\infty} g_{s,\text{MZ}}(t) \Delta\omega_{\text{rec},i}(t) dt \quad (5.4)$$

with the sensitivity function $g_{s,\text{MZ}}(t)$ (Equation (2.24)), allows to determine the phase shift imposed onto species i by a residual magnetic field gradient.

Figure 5.4 a) shows the magnetic field gradient, which was determined by means of microwave spectroscopy of the $|F = 1, m_F = 0\rangle \rightarrow |F = 2, m_F = 0\rangle$ and $|F = 1, m_F = -1\rangle \rightarrow |F = 2, m_F = -1\rangle$ transitions in rubidium. In combination with the measured field $B(t)$ (Figure 5.4 b)), using Equation (5.4) allows to calculate the differential bias acceleration affecting the measurement of the EÖTVÖS ratio. With $\Delta\omega_{\text{clock,Rb}}/B^2 = 2\pi \cdot 575.15 \text{ Hz/G}^2$ for rubidium and $\Delta\omega_{\text{clock,K}}/B^2 = 2\pi \cdot 8.526 \text{ kHz/G}^2$ for potassium, the differential acceleration is $\Delta\eta^{\text{rec}} = (-5.8 \pm 2.6) \times 10^{-8}$, with the error inferred from the magnetic gradient fit function using uncertainty propagation. The uncertainty can be further reduced by surveying the magnetic gradient with higher resolution. Furthermore, the switching of $B(t)$ was recently improved, yielding a steady state after a shorter time.

5.2.3 Effective wave vector

Precise knowledge of $k_{\text{eff},i}$ is necessary to achieve high accuracy in the determination of g . Both, uncertainties of $k_{\text{eff},i}$, e.g. due to limited accuracy of a spectroscopy lock, and changes of the projection $\vec{k}_{\text{eff}} \cdot \vec{g}$, such as misalignment of the retroreflected beam splitting light field, or wavefront aberrations, have to be taken into account for the error estimation.

Spectroscopy uncertainty

The D_2 lines of rubidium and potassium are determined to relative uncertainties of 1×10^{-11} [142], and 2×10^{-10} [122], respectively. Assuming uncertainties of the potassium and rubidium spectroscopies $\Delta\omega_i$, the uncertainty in the EÖTVÖS ratio to leading order in $\Delta\omega_i$ is

$$\delta\eta^{\text{spec}} = \sqrt{\left(\frac{\Delta\omega_{\text{Rb}}}{2\omega_{D_2,\text{Rb}}}\right)^2 + \left(\frac{\Delta\omega_{\text{K}}}{2\omega_{D_2,\text{K}}}\right)^2}, \quad (5.5)$$

with the D_2 line transition frequency $f_{D_2,i}$. With the assumption $\Delta\omega_{\text{Rb}} = \Delta\omega_{\text{K}} = 700 \text{ kHz}$, the uncertainty of the EÖTVÖS ratio becomes $\delta\eta^{\text{spec}} = 1.3 \times 10^{-9}$.

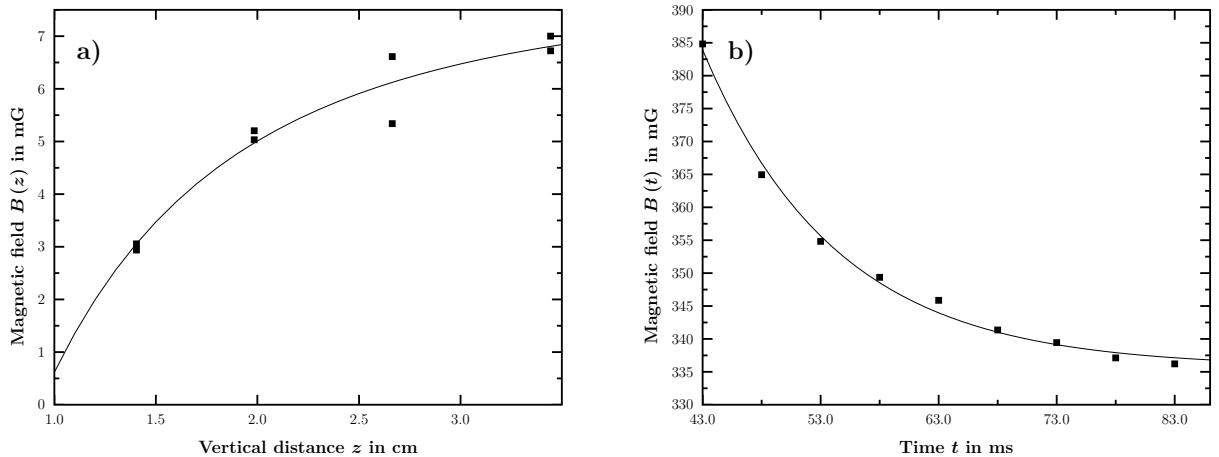


Figure 5.4: a) Purely spatial magnetic field variation in dependence of the falling distance starting from the 3D MOT position (black squares) and fitted function $B(z) \propto a/(z+b)^3$ (solid black line). In a normal experimental sequence, the gradient is masked by stronger temporal variations. b) Switching behavior of the magnetic field coils (black squares) and fitted function $B(t) \propto a \cdot \exp[-bt]$ (solid black line) starting at the time of the first interferometer pulse $t_{\text{TOF}} = 43 \text{ ms}$.

Vertical alignment

Alignment errors of the RAMAN beam splitting light fields change the projection $\vec{k}_{\text{eff}} \cdot \vec{g}$ and thus the gravitationally induced phase shift. To quadratic order, the relative phase shift caused by a small angle misalignment $\delta\alpha$ of \vec{k}_{eff} away from the vertical axis is

$$\frac{\Delta\phi_i^{\text{al}}}{\phi_i} = \frac{\delta\alpha_i^2}{2}. \quad (5.6)$$

In the present experiment, the vertical alignment uncertainty $\delta\alpha = \delta\alpha_{\text{Rb}} = \delta\alpha_{\text{K}} = 0.03 \text{ mrad}$ is common to both the rubidium and potassium RAMAN light fields. The resulting uncertainty of the EÖTVÖS ratio measurement is thus strongly suppressed:

$$\delta\eta^{\text{al}} = \frac{\delta\alpha^2}{2} \left(1 - \frac{k_{\text{eff,K}}}{k_{\text{eff,Rb}}} \right). \quad (5.7)$$

The uncertainty of the EÖTVÖS ratio yields $\delta\eta^{\text{al}} = 7.9 \times 10^{-12}$ and is negligible for the given experimental parameters.

Wavefront aberration

Treating the two-photon light field as a plane wave is not sufficient when analyzing bias contributions in an interferometer. Given the finite size of an atomic ensemble in an interferometer, and spatial variations of the RAMAN light field, e.g. due to wavefront curvature, changes in the projection $\vec{k}_{\text{eff}} \cdot \vec{g}$ as indicated in Figure 5.5 occur. This in turn can cause different average effective wave vectors k_{eff} throughout the interferometer and result in a bias acceleration. Due to the retroreflected setup, wavefront imperfections are strongly suppressed. For example, the wavefront curvature R_{in} of the incident wave is greatly compensated for by roughly the opposite curvature R_{re} of the retroreflected beam¹, yielding a much larger effective curvature (Figure 5.5). In a MACH-ZEHNDER interferometer, the acceleration bias for a small splitting between the interferometer arms can be expressed as [59, 127]

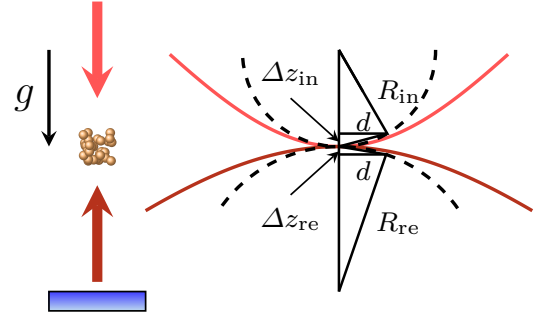


Fig. 5.5: Influence of wavefront curvatures R_{in} of the incident wave and R_{re} of the retroreflected wave. An atom at a radial distance d from the RAMAN beam center experiences a reduced effective wave vector k_{eff} due to its offset $\Delta z_{\text{in}} - \Delta z_{\text{re}}$, making transverse expansion a cause of a bias acceleration.

$$\begin{aligned} \Delta\phi_i^{\text{wf}} \approx & k_{\text{eff},i} \left[(\sigma_a(t_{\text{TOF}}))^2 \left(\frac{1}{R_{\text{in}}(t_{\text{TOF}})} - \frac{1}{R_{\text{re}}(t_{\text{TOF}})} \right) \right. \\ & - 2(\sigma_a(t_{\text{TOF}} + T))^2 \left(\frac{1}{R_{\text{in}}(t_{\text{TOF}} + T)} - \frac{1}{R_{\text{re}}(t_{\text{TOF}} + T)} \right) \\ & \left. + (\sigma_a(t_{\text{TOF}} + 2T))^2 \left(\frac{1}{R_{\text{in}}(t_{\text{TOF}} + 2T)} - \frac{1}{R_{\text{re}}(t_{\text{TOF}} + 2T)} \right) \right]. \end{aligned} \quad (5.8)$$

¹ The retroreflected beam has a different curvature due to the longer distance it is traveling before interacting with the atoms.

Here, the time dependence of $R_{\text{in}}(t)$ and $R_{\text{re}}(t)$, which are calculated using ABCD matrix analysis, takes account for the changing curvature due to beam divergence as experienced by the atoms in motion along the beam over the distance of ≈ 1.65 m between the RAMAN collimator and the retroreflector. Furthermore, $\sigma_a(t)$ is the cloud radius (Equation (4.21)).

In the performed EÖTVÖS ratio measurement, the beam splitting light field is collimated using a shearing interferometer [CVI Laser Optics 09SPM003]. When conservatively assuming a wavefront curvature of $R = 300$ m at the RAMAN collimator, the resulting differential acceleration uncertainty can be calculated using Equation (5.8) and is $\delta\eta^{\text{wf}} = 1.2 \times 10^{-8}$.

5.2.4 Coriolis force

Any velocity component perpendicular to the direction of momentum transfer results in an area A enclosed by the trajectories of an interferometer. Due to the SAGNAC effect [144–146], a corresponding phase shift

$$\Delta\phi^{\text{S}} = \frac{2m}{\hbar} \vec{\Omega} \cdot \vec{A} \quad (5.9)$$

sensitive to rotations $\vec{\Omega}$ around the normal \vec{A} is induced. While the transverse spread of an atomic ensemble due to its temperature is symmetric and thus nulls the SAGNAC phase, a center of mass velocity results in a bias acceleration due to the CORIOLIS force as the laboratory inertial frame rotates around the free falling atoms. As indicated in Figure 5.6, a transverse velocity component $v_{0,\text{EW}}$ on the East-West axis, which can for example be induced by the beam splitting lasers rotating around the free falling atoms [146] or light pressure in the cooling phase, gives rise to a non-vanishing phase shift

$$\Delta\phi^{\text{C}} = 2 \Omega_{\text{eff}} \cdot (v_{0,\text{EW}} \times \vec{k}_{\text{eff}}) T^2. \quad (5.10)$$

Here, $\Omega_{\text{eff}} = \Omega_{\oplus} \cdot \cos(\theta)$ is the effective Earth rotation rate at the instrument location's latitude θ .

For a measurement of the EÖTVÖS ratio, the acceleration bias is strongly suppressed and scales only with the differential center of mass velocity $\delta v_{0,\text{EW}}$:

$$\delta\eta^{\text{C}} \approx \frac{2 \Omega_{\text{eff}} \delta v_{0,\text{EW}}}{g}. \quad (5.11)$$

With an effective rotation rate of Hannover¹ $\Omega_{\text{eff}} = 4.45 \times 10^{-5}$ rad/s and an assumed differential velocity uncertainty $\delta v_{0,\text{EW}} = 1$ mm/s, the uncertainty due to the CORIOLIS force is $\delta\eta^{\text{C}} = 9.1 \times 10^{-9}$.

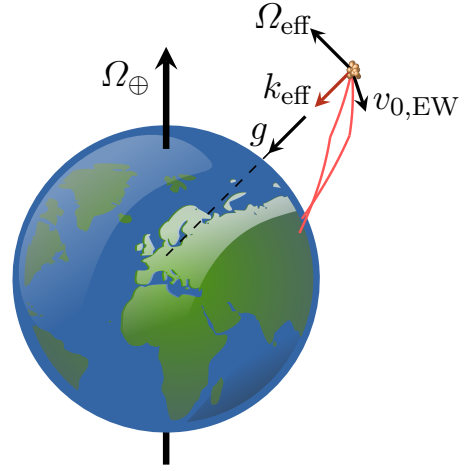


Fig. 5.6: Influence of the Coriolis force on a MACH-ZEHNDER interferometer. An area giving rise to a SAGNAC phase shift, e.g. due to the effective Earth's rotation $\Omega_{\text{eff}} = \Omega_{\oplus} \cdot \cos(\theta)$ where θ is the instrument location's latitude, is enclosed as a cause of a transverse velocity $v_{0,\text{EW}} \perp \vec{k}_{\text{eff}}$. Image modified from Ref. [143].

¹ The calculation of Ω_{eff} is based on a latitude $\theta = 52.376^\circ$ and the length of a sidereal day 86 164.09 s.

5.2.5 Two-photon light shift

Besides the influence of the one-photon AC-STARK shift (see Section 4.3.2 & Section 5.2.1), the presence of a second, off-resonant two-photon light field as in the case of the retroreflected setup in this thesis gives rise to a perturbation of the RAMAN transition frequency and thus a related bias acceleration. Figure 5.7 depicts the case of a DOPPLER-sensitive two-photon transition resonantly coupling the states $|g, p\rangle \rightarrow |e, p + \hbar k_{\text{eff}}\rangle$. While driving the transition, the counterpropagating pair ω_1^{re} and ω_1^{in} off-resonantly couples the second DOPPLER-sensitive $|g, p\rangle \rightarrow |e, p - \hbar k_{\text{eff}}\rangle$ transition with a detuning given by twice the DOPPLER shift ω_D (Equation (2.14)). Furthermore, the states $|e, p + \hbar k_{\text{eff}}\rangle \rightarrow |g, p + 2\hbar k_{\text{eff}}\rangle$ at a detuning given by the DOPPLER shift and the recoil frequency ω_{rec} (Equation (2.13)) are coupled. As derived in Ref. [147], the perturbation $\delta\omega_{\pm\text{TP}}$ due to the energy shifts δE_g and δE_e caused by the off-resonant counterpropagating RAMAN beam pair coupling $|g, p\rangle \rightarrow |e, p \pm \hbar k_{\text{eff}}\rangle$

$$\delta\omega^{\pm\text{TP}} = \frac{\Omega_{\text{eff}}^2}{\pm 8\omega_D} + \frac{\Omega_{\text{eff}}^2}{4(\pm 2\omega_D + 4\omega_{\text{rec}})}, \quad (5.12)$$

with the effective RABI frequency Ω_{eff} . As the polarizations in this thesis in addition allow coupling of the copropagating transitions $|g, p\rangle \rightarrow |e, p\rangle$ & $|g, p \pm \hbar k_{\text{eff}}\rangle \rightarrow |e, p \pm \hbar k_{\text{eff}}\rangle$ (see Section 3.3 & Section 2.1), an additional shift [147]

$$\delta\omega^{\text{TP,co}} \approx \frac{2\Omega_{\text{eff}}^2}{4(\pm\omega_D + \omega_{\text{rec}})} \quad (5.13)$$

is imposed¹. For pulses short enough to assume a constant two-photon light shift over the duration of the pulse, the phase shift for a single species i is [147]

$$\Delta\phi_i^{\text{TP}} = \left(\frac{\delta\omega_{1,i}^{\pm\text{TP}} + \delta\omega_{1,i}^{\text{TP,co}}}{\Omega_{\text{eff},1,i}} - \frac{\delta\omega_{3,i}^{\pm\text{TP}} + \delta\omega_{3,i}^{\text{TP,co}}}{\Omega_{\text{eff},3,i}} \right), \quad (5.14)$$

with the subscript numbers (1,3) indicating the first and third beam splitting pulse. With the considerations above, the bias contribution on the EÖTVÖS ratio due to the two-photon light shift can be determined to $\Delta\eta^{\text{TP}} = 4.1 \times 10^{-9}$ with an assumed uncertainty of 2%.

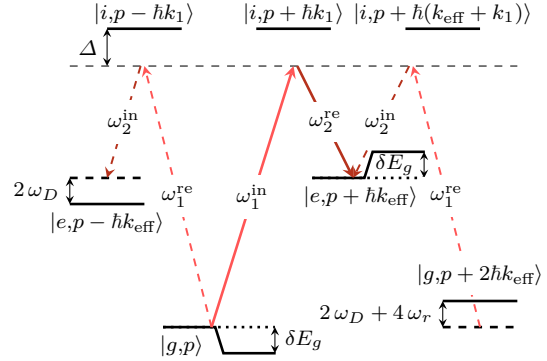


Fig. 5.7: Two-photon light shift on the $|g, p\rangle \rightarrow |e, p + \hbar k_{\text{eff}}\rangle$ transition induced by off-resonant coupling of the second counterpropagating RAMAN beam pair ω_1^{re} and ω_1^{in} . In addition, off-resonant coupling of the copropagating beams has to be considered with the polarizations used in this work. Modified from Ref. [147].

¹ Here, the assumption is made that the copropagating transition is driven at a RABI frequency $2\Omega_{\text{eff}}$ due to the retroreflection setup.

5.2.6 Gravity gradient

Going beyond the phase shift from Equation (2.21) introduces higher order contributions, which depend on the gravity gradient. The largest phase shift terms depending on the gradient are caused by an initial velocity difference and a position offset. Following the full analysis in Ref. [92], the lowest order contributions in dependence of the gradient tensor component $T_{zz} = 3.1 \times 10^{-7} \text{ s}^{-2}$ are

$$\Delta\phi^{\text{gr},z} = k_{\text{eff}} T_{zz} \delta z T^2 \quad (5.15)$$

for a vertical offset δz between two ensembles, and

$$\Delta\phi^{\text{gr},v} = k_{\text{eff}} T_{zz} \delta v_{0,z} T^3, \quad (5.16)$$

accounting for a (differential) velocity $\delta v_{0,z}$. In the presented experiment, a vertical offset uncertainty $\delta z = 300 \mu\text{m}$ leads to an uncertainty of the EÖTVÖS ratio $\delta\eta^{\text{gr},z} = 9.5 \times 10^{-12}$. Assuming an uncertainty of the differential velocity $\delta v_{0,z} = 1 \text{ mm/s}$, the influence on the measurement of the universality of free fall is $\delta\eta^{\text{gr},v} = 6.3 \times 10^{-13}$. The quadratic sum yields an uncertainty due to the gravity gradient of $\delta\eta^{\text{gr}} = 9.5 \times 10^{-12}$. Phase shifts depending on the different recoil transferred in the beam splitting process do not change their sign with a change of the direction of momentum transfer and are thus suppressed in the k -reversal scheme (see Section 4.4.2).

5.3 Summary

The systematic bias contributions $\Delta\eta$ and their uncertainties $\delta\eta$ derived in Sections 5.2.2 – 5.2.6 are listed in Table 5.1 and yield total contributions of $\Delta\eta_{\text{tot}} = -5.4 \times 10^{-8}$ and $\delta\eta_{\text{tot}} = 3.1 \times 10^{-8}$. Taking into account the statistical uncertainty¹ σ_η and the bias $\Delta\eta_{\text{tot}}$, the EÖTVÖS ratio can be determined to $\eta_{\text{Rb,K}} = (0.3 \pm 5.4) \times 10^{-7}$.

A variety of significantly smaller systematic errors, and methods for error mitigation exist beyond the discussion presented here [59, 92]. For example, the implementation of a tip-tilt mirror allows to significantly reduce the influence of the CORIOLIS force [55, 56, 146]. As a second example, due its linearity in the effective RABI frequency, the two-photon light shift bias (see Section 5.2.5)

Table 5.1: Overview of systematic effects $\Delta\eta$ perturbing the EÖTVÖS ratio determination, and their uncertainties $\delta\eta$. The uncertainties are treated to be uncorrelated at the level of inaccuracy.

Contribution	$\Delta\eta$	$\delta\eta$
Second-order ZEEMAN effect	-5.8×10^{-8}	2.6×10^{-8}
Wavefront aberration	0	1.2×10^{-8}
CORIOLIS force	0	9.1×10^{-9}
Two-photon light shift	4.1×10^{-9}	8.2×10^{-11}
Effective wave vector	0	1.3×10^{-9}
First-order gravity gradient	0	9.5×10^{-12}
Total	-5.4×10^{-8}	3.1×10^{-8}

¹ At the current level of resolution, the systematic uncertainty $\delta\eta_{\text{tot}}$ has no relevance in the quadratic sum.

can be reduced by changing the beam splitting laser power and computing a linear combination extrapolating to zero bias with a reduced short-term sensitivity [127]. As explained in the outlook in Chapter 6, techniques are available to further reduce the uncertainty of the currently limiting bias contributions represented by the second-order ZEEMAN shift caused by a residual magnetic field gradient (see Section 5.2.2), and wavefront aberration (see Section 5.2.3).

CHAPTER 6

Outlook

*“Science shall never find that formula by which its necessary character could be proved.
Actually science itself might cease if we were to find the clue to the secret.”*

— L. EÖTVÖS, 1890 [30]

In the scope of this thesis, the first potassium matter wave interferometer was demonstrated, and the universality of free fall (UFF) was tested utilizing matter wave interferometry with two different species, rubidium and potassium, for the first time. The measurement yielded the EÖTVÖS ratio $\eta_{\text{Rb,K}} = (0.3 \pm 5.4) \times 10^{-7}$. Due to the comparably low contrast of the potassium interferometer and technical noise influencing it, the measurement was limited by statistical uncertainty. This limit lies about one order of magnitude above the total systematic uncertainty $\delta\eta_{\text{tot}} = 3.1 \times 10^{-8}$. In this Chapter, methods to increase the system’s performance are discussed. Recently demonstrated noise reduction of the potassium interferometer will allow an improvement of the EÖTVÖS ratio measurement to a level of parts in 10^8 within a few hours of integration. It is furthermore projected that the use of an optical dipole trap as a common source will constrain systematic uncertainties to the ppb level. This thesis is closed with a look into the future of matter wave tests of gravity. The use of large-scale apparatuses such as the “very long baseline atom interferometry” facility, which is currently planned in Hannover, will enable tests of the UFF at a level of a few parts in 10^{13} . Finally, the extension of UFF tests into space bring inaccuracies at a scale of 2×10^{-15} into reach.

6.1 Overcoming current limitations

Statistical uncertainty

The resolution of the EÖTVÖS ratio $\eta_{\text{Rb,K}}$ of rubidium and potassium performed in this thesis was limited by statistical uncertainty of the potassium interferometer due to both, the limited integration time and the short-term stability; being affected by technical noise and low contrast. Due to the leading order noise contribution not being common to the rubidium and potassium interferometer, noise suppression [49, 139, 140] was not observable up to now. As shown in Section 4.4, various steps toward a sensitivity enhancement have been taken. Technical improvements have allowed to increase the RAMAN beam splitting stability (see Section 4.4), thus the measurement contrast and the pulse separation time remain the most important levers to achieve a lower short-term instability. In order to test the potential of these improvements, a midfringe instability measurement was obtained using an inertial-sensitive interferometer with a pulse separation $T = 25$ ms with a contrast of $C = 3\%$. The assumption that the potassium

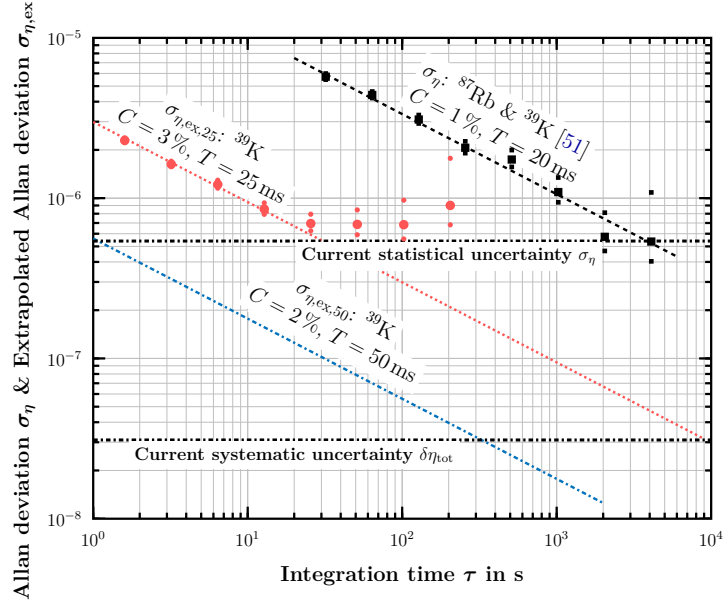


Figure 6.1: ALLAN deviation extrapolated under the assumption that the potassium interferometer constitutes the leading uncertainty of the measurement, based on a demonstration midfringe measurement obtained at a pulse separation time $T = 25$ ms with a contrast of $C = 3\%$ (red circles and dotted red line). The measurement is subject to a drift caused by slow variations in the signal offset that can be compensated. For comparison, the ALLAN deviations for $T = 50$ ms, $C = 2\%$ (dashdotted blue line), and for the first dual species UFF measurement with $T = 20$ ms, $C = 1\%$ (black squares and dashed black line) are displayed.

interferometer constitutes the leading uncertainty of the measurement is made. Because of a drift affecting the midfringe measurement, a data acquisition protocol repetitively scanning a full fringe is considered¹. The largest pulse separation times demonstrated so far in a potassium single species configuration were $T = 50$ ms, and yielded a contrast of $C = 2\%$. As can be seen from the ALLAN deviation $\sigma_{\eta,ex}$ (Figure 6.1) of an extrapolated EÖTVÖS ratio measurement, a short-term stability that is improved by one order of magnitude can be derived from the data taken at $T = 25$ ms. With this performance, the current statistical uncertainty $\sigma_\eta = 5.4 \times 10^{-7}$ can be achieved after ≈ 30 s of integration. Accordingly, the current systematic uncertainty $\delta\eta_{tot} = 3.1 \times 10^{-8}$ is in reach after ≈ 3 h of integration. For a measurement at $T = 50$ ms with a contrast of $C = 2\%$, the single-shot resolution exceeds the current statistical limit, allowing for a much faster integration toward the systematic limit.

It was shown previously, that seismic noise is the leading order noise contribution for a single species rubidium gravimeter operated in the present apparatus [90]. The same holds true in state-of-the-art matter wave gravimeters [148–150], however, it has been demonstrated that using correlation with a high bandwidth classical seismometer, this noise can be corrected for [151]. In a dual species measurement a noise contribution that is common to both interferometers allows common mode rejection [49, 139, 140]. Here, the degree of suppression is governed by how well the interferometer scaling factors of the two species and their sensitivity functions, that is,

¹ In comparison to a two-slope midfringe measurement, which requires both, good knowledge and high stability of the measurement contrast, the full fringe scan increases the instability by a factor of $\sqrt{2}$.

their pulse separation times and RABI frequencies, are matched (see Section 2.1.3). Contrary to an experiment employing isotopes of the same species with very similar transition wavelengths matching the scaling factors and RABI frequencies of two different species is subject to much tighter constraints due to wavelength differences that typically lie on the order of terahertz or more. For the case of rubidium and potassium, a conservative estimation promises a suppression of vibrational noise by a factor > 100 without much technical effort [139].

Employing BRAGG transitions [86, 152] as beam splitters instead of RAMAN transitions is an interesting alternative to increase the sensitivity of a matter wave interferometer. Given sufficient laser power, n^{th} -order BRAGG processes can be driven, increasing the transferred momentum $2n \hbar k_{\text{eff}}$ linearly with the diffraction order. It is worth noting that a trade-off has to be considered when weighing a scaling factor matching against a trajectory matching, which is beneficial for decreasing systematic effects.

Systematic uncertainty

Conservative traps as a source of ultracold ensembles with well controlled release and expansion dynamics for matter wave interferometry are nowadays widely spread [55–58, 137, 153]. The use of an optical dipole trap as a common source for rubidium and potassium features evaporative cooling and the possibility to sympathetically cool one species [154, 155]. The apparatus presented in this thesis was previously used to generate BOSE-EINSTEIN condensates in an optical dipole trap (ODT) at a wavelength of $\lambda_{\text{ODT}} \approx 2 \mu\text{m}$ [102, 156]. Due to its efficient loading and the low differential AC-STARK shift exerted on the $^2S_{1/2} \rightarrow ^2P_{3/2}$ fine structure transitions of rubidium [102] and potassium, the use of an ODT of this kind holds great potential as a source for matter wave interferometry, even though the statistical resolution may be decreased due to higher quantum projection noise as consequence of lower flux as compared to a thermal source¹. As shown above, the recent improvements will soon allow to reach the current systematic limit, which is constrained to $\delta\eta_{\text{tot}} = 3.1 \times 10^{-8}$ (see Section 5.2), within reasonable integration time. Next to the potential in improving the contrast and thus sensitivity of the measurement, the optical dipole trap is an important tool to handle the systematic uncertainty of a dual species measurement [51, 156], which is mainly set by the second-order ZEEMAN shift, caused by spatial

Table 6.1: Comparison of the current systematic uncertainties $\delta\eta$ of the EÖTVÖS ratio to the improved uncertainties $\delta\eta^{\text{adv}}$ achieved by using an optical dipole trap. The uncertainties are treated to be uncorrelated at the level of inaccuracy.

Contribution	$\delta\eta$	$\delta\eta^{\text{adv}}$
Second-order ZEEMAN effect	2.6×10^{-8}	3.0×10^{-9}
Wavefront aberration	1.2×10^{-8}	3.0×10^{-9}
CORIOLIS force	9.1×10^{-9}	1.0×10^{-11}
Two-photon light shift	8.2×10^{-11}	8.2×10^{-11}
Effective wave vector	1.3×10^{-9}	1.3×10^{-9}
First-order gravity gradient	9.5×10^{-12}	1.0×10^{-13}
Total	3.1×10^{-8}	4.4×10^{-9}

¹ Based on sympathetic cooling, degenerate mixtures of 10^6 atoms of ^{87}Rb and 2×10^5 atoms of ^{39}K [155] and 10^4 atoms of ^{87}Rb & ^{41}K each [154] have been demonstrated.

variations of the magnetic field. This shift is not suppressed by the k -reversal scheme due to the different trajectories of the two species. Next to a better characterization of residual gradients using an ODT source, holding in an optical trap also allows to add additional waiting time to make sure any magnetic fields are completely switched off. Furthermore, wave front aberrations affect the interferometer phase by variations of the effective wave vector throughout the sequence [127]. Reducing the ensemble temperature and the related expansion by means of evaporative cooling allows to decrease the influence of wave front distortions. By creating a common potential that is only different to two species by the difference in their polarizability and the gravitational sag, an optical trap allows to carefully constrain the starting parameters of the two ensembles, such as the differential expansion and center of mass velocity, and the center of mass colocation. It furthermore becomes possible to map the wave front by precisely scanning the initial position of the source. Moreover, in an optical trap the magnetic field is a free parameter allowing tuning of the scattering properties of trapped atoms via FESHBACH resonances [154, 155, 157–159]. In the case of mixtures of rubidium and potassium, addressing these is necessary to tune the scattering length in order to allow for sympathetic cooling and to gain full control over the miscibility.

A variety of methods to achieve a high flux source of ultracold mixtures of rubidium and potassium are available. Using the anti-HELMHOLTZ coil pair that generates the 3D MOT magnetic quadrupole field, gradients up to $B' = 45 \text{ G/cm}$ can be realized with the currently operated power supply and water cooling system. Next to BOSE-EINSTEIN condensate generation in a weak hybrid trap [156], this enables experimental schemes of magnetically aided forced evaporation in an optical trap as demonstrated in [160]. Besides creating an ultracold dual species source *per se*, further temperature reduction is possible by atom optical lenses, that utilize a harmonic potential to stop the expansion of an atomic ensemble. The effectiveness of this method in increasing the contrast of matter wave interferometers has recently been shown in [55, 56, 58], where magnetic potentials were employed. In addition, the applicability of optical potential for this purpose has been demonstrated [137]. For the apparatus presented in this thesis, one option is to superimpose a focused dipole trap beam with the RAMAN beam on a dichroic mirror to enable optical matter wave lensing.

Table 6.1 shows the current uncertainty budget and improved uncertainty contributions $\delta\eta^{\text{adv}}$ assuming the use of an optical dipole trap. The considered extrapolation is based on a temperature of the Rb-K mixture of $10 \mu\text{K}$. The assumed ODT parameters are a horizontal trap alignment uncertainty of 1.5° , 3 ms trap switch-off time and an uncertainty of the trap power before release of 0.2% [51]. The improved total uncertainty $\delta\eta_{\text{tot}}^{\text{adv}} = 4.4 \times 10^{-9}$. Hence, by utilizing the ODT as a source, a ppb-level test of the UFF with rubidium and potassium can be performed in the near future.

6.2 The future of matter wave tests of gravity

Large scale apparatuses and microgravity experiments

Matter wave tests of gravity allow tests of novel effects that find their origin in quantum mechanics and cannot be observed with classical matter [169–172]. Furthermore, it may be possible to further investigate the nature of dark energy with matter wave interferometry [173]. In the sector of UFF tests, numerous initiatives were started with quantum objects. Table 6.2 provides an overview on proposed tests. The scope of these experiments can be split into the class of tests that are ground-based, and the ones in microgravity. In attempt to set new records for matter wave tests of the UFF, large-scale apparatuses such as 10 m-fountains are currently being operated by

Table 6.2: Comparison of proposed matter wave tests of the UFF with respect to their type of experiment, the choice of test masses, the maximum free evolution time $2T$ and the proposed inaccuracy $\delta\eta_{\text{tot}}$. The experiments are categorized into ground-based and microgravity tests. Note that for some tests no detailed systematics assessment is available.

	Experiment	Type	Ref.	Species	$2T$ in s	$\delta\eta_{\text{tot}}$
Ground-based	Palo Alto	10 m-fountain	[54]	^{87}Rb vs ^{85}Rb	1.4	1×10^{-15}
	Wūhàn	10 m-fountain	[161]	^6Li vs ^{85}Rb	1.4	–
	Berkeley	Lattice interferometer	[94]	^6Li vs ^7Li	10 ^a	1×10^{-14}
	Hannover	Lab-based ^{b c}	[51]	^{87}Rb vs ^{39}K	0.2	4×10^{-9}
	Hannover, VLBAI	10 m-fountain	[162]	^{87}Rb vs $^{168/170}\text{Yb}$	1.4	7×10^{-13}
μ -gravity	Bordeaux, ICE	Parabola flights	[163]	^{87}Rb vs ^{39}K	2.0	5×10^{-11}
	CAL	Space station	[65]	^{87}Rb vs ^{41}K	4.0	1×10^{-11}
	STE-QUEST	Satellite mission ^{c d}	[60]	^{87}Rb vs ^{85}Rb	10	2×10^{-15}

^a The proposed geometry foresees a guided interferometer that allows to achieve long wave packet separation times.

^b The experiment is presented in this thesis.

^c A detailed assessment of systematic effects is available.

^d Prestudies in microgravity for the STE-QUEST mission, and possible extensions to ^{41}K are performed in the drop tower experiments within the QUANTUS project [57, 58, 164, 165], the PRIMUS project [166, 167], and in the sounding rocket mission MAIUS [168].

groups in Palo Alto, USA [54–56] and Wuhan, China [161]. In the ground-based sector, these instruments promise to be among the most sensitive sensors and open up great potential for groundbreaking developments for tests of the UFF. With this motivation, a fountain of this kind is currently being planned in Hannover, Germany. This device will be operated with rubidium and ytterbium to examine new frontiers in “very long baseline atom interferometry” (VLBAI). Proposed aims are a test of the UFF at a level of a few parts in 10^{13} and record inaccuracy for absolute measurements of gravitational acceleration and its derivatives in close cooperation with geodesy. Moreover, the feasibility of novel high fidelity beam splitters, and the applicability of non-classical states to overcome the quantum projection noise will be investigated [174–179]. Tests in microgravity benefit from the possibility of reaching very long free fall times due to the lifted constraint of limited vacuum vessel size. More importantly, however, more abilities to reduce systematic effects as compared to ground-based experiments are available [59, 60] and allow to constrain systematic error budgets to the level of parts in 10^{15} . As a trade-off, microgravity missions suffer from typically very high technology-readiness requirements, limited maintenance access, and, e.g. in the case of the ZARM drop tower in Bremen, from low repetition rates¹. A variety of new test mass pairs is considered, however, proposals accessing inaccuracies of the EÖTVÖS ratio on the order of 10^{-13} and below are subject to extremely tight experimental constraints. For example, in the STE-QUEST mission, the initial position of the test species’ centers of mass must coincide on the order of 1 nm, and the differential velocity must not

¹ The EINSTEIN-elevator [180], a high-repetition, free fall simulator, which is currently being planned in Hannover, will fill the gap.

be larger than 0.3 nm/s , to suppress bias contributions due to the gravity gradient [59, 60]. Considering the displacement of the clouds in the preparation phase caused by the relatively strong second-order ZEEMAN shift due to the required FESHBACH fields, raises high demands on the magnetic field quality in such an experiment. This highlights the importance of a careful analysis of all systematic parameters, such as the quantum miscibility, during the search for a test mass pair. In the STE-QUEST mission proposal, this option was not available because of the dual use of the experiment as an atomic clock and the related additional constraints.

Conclusion

Different tests of gravity are subject to different constraints, e.g. the available test masses. For instance, matter wave tests rely on laser cooling and the miscibility of test species, torsion balances underly certain constraints such as conductivity, magnetic properties [61] and a maximum density difference of the two species [181]. Most definitely, however, pursuing new record accuracies for measurements of the universality of free fall with a further extended set of test masses is a very promising strategy to find the missing piece for a self-consistent “quantum gravity” framework valid over all energy scales. There is no doubt that many of the currently followed experimental strategies, may they be classical or based on quantum mechanics, will allow exciting insights in the nature of gravity and its links to quantum mechanics. By opening up the door toward matter wave tests of the UFF using different species, the results of this thesis set part of the foundation for a number of future tests and are an important step on the road of seeking a “theory of everything”.

Bibliography

- [1] H. Hertz,
‘Die Constitution der Materie: Eine Vorlesung über die Grundlagen der Physik aus dem Jahre 1884’,
Springer, Berlin (1999) (cit. on pp. 1, 3).
- [2] A. Einstein,
‘Über einen die Erzeugung und Verwandlung des Lichtes betreffenden heuristischen Gesichtspunkt’,
Ann. Phys. **322**, 132–148 (1905) (cit. on p. 1).
- [3] L. de Broglie,
‘Recherches sur la théorie des Quantas’,
PhD thesis, Sorbonne Paris (1924) (cit. on p. 1).
- [4] W. Heisenberg,
‘Über quantentheoretische Umdeutung kinematischer und mechanischer Beziehungen.’,
Zeitschrift für Physik **33**, 879–893 (1925) (cit. on p. 1).
- [5] E. Schrödinger,
‘Quantisierung als Eigenwertproblem’,
Ann. Phys. **384**, 361–376 (1926) (cit. on p. 1).
- [6] E. Schrödinger,
‘Quantisierung als Eigenwertproblem’,
Ann. Phys. **384**, 489–527 (1926) (cit. on p. 1).
- [7] M. Born,
‘Zur Quantenmechanik der Stoßvorgänge’,
Zeitschrift für Physik **37**, 863–867– (1926) (cit. on p. 1).
- [8] W. Heisenberg,
‘Über den anschaulichen Inhalt der quantentheoretischen Kinematik und Mechanik’,
Zeitschrift für Physik **43**, 172–198– (1927) (cit. on p. 1).
- [9] W. Pauli,
‘Zur Quantenmechanik des magnetischen Elektrons’,
Zeitschrift für Physik **43**, 601–623– (1927) (cit. on p. 1).
- [10] C. G. Parthey *et al.*,
‘Improved Measurement of the Hydrogen $1S - 2S$ Transition Frequency’,
Phys. Rev. Lett. **107**, 203001– (2011) (cit. on p. 1).

- [11] A. Matveev *et al.*,
'Precision Measurement of the Hydrogen $1S - 2S$ Frequency via a 920-km Fiber Link',
Phys. Rev. Lett. **110**, 230801– (2013) (cit. on p. 1).
- [12] A. Einstein,
'Die Grundlage der allgemeinen Relativitätstheorie',
Ann. Phys. **49**, 769–822 (1916) (cit. on p. 1).
- [13] J. B. Hartle,
'Gravity: an Introduction to Einstein's General Relativity',
Addison-Wesley, San Francisco (2003) (cit. on p. 1).
- [14] C. M. Will,
'The Confrontation between General Relativity and Experiment',
Living Rev. Relativity **17**, (2014) (cit. on p. 2).
- [15] A. Einstein,
'Über Gravitationswellen',
Sitzungsbericht Kgl. Preuss. Akad. Wiss. (1918) (cit. on p. 2).
- [16] J. M. Weisberg, J. H. Taylor, and L. A. Fowler,
'Gravitational Waves from an Orbiting Pulsar',
Scientific American **245**, 47–82 (1981) (cit. on p. 2).
- [17] F. Acernese *et al.*,
'Virgo status',
Classical and Quantum Gravity **25**, 184001– (2008) (cit. on p. 2).
- [18] G. M. Harry *et al.*,
'Advanced LIGO: the next generation of gravitational wave detectors',
Classical and Quantum Gravity **27**, 084006– (2010) (cit. on p. 2).
- [19] M. Punturo and H. Lück,
'Toward a third generation of gravitational wave observatories',
General Relativity and Gravitation **43**, 363–385– (2011) (cit. on p. 2).
- [20] H. Georgi and S. L. Glashow,
'Unity of All Elementary-Particle Forces',
Phys. Rev. Lett. **32**, 438–441 (1974) (cit. on p. 2).
- [21] J. Franck and G. Hertz,
'Über Zusammenstöße zwischen Elektronen und Molekülen des Quecksilberdampfes und die Ionisierungsspannung desselben',
Verh. Dtsch. Phys. Ges. **16**, 457–467 (1914) (cit. on p. 2).
- [22] C. Jönsson,
'Elektroneninterferenzen an mehreren künstlich hergestellten Feinspalten',
161, 454–474– (1961) (cit. on p. 2).
- [23] H. Rauch, W. Treimer, and U. Bonse,
'Test of a single crystal neutron interferometer',
Physics Letters A **47**, 369–371 (1974) (cit. on p. 2).
- [24] R. V. Pound and G. A. Rebka,
'Apparent Weight of Photons',
Phys. Rev. Lett. **4**, 337–341 (1960) (cit. on pp. 2, 4).

- [25] R. V. Pound and J. L. Snider,
‘Effect of Gravity on Nuclear Resonance’,
Phys. Rev. Lett. **13**, 539–540 (1964) (cit. on pp. 2, 4).
- [26] R. V. Pound and J. L. Snider,
‘Effect of Gravity on Gamma Radiation’,
Phys. Rev. **140**, B788–B803 (1965) (cit. on pp. 2, 4).
- [27] R. F. C. Vessot, M. W. Levine, E. M. Mattison, E. L. Blomberg, T. E. Hoffman, G. U. Nystrom, B. F. Farrel, R. Decher, P. B. Eby, C. R. Baugher, J. W. Watts, D. L. Teuber, and F. D. Wills,
‘Test of Relativistic Gravitation with a Space-Borne Hydrogen Maser’,
Phys. Rev. Lett. **45**, 2081–2084 (1980) (cit. on pp. 2, 4).
- [28] C. Lämmerzahl,
‘The search for quantum gravity effects I’,
Appl. Phys. B **84**, 551–562– (2006) (cit. on pp. 2, 4).
- [29] S. G. Turyshev, V. T. Toth, G. Kinsella, S.-C. Lee, S. M. Lok, and J. Ellis,
‘Support for the Thermal Origin of the Pioneer Anomaly’,
Phys. Rev. Lett. **108**, 241101– (2012) (cit. on p. 2).
- [30] C. W. Misner, K. S. Thorne, and J. A. Wheeler,
‘Gravitation’,
Freeman, San Francisco (1973) (cit. on pp. 2, 75).
- [31] T. M. Fortier *et al.*,
‘Precision Atomic Spectroscopy for Improved Limits on Variation of the Fine Structure Constant and Local Position Invariance’,
Phys. Rev. Lett. **98**, 070801– (2007) (cit. on pp. 2, 4).
- [32] N. Ashby, T. P. Heavner, S. R. Jefferts, T. E. Parker, A. G. Radnaev, and Y. O. Dudin,
‘Testing Local Position Invariance with Four Cesium-Fountain Primary Frequency Standards and Four NIST Hydrogen Masers’,
Phys. Rev. Lett. **98**, 070802– (2007) (cit. on pp. 2, 4).
- [33] S. Blatt *et al.*,
‘New Limits on Coupling of Fundamental Constants to Gravity Using ^{87}Sr Optical Lattice Clocks’,
Phys. Rev. Lett. **100**, 140801– (2008) (cit. on pp. 2, 4).
- [34] V. A. Kostelecký and C. D. Lane,
‘Constraints on Lorentz violation from clock-comparison experiments’,
Phys. Rev. D **60**, 116010– (1999) (cit. on pp. 2, 4).
- [35] M. A. Hohensee, R. Lehnert, D. F. Phillips, and R. L. Walsworth,
‘Particle-Accelerator Constraints on Isotropic Modifications of the Speed of Light’,
Phys. Rev. Lett. **102**, 170402– (2009) (cit. on pp. 2, 4).
- [36] M. A. Hohensee, N. Leefer, D. Budker, C. Harabati, V. A. Dzuba, and V. V. Flambaum,
‘Limits on Violations of Lorentz Symmetry and the Einstein Equivalence Principle using Radio-Frequency Spectroscopy of Atomic Dysprosium’,
Phys. Rev. Lett. **111**, 050401– (2013) (cit. on pp. 2, 4).

- [37] J. G. Williams, S. G. Turyshev, and D. H. Boggs, ‘Progress in Lunar Laser Ranging Tests of Relativistic Gravity’, *Phys. Rev. Lett.* **93**, 261101– (2004) (cit. on p. 3).
- [38] J. G. Williams, S. G. Turyshev, and D. H. Boggs, ‘Lunar laser ranging tests of the equivalence principle’, *Classical and Quantum Gravity* **29**, 184004– (2012) (cit. on p. 3).
- [39] L. Eötvös, ‘Über die Anziehung der Erde auf verschiedene Substanzen’, *Mathematische and naturwissenschaftliche Berichte aus Ungarn* **8**, 65– (1889) (cit. on p. 3).
- [40] L. Eötvös, D. Pekár, and E. Fekete, ‘Beiträge zum Gesetze der Proportionalität von Trägheit und Gravität’, *Ann. Phys.* **373**, 11–66 (1922) (cit. on p. 3).
- [41] S. Schlamminger, K.-Y. Choi, T. A. Wagner, J. H. Gundlach, and E. G. Adelberger, ‘Test of the Equivalence Principle Using a Rotating Torsion Balance’, *Phys. Rev. Lett.* **100**, 041101– (2008) (cit. on pp. 3, 14, 15).
- [42] T. M. Niebauer, M. P. McHugh, and J. E. Faller, ‘Galilean test for the fifth force’, *Phys. Rev. Lett.* **59**, 609–612 (1987) (cit. on pp. 3, 14, 15).
- [43] P. C. C. Freire, M. Kramer, and N. Wex, ‘Tests of the universality of free fall for strongly self-gravitating bodies with radio pulsars’, *Classical Quantum Gravity* **29**, 184007– (2012) (cit. on p. 3).
- [44] S. M. Ransom *et al.*, ‘A millisecond pulsar in a stellar triple system’, *Nature (London)* **505**, 520–524 (2014) (cit. on p. 3).
- [45] P. Touboul, G. Métris, V. Lebat, and A. Robert, ‘The MICROSCOPE experiment, ready for the in-orbit test of the equivalence principle’, *Classical Quantum Gravity* **29**, 184010– (2012) (cit. on p. 3).
- [46] A. Peters, K.-Y. Chung, and S. Chu, ‘Measurement of gravitational acceleration by dropping atoms’, *Nature (London)* **400**, 849–852 (1999) (cit. on pp. 3, 4, 50).
- [47] S. Merlet, Q. Bodart, N. Malossi, A. Landragin, F. Pereira Dos Santos, O. Gitlein, and L. Timmen, ‘Comparison between two mobile absolute gravimeters: optical versus atomic interferometers’, *Metrologia* **47**, L9– (2010) (cit. on pp. 3, 4).
- [48] S. Fray, C. A. Diez, T. W. Hänsch, and M. Weitz, ‘Atomic Interferometer with Amplitude Gratings of Light and Its Applications to Atom Based Tests of the Equivalence Principle’, *Phys. Rev. Lett.* **93**, 240404– (2004) (cit. on pp. 3, 4, 14, 15).
- [49] A. Bonnin, N. Zahzam, Y. Bidet, and A. Bresson, ‘Simultaneous dual-species matter-wave accelerometer’, *Phys. Rev. A* **88**, 043615– (2013) (cit. on pp. 3, 4, 14, 15, 24, 65, 75, 76).

- [50] M. G. Tarallo, T. Mazzoni, N. Poli, D. V. Sutyryn, X. Zhang, and G. M. Tino, ‘Test of Einstein Equivalence Principle for 0-Spin and Half-Integer-Spin Atoms: Search for Spin-Gravity Coupling Effects’, *Phys. Rev. Lett.* **113**, 023005– (2014) (cit. on pp. 3, 4, 14, 15).
- [51] D. Schlippert, J. Hartwig, H. Albers, L. L. Richardson, C. Schubert, A. Roura, W. P. Schleich, W. Ertmer, and E. M. Rasel, ‘Quantum Test of the Universality of Free Fall’, *Phys. Rev. Lett.* **112**, 203002 (2014) (cit. on pp. 3, 4, 14, 15, 36, 63, 76–79).
- [52] R. Colella, A. W. Overhauser, and S. A. Werner, ‘Observation of Gravitationally Induced Quantum Interference’, *Phys. Rev. Lett.* **34**, 1472–1474 (1975) (cit. on p. 4).
- [53] S. Fray and M. Weitz, ‘Atom-Based Test of the Equivalence Principle’, *Space Sci. Rev.* **148**, 225–232– (2009) (cit. on p. 4).
- [54] S. Dimopoulos, P. W. Graham, J. M. Hogan, and M. A. Kasevich, ‘Testing General Relativity with Atom Interferometry’, *Phys. Rev. Lett.* **98**, 111102– (2007) (cit. on pp. 4, 79).
- [55] S. M. Dickerson, J. M. Hogan, A. Sugarbaker, D. M. S. Johnson, and M. A. Kasevich, ‘Multiaxis Inertial Sensing with Long-Time Point Source Atom Interferometry’, *Phys. Rev. Lett.* **111**, 083001– (2013) (cit. on pp. 4, 72, 77–79).
- [56] A. Sugarbaker, S. M. Dickerson, J. M. Hogan, D. M. S. Johnson, and M. A. Kasevich, ‘Enhanced Atom Interferometer Readout through the Application of Phase Shear’, *Phys. Rev. Lett.* **111**, 113002– (2013) (cit. on pp. 4, 72, 77–79).
- [57] T. van Zoest *et al.*, ‘Bose-Einstein Condensation in Microgravity’, *Science* **328**, 1540–1543 (2010) (cit. on pp. 4, 77, 79).
- [58] H. Müntinga *et al.*, ‘Interferometry with Bose-Einstein Condensates in Microgravity’, *Phys. Rev. Lett.* **110**, 093602– (2013) (cit. on pp. 4, 54, 77–79).
- [59] C. Schubert *et al.*, ‘Differential atom interferometry with ^{87}Rb and ^{85}Rb for testing the UFF in STE-QUEST’, arXiv:1312.5963 (cit. on pp. 4, 46, 69, 72, 79, 80).
- [60] D. Aguilera *et al.*, ‘STE-QUEST - Test of the Universality of Free Fall Using Cold Atom Interferometry’, *Classical and Quantum Gravity* **31**, 115010– (2014) (cit. on pp. 4, 46, 79, 80).
- [61] E. G. Adelberger, J. H. Gundlach, B. R. Heckel, S. Hoedl, and S. Schlamminger, ‘Torsion balance experiments: A low-energy frontier of particle physics’, *Prog. Part. Nucl. Phys.* **62**, 102–134 (2009) (cit. on pp. 4, 80).
- [62] S. Chu, ‘Nobel Lecture: The manipulation of neutral particles’, *Rev. Mod. Phys.* **70**, 685–706 (1998) (cit. on pp. 4, 34, 63).

- [63] W. D. Phillips,
'Nobel Lecture: Laser cooling and trapping of neutral atoms',
Rev. Mod. Phys. **70**, 721–741 (1998) (cit. on pp. 4, 34, 63).
- [64] M. A. Hohensee, H. Müller, and R. B. Wiringa,
'Equivalence Principle and Bound Kinetic Energy',
Phys. Rev. Lett. **111**, 151102– (2013) (cit. on pp. 4, 5, 13–15).
- [65] H. Müller,
'Quantum mechanics, matter waves, and moving clocks',
Atom Interferometry, Proceedings of the International School of Physics "Enrico Fermi" Course CLXXXVIII, ed. by G. M. Tino and M. A. Kasevich, Società Italiana di Fisica and IOS Press (2013) (cit. on pp. 4, 5, 15, 16, 79).
- [66] J. Leitner and S. Okubo,
'Parity, Charge Conjugation, and Time Reversal in the Gravitational Interaction',
Phys. Rev. **136**, B1542–B1546 (1964) (cit. on p. 4).
- [67] C. Lämmerzahl,
'Quantum tests of the foundations of general relativity',
Classical and Quantum Gravity **15**, 13– (1998) (cit. on p. 4).
- [68] C. Lämmerzahl,
'Quantum Tests of Space-Time Structures',
Proceedings of the International School of Cosmology and Gravitation, Course XV, ed. by P. Bergmann, V. DeSabbata, G. Gillies, and P. Pronin, World Scientific, Singapore (1998) (cit. on p. 4).
- [69] C.-H. Hsieh, P.-Y. Jen, K.-L. Ko, K.-Y. Li, W.-T. Ni, S.-S. Pan, Y.-H. Shih, and R.-J. Tyan,
'The Equivalence Principle Experiment for Spin-Polarized Bodies',
Mod. Phys. Lett. A **04**, 1597–1603 (1989) (cit. on p. 4).
- [70] E. Göklü and C. Lämmerzahl,
'Metric fluctuations and the weak equivalence principle',
Classical Quantum Gravity **25**, 105012– (2008) (cit. on pp. 4, 13).
- [71] S. A. Diddams, J. C. Bergquist, S. R. Jefferts, and C. W. Oates,
'Standards of Time and Frequency at the Outset of the 21st Century',
Science **306**, 1318–1324 (2004) (cit. on p. 4).
- [72] G. Audi, A.H. Wapstra, and C. Thibault,
'The $A_{ME}2003$ atomic mass evaluation: (II). Tables, graphs and references',
Nucl. Phys. A **729**, 337–676 (Dec. 2003) (cit. on pp. 5, 15).
- [73] J. R. de Laeter, J. K. Böhlke, P. De Bièvre, H. Hidaka, H. S. Peiser, K. J. R. Rosman, and P. D. P. Taylor,
'Atomic weights of the elements. Review 2000 (IUPAC Technical Report)',
Pure Appl. Chem. **75**, 683– (2003) (cit. on pp. 5, 14, 15).
- [74] T. Damour,
'Theoretical aspects of the equivalence principle',
Classical Quantum Gravity **29**, 184001– (2012) (cit. on pp. 4, 13–15).

- [75] D. Colladay and V. A. Kostelecký,
'*CPT* violation and the standard model',
Phys. Rev. D **55**, 6760–6774 (1997) (cit. on pp. 4, 13).
- [76] D. Colladay and V. A. Kostelecký,
'Lorentz-violating extension of the standard model',
Phys. Rev. D **58**, 116002– (1998) (cit. on pp. 4, 13).
- [77] V. A. Kostelecký,
'Gravity, Lorentz violation, and the standard model',
Phys. Rev. D **69**, 105009– (2004) (cit. on pp. 4, 13).
- [78] V. A. Kostelecký and J. D. Tasson,
'Prospects for Large Relativity Violations in Matter-Gravity Couplings',
Phys. Rev. Lett. **102**, 010402– (2009) (cit. on pp. 4, 13).
- [79] V. A. Kostelecký and J. D. Tasson,
'Matter-gravity couplings and Lorentz violation',
Phys. Rev. D **83**, 016013– (2011) (cit. on pp. 4, 13).
- [80] M. A. Hohensee, S. Chu, A. Peters, and H. Müller,
'Equivalence Principle and Gravitational Redshift',
Phys. Rev. Lett. **106**, 151102– (2011) (cit. on pp. 4, 13).
- [81] C. von Clausewitz,
'Vom Kriege',
Ferdinand Dümmler, Berlin (1832) (cit. on p. 7).
- [82] B. Young, M. Kasevich, and S. Chu,
'Precision Atom Interferometry with Light Pulses',
Atom Interferometry, ed. by P. R. Berman, Academic Press (1997) (cit. on pp. 7, 8, 11, 48, 51).
- [83] M. Kasevich and S. Chu,
'Atomic interferometry using stimulated Raman transitions',
Phys. Rev. Lett. **67**, 181–184 (1991) (cit. on pp. 7, 9, 10, 41).
- [84] E. M. Rasel, M. K. Oberthaler, H. Batelaan, J. Schmiedmayer, and A. Zeilinger,
'Atom Wave Interferometry with Diffraction Gratings of Light',
Phys. Rev. Lett. **75**, 2633–2637 (1995) (cit. on p. 7).
- [85] P. R. Berman, ed.,
'Atom Interferometry',
Academic Press (1997) (cit. on p. 7).
- [86] M. Kozuma, L. Deng, E. W. Hagley, J. Wen, R. Lutwak, K. Helmerson, S. L. Rolston, and W. D. Phillips,
'Coherent Splitting of Bose-Einstein Condensed Atoms with Optically Induced Bragg Diffraction',
Phys. Rev. Lett. **82**, 871–875 (1999) (cit. on pp. 7, 77).

- [87] P. A. Altin, M. T. Johnsson, V. Negnevitsky, G. R. Dennis, R. P. Anderson, J. E. Debs, S. S. Szigeti, K. S. Hardman, S. Bennetts, G. D. McDonald, L. D. Turner, J. D. Close, and N. P. Robins, 'Precision atomic gravimeter based on Bragg diffraction', *New Journal of Physics* **15**, 023009– (2013) (cit. on p. 7).
- [88] D. A. Steck, 'Rubidium 87 D Line Data, rev. 2.1.4', (2010) (cit. on pp. 8, 9, 33, 46, 101).
- [89] N. F. Ramsey, 'A Molecular Beam Resonance Method with Separated Oscillating Fields', *Phys. Rev.* **78**, 695–699 (1950) (cit. on p. 10).
- [90] J. Hartwig, 'Analyse eines atomaren Gravimeters hinsichtlich eines Quantentests des Äquivalenzprinzips', PhD thesis, Leibniz Universität Hannover (2013) (cit. on pp. 11, 17, 27, 28, 64, 76).
- [91] A. Peters, K.-Y. Chung, and S. Chu, 'High-precision gravity measurements using atom interferometry', *Metrologia* **38**, 25– (2001) (cit. on p. 11).
- [92] Savas Dimopoulos, Peter W. Graham, Jason M. Hogan, and Mark A. Kasevich, 'General relativistic effects in atom interferometry', *Phys. Rev. D* **78**, 042003– (2008) (cit. on pp. 11, 72).
- [93] P. Cheinet, B. Canuel, F. Pereira dos Santos, A. Gauguier, F. Yver-Leduc, and A. Landragin, 'Measurement of the Sensitivity Function in a Time-Domain Atomic Interferometer', *Instrumentation and Measurement, IEEE Transactions on* **57**, 1141–1148 (2008) (cit. on pp. 12, 13).
- [94] P. Hamilton, T. Barter, G. Kim, B. Mukherjee, and H. Müller, 'Progress towards a test of the universality of free fall using a ${}^6\text{Li}$ - ${}^7\text{Li}$ atom interferometer', *Bull. Am. Phys. Soc.* **57**, T5.00004 (2012) (cit. on pp. 14, 15, 79).
- [95] T. Damour, 'Testing the equivalence principle: why and how?', *Classical and Quantum Gravity* **13**, A33– (1996) (cit. on p. 14).
- [96] D. R. Hofstadter, 'Gödel, Escher, Bach. An Eternal Golden Braid', Basic Books, New York (1979) (cit. on p. 17).
- [97] E. L. Raab, M. Prentiss, Alex Cable, Steven Chu, and D. E. Pritchard, 'Trapping of Neutral Sodium Atoms with Radiation Pressure', *Phys. Rev. Lett.* **59**, 2631–2634 (1987) (cit. on p. 17).
- [98] A. M. Steane, M. Chowdhury, and C. J. Foot, 'Radiation force in the magneto-optical trap', *J. Opt. Soc. Am. B* **9**, 2142–2158 (1992) (cit. on p. 17).

- [99] S. Weyers, E. Aucouturier, C. Valentin, and N. Dimarcq,
'A continuous beam of cold cesium atoms extracted from a two-dimensional magneto-optical trap',
Opt. Comm. **143**, 30–34 (Nov. 1997) (cit. on p. 17).
- [100] K. Dieckmann, R. J. C. Spreeuw, M. Weidemüller, and J. T. M. Walraven,
'Two-dimensional magneto-optical trap as a source of slow atoms',
Phys. Rev. A **58**, 3891–3895 (1998) (cit. on p. 17).
- [101] P. Berthoud, A. Joyet, G. Dudley, N. Sagna, and P. Thomann,
'A continuous beam of slow, cold cesium atoms magnetically extracted from a 2D magneto-optical trap',
Eur. Phys. Lett. **41**, 141– (1998) (cit. on p. 17).
- [102] M. Zaiser,
'Eine Quelle quantenentarteter Gase für die Atominterferometrie',
PhD thesis, Leibniz Universität Hannover (2010) (cit. on pp. 17, 77).
- [103] C. B. Alcock, V. P. Itkin, and M. K. Horrigan,
'Vapor pressure equations for the metallic elements: 298-2500K',
Canadian Metallurgical Quarterly **23**, 309 (1984) (cit. on p. 18).
- [104] W. Demtröder,
'Experimentalphysik 2 Elektrizität und Optik',
Springer (2004) (cit. on p. 19).
- [105] A. Abragam,
'Principles of Nuclear Magnetism',
Oxford University Press (1961) (cit. on p. 19).
- [106] H. Meinke and F. W. Gundlach,
'Taschenbuch der Hochfrequenztechnik',
Springer (1956) (cit. on pp. 19, 20).
- [107] E. Arimondo, M. Inguscio, and P. Violino,
'Experimental determinations of the hyperfine structure in the alkali atoms',
Rev. Mod. Phys. **49**, 31–75 (1977) (cit. on pp. 19, 34, 101–103).
- [108] A. Fölsing,
'Heinrich Hertz',
Hoffmann und Campe (1997) (cit. on p. 20).
- [109] H. Yagi,
'Beam Transmission of Ultra Short Waves',
Proc. IRE **16**, 715–740 (1928) (cit. on p. 20).
- [110] M. A. Lee and K. E. Schmidt,
Yagi Antenna Modeler, 2000, URL: <http://fermi.la.asu.edu/ccli/applets/yagi/yagi.html> (cit. on pp. 21, 107).
- [111] M. E. Meserve,
Javascript Electronic Notebook VHF/UHF Yagi Antenna Design, 2004, URL: http://www.k7mem.com/Electronic_Notebook/antennas/yagi_vhf.html (cit. on pp. 21, 107).

- [112] X. Baillard, A. Gauguet, S. Bize, P. Lemonde, Ph. Laurent, A. Clairon, and P. Rosenbusch, ‘Interference-filter-stabilized external-cavity diode lasers’, *Opt. Comm.* **266**, 609–613 (2006) (cit. on pp. 23, 26).
- [113] M. Gilowski, Ch. Schubert, M. Zaiser, W. Herr, T. Wübbena, T. Wendrich, T. Müller, E.M. Rasel, and W. Ertmer, ‘Narrow bandwidth interference filter-stabilized diode laser systems for the manipulation of neutral atoms’, *Opt. Comm.* **280**, 443–447 (2007) (cit. on pp. 23, 26).
- [114] C. Rode, ‘Aufbau eines kompakten Lasersystems zur Kühlung der Isotope von Rubidium und Kalium’, Diploma thesis, Leibniz Universität Hannover (2009) (cit. on p. 23).
- [115] R. S. Williamson III, ‘Magneto-optical trapping of potassium isotopes’, PhD thesis, University of Wisconsin - Madison (1997) (cit. on p. 23).
- [116] O. Carraz, R. Charrière, M. Cadoret, N. Zahzam, Y. Bidet, and A. Bresson, ‘Phase shift in an atom interferometer induced by the additional laser lines of a Raman laser generated by modulation’, *Phys. Rev. A* **86**, 033605– (Sept. 2012) (cit. on p. 24).
- [117] H. Albers, ‘Atominterferometrie mit ^{39}K ’, MA thesis, Leibniz Universität Hannover (2013) (cit. on pp. 26, 28, 45).
- [118] C. Meiners, ‘Aufbau und Charakterisierung eines Lasersystems für die Interferometrie mit ^{39}K ’, BA thesis, Leibniz Universität Hannover (2012) (cit. on p. 25).
- [119] M. Landini, S. Roy, L. Carcagnì, D. Trypogeorgos, M. Fattori, M. Inguscio, and G. Modugno, ‘Sub-Doppler laser cooling of potassium atoms’, *Phys. Rev. A* **84**, 043432– (2011) (cit. on pp. 27, 33–37, 48, 60).
- [120] T. G. Tiecke, ‘Properties of Potassium, rev. 1.0’, (2010) (cit. on pp. 33, 34, 101).
- [121] G. Modugno, C. Benkö, P. Hannaford, G. Roati, and M. Inguscio, ‘Sub-Doppler laser cooling of fermionic ^{40}K atoms’, *Phys. Rev. A* **60**, R3373–R3376 (1999) (cit. on p. 33).
- [122] S. Falke, E. Tiemann, C. Lisdat, H. Schnatz, and G. Grosche, ‘Transition frequencies of the D lines of ^{39}K , ^{40}K , and ^{41}K measured with a femtosecond laser frequency comb’, *Phys. Rev. A* **74**, 032503– (2006) (cit. on pp. 34, 68, 101–103).
- [123] G. Hertz, ed., ‘Lehrbuch der Kernphysik Band 2’, Teubner (1960) (cit. on p. 34).

- [124] T. Mayer-Kuckuk,
'Kernphysik',
Teubner (1994) (cit. on p. 34).
- [125] M. Landini,
'A tunable Bose-Einstein condensate for quantum interferometry',
PhD thesis, Università degli Studi di Trento (2011) (cit. on pp. 34, 35).
- [126] C. Fort, A. Bambini, L. Cacciapuoti, F. S. Cataliotti, M. Prevedelli, G. M. Tino, and M. Inguscio,
'Cooling mechanisms in potassium magneto-optical traps',
Eur. Phys. J. D **3**, 113–118 (1998) (cit. on p. 35).
- [127] A. Louchet-Chauvet, T. Farah, Q. Bodart, A. Clairon, A. Landragin, S. Merlet, and F. Pereira Dos Santos,
'The influence of transverse motion within an atomic gravimeter',
New J. Phys. **13**, 065025– (2011) (cit. on pp. 36, 56, 69, 73, 78).
- [128] D. C. McKay, D. Jervis, D. J. Fine, J. W. Simpson-Porco, G. J. A. Edge, and J. H. Thywissen,
'Low-temperature high-density magneto-optical trapping of potassium using the $4S \rightarrow 5P$ transition at 405 nm',
Phys. Rev. A **84**, 063420– (2011) (cit. on p. 36).
- [129] G. Salomon, L. Fouché, P. Wang, A. Aspect, P. Bouyer, and T. Bourdel,
'Gray-molasses cooling of ^{39}K to a high phase-space density',
Eur. Phys. Lett. **104**, 63002– (2013) (cit. on pp. 36, 60).
- [130] W. Ketterle, D. S. Durfee, and D. M. Stamper-Kurn,
'Making, probing and understanding Bose-Einstein condensates',
Bose-Einstein condensation in atomic gases, Proceedings of the International School of Physics 'Enrico Fermi', Course CXL, ed. by S. Stringari M. Inguscio and C.E. Wieman, IOS Press, Amsterdam (1999) (cit. on pp. 37, 38, 51).
- [131] T. Petelski,
'Atom Interferometers for Precision Gravity Measurements',
PhD thesis, Université Paris VI (2005) (cit. on p. 41).
- [132] M. Kasevich, D. S. Weiss, E. Riis, K. Moler, S. Kasapi, and S. Chu,
'Atomic velocity selection using stimulated Raman transitions',
Phys. Rev. Lett. **66**, 2297–2300 (1991) (cit. on pp. 43, 49, 50).
- [133] C. J. Foot,
'Atomic Physics',
Oxford University Press (2005) (cit. on pp. 43, 45).
- [134] S. S. Szigeti, J. E. Debs, J. J. Hope, N. P. Robins, and J. D. Close,
'Why momentum width matters for atom interferometry with Bragg pulses',
New Journal of Physics **14**, 023009– (2012) (cit. on p. 51).
- [135] P. Cheinet,
'Conception et Réalisation d'un Gravimètre à Atomes Froids',
Dissertation, Université Paris VI (2006) (cit. on pp. 51, 52).

- [136] W. Demtröder,
‘Experimentalphysik 1: Mechanik und Wärme’,
Springer (2006) (cit. on p. 51).
- [137] T. Kovachy, J. M. Hogan, A. Sugarbaker, S. M. Dickerson, C. A. Donnelly, C. Overstreet,
and M. A. Kasevich,
‘Matter wave lensing to picokelvin temperatures’,
arXiv:1407.6995 (cit. on pp. 54, 77, 78).
- [138] J. M. McGuirk, G. T. Foster, J. B. Fixler, M. J. Snadden, and M. A. Kasevich,
‘Sensitive absolute-gravity gradiometry using atom interferometry’,
Phys. Rev. A **65**, 033608– (2002) (cit. on p. 56).
- [139] G. Varoquaux, R. A. Nyman, R. Geiger, P. Cheinet, A. Landragin, and P. Bouyer,
‘How to estimate the differential acceleration in a two-species atom interferometer to test
the equivalence principle’,
New J. Phys. **11**, 113010– (2009) (cit. on pp. 65, 75–77).
- [140] X. Chen, J. Zhong, H. Song, L. Zhu, J. Wang, and M. Zhan,
‘Proportional-scanning-phase method to suppress the vibrational noise in nonisotope
dual-atom-interferometer-based weak-equivalence-principle-test experiments’,
Phys. Rev. A **90**, 023609– (2014) (cit. on pp. 65, 75, 76).
- [141] G. Breit and I. I. Rabi,
‘Measurement of Nuclear Spin’,
Phys. Rev. **38**, 2082–2083 (1931) (cit. on p. 67).
- [142] J. Ye, S. Swartz, P. Jungner, and J. L. Hall,
‘Hyperfine structure and absolute frequency of the ^{87}Rb $5P_{3/2}$ state’,
Opt. Lett. **21**, 1280–1282 (1996) (cit. on p. 68).
- [143] URL: <https://openclipart.org/> (cit. on p. 70).
- [144] F. Riehle, T. Kisters, A. Witte, J. Helmcke, and C. J. Bordé,
‘Optical Ramsey spectroscopy in a rotating frame: Sagnac effect in a matter-wave interfer-
ometer’,
Phys. Rev. Lett. **67**, 177–180 (1991) (cit. on p. 70).
- [145] G. Tackmann, P. Berg, C. Schubert, S. Abend, M. Gilowski, W. Ertmer, and E. M. Rasel,
‘Self-alignment of a compact large-area atomic Sagnac interferometer’,
New Journal of Physics **14**, 015002– (2012) (cit. on p. 70).
- [146] S.-Y. Lan, P.-C. Kuan, B. Estey, P. Haslinger, and H. Müller,
‘Influence of the Coriolis Force in Atom Interferometry’,
Phys. Rev. Lett. **108**, 090402– (2012) (cit. on pp. 70, 72).
- [147] A. Gauguet, T. E. Mehlstäubler, T. Lévèque, J. Le Gouët, W. Chaibi, B. Canuel, A.
Clairon, F. Pereira Dos Santos, and A. Landragin,
‘Off-resonant Raman transition impact in an atom interferometer’,
Phys. Rev. A **78**, 043615– (2008) (cit. on p. 71).
- [148] J. Le Gouët, T.E. Mehlstäubler, J. Kim, S. Merlet, A. Clairon, A. Landragin, and F.
Pereira Dos Santos,
‘Limits to the sensitivity of a low noise compact atomic gravimeter’,
Appl. Phys. B **92**, 133–144– (2008) (cit. on p. 76).

- [149] M. Hauth, C. Freier, V. Schkolnik, A. Senger, M. Schmidt, and A. Peters, ‘First gravity measurements using the mobile atom interferometer GAIN’, *Appl. Phys. B* **113**, 49–55– (2013) (cit. on p. 76).
- [150] Z.-K. Hu, B.-L. Sun, X.-C. Duan, M.-K. Zhou, L.-L. Chen, S. Zhan, Q.-Z. Zhang, and J. Luo, ‘Demonstration of an ultrahigh-sensitivity atom-interferometry absolute gravimeter’, *Phys. Rev. A* **88**, 043610– (2013) (cit. on p. 76).
- [151] R. Geiger, V. Ménot, G. Stern, N. Zahzam, P. Cheinet, B. Battelier, A. Villing, F. Moron, M. Lours, Y. Bidel, A. Bresson, A. Landragin, and P. Bouyer, ‘Detecting inertial effects with airborne matter-wave interferometry’, *Nat Commun* **2**, 474– (2011) (cit. on p. 76).
- [152] E. Giese, A. Roura, G. Tackmann, E. M. Rasel, and W. P. Schleich, ‘Double Bragg diffraction: A tool for atom optics’, *Phys. Rev. A* **88**, 053608– (2013) (cit. on p. 77).
- [153] W. Herr, ‘Eine kompakte Quelle quantenentarteter Gase hohen Flusses für die Atominterferometrie unter Schwerelosigkeit’, PhD thesis, Leibniz Universität Hannover (2013) (cit. on p. 77).
- [154] G. Modugno, G. Ferrari, G. Roati, R. J. Brecha, A. Simoni, and M. Inguscio, ‘Bose-Einstein Condensation of Potassium Atoms by Sympathetic Cooling’, *Science* **294**, 1320–1322 (2001) (cit. on pp. 77, 78).
- [155] G. Roati, M. Zaccanti, C. D’Errico, J. Catani, M. Modugno, A. Simoni, M. Inguscio, and G. Modugno, ‘³⁹ Bose-Einstein Condensate with Tunable Interactions’, *Phys. Rev. Lett.* **99**, 010403– (2007) (cit. on pp. 77, 78).
- [156] M. Zaiser, J. Hartwig, D. Schlippert, U. Velte, N. Winter, V. Lebedev, W. Ertmer, and E. M. Rasel, ‘Simple method for generating Bose-Einstein condensates in a weak hybrid trap’, *Phys. Rev. A* **83**, 035601 (2011) (cit. on pp. 77, 78).
- [157] M. Landini, S. Roy, G. Roati, A. Simoni, M. Inguscio, G. Modugno, and M. Fattori, ‘Direct evaporative cooling of ³⁹K atoms to Bose-Einstein condensation’, *Phys. Rev. A* **86**, 033421– (2012) (cit. on p. 78).
- [158] G. Salomon, L. Fouché, S. Lepoutre, A. Aspect, and T. Bourdel, ‘All optical cooling of ³⁹K to Bose Einstein condensation’, arXiv:1312.5963 (cit. on p. 78).
- [159] C. Chin, R. Grimm, P. Julienne, and E. Tiesinga, ‘Feshbach resonances in ultracold gases’, *Rev. Mod. Phys.* **82**, 1225–1286 (2010) (cit. on p. 78).
- [160] C. L. Hung, X. Zhang, N. Gemelke, and C. Chin, ‘Accelerating evaporative cooling of atoms into Bose-Einstein condensation in optical traps’, *Phys. Rev. A* **78**, 011604 (2008) (cit. on p. 78).

- [161] L. Zhou, Z.Y. Xiong, W. Yang, B. Tang, W.C. Peng, K. Hao, R.B. Li, M. Liu, J. Wang, and M.S. Zhan,
‘Development of an atom gravimeter and status of the 10-meter atom interferometer for precision gravity measurement’,
General Relativity and Gravitation **43**, 1931–1942– (2011) (cit. on p. 79).
- [162] J. Hartwig, S. Abend, C. Schubert, D. Schlippert, H. Ahlers, K. Posso-Trujillo, N. Gaaloul, W. Ertmer, and E. M. Rasel,
‘Testing the universality of free fall with rubidium and ytterbium in a very large baseline atom interferometer’,
Submitted to New J. Phys. (2014) (cit. on p. 79).
- [163] G. Stern, B. Battelier, R. Geiger, G. Varoquaux, A. Villing, F. Moron, O. Carraz, N. Zahzam, Y. Bidet, W. Chaibi, F. Pereira Dos Santos, A. Bresson, A. Landragin, and P. Bouyer,
‘Light-pulse atom interferometry in microgravity’,
Eur. Phys. J. D **53**, 353–357– (2009) (cit. on p. 79).
- [164] J. Rudolph *et al.*,
‘Degenerate Quantum Gases in Microgravity’,
Microgravity Science and Technology **23**, 287–292– (2011) (cit. on p. 79).
- [165] J. Rudolph, W. Herr, C. Grzeschik, T. Sternke, A. Grote, M. Popp, D. Becker, H. Müntinga, H. Ahlers, A. Peters, C. Lämmerzahl, K. Sengstock, N. Gaaloul, W. Ertmer, and E. M. Rasel,
‘A high-flux BEC source for mobile atom interferometers’,
Submitted to New J. Phys. (2014) (cit. on p. 79).
- [166] S. Herrmann, E. Göklü, H. Müntinga, A. Resch, T. van Zoest, H. Dittus, and C. Lämmerzahl,
‘Testing Fundamental Physics with Degenerate Quantum Gases in Microgravity’,
Microgravity Science and Technology **22**, 529–538– (2010) (cit. on p. 79).
- [167] S. Herrmann, H. Dittus, and C. Lämmerzahl,
‘Testing the equivalence principle with atomic interferometry’,
Classical and Quantum Gravity **29**, 184003– (2012) (cit. on p. 79).
- [168] S. T. Seidel, N. Gaaloul, and E. M. Rasel,
‘MAIUS - A Rocket-Born Test of an Atom Interferometer with a Chip-Based Atom Laser’,
Proceedings of the 63rd International Astronautical Congress 2012 **3**, 801 (2013) (cit. on p. 79).
- [169] T. Jenke, P. Geltenbort, H. Lemmel, and H. Abele,
‘Realization of a gravity-resonance-spectroscopy technique’,
Nat. Phys. **7**, 468–472 (2011) (cit. on p. 78).
- [170] E. Kajari, N. L. Harshman, E. M. Rasel, S. Stenholm, G. Süßmann, and W. P. Schleich,
‘Inertial and gravitational mass in quantum mechanics’,
Appl. Phys. B **100**, 43–60– (2010) (cit. on p. 78).
- [171] M. Zych, F. Costa, I. Pikovski, and Č. Brukner,
‘Quantum interferometric visibility as a witness of general relativistic proper time’,
Nat. Commun. **2**, 505– (2011) (cit. on p. 78).

- [172] M. Zych and Č. Brukner,
‘Quantum Weak Equivalence Principle’,
Verhandl. DPG (VI) **49.2**, (2014) (cit. on p. 78).
- [173] C. Burrage, E. J. Copeland, and E. A. Hinds,
‘Probing Dark Energy with Atom Interferometry’,
arXiv:1408.1409 (cit. on p. 78).
- [174] B. Lücke, M. Scherer, J. Kruse, L. Pezzé, F. Deuretzbacher, P. Hyllus, O. Topic, J. Peise,
W. Ertmer, J. Arlt, L. Santos, A. Smerzi, and C. Klempt,
‘Twin Matter Waves for Interferometry Beyond the Classical Limit’,
Science **334**, 773–776 (2011) (cit. on p. 79).
- [175] R. Bücker, J. Grond, S. Manz, T. Berrada, T. Betz, C. Koller, U. Hohenester, T. Schumm,
A. Perrin, and J. Schmiedmayer,
‘Twin-atom beams’,
Nat. Phys. **7**, 608–611 (2011) (cit. on p. 79).
- [176] T. Berrada, S. van Frank, R. Bücker, T. Schumm, J.-F. Schaff, and J. Schmiedmayer,
‘Integrated Mach-Zehnder interferometer for Bose-Einstein condensates’,
Nat. Commun. **4**, – (2013) (cit. on p. 79).
- [177] J. Lee, G. Vrijsen, I. Teper, and M. A. Hosten O. Kasevich,
‘A Many-Atom Cavity QED System with Homogeneous Atom-Cavity Coupling’,
arXiv:1311.1805 (cit. on p. 79).
- [178] J. G. Bohnet, K. C. Cox, M. A. Norcia, Weiner J. M., Z. Chen, and Thompson J. K.,
‘Reduced spin measurement back-action for a phase sensitivity ten times beyond the
standard quantum limit’,
Nat Photon **8**, 731–736 (2014) (cit. on p. 79).
- [179] M. Landini, M. Fattori, L. Pezzé, and A. Smerzi,
‘Phase-noise protection in quantum-enhanced differential interferometry’,
arXiv:1409.1703 (cit. on p. 79).
- [180] URL: <http://www.hitec.uni-hannover.de/> (cit. on p. 79).
- [181] E. G. Adelberger, *private communication* (2014) (cit. on p. 80).
- [182] J. Emsley,
‘The Elements’,
Oxford Univ. Press, New York (1995) (cit. on p. 101).

List of Figures

1.1	Comparison of neutral matter test masses in the standard model extension	5
2.1	Coherent two-photon transition	8
2.2	Ideal Rabi oscillations	9
2.3	Space-time diagram of a Mach-Zehnder interferometer	10
2.4	Compensating for the gravitationally induced phase shift	11
2.5	Sensitivity function	13
3.1	Vacuum system	18
3.2	Comparison of a dipole antenna and YAGI-UDA antenna	20
3.3	Radio-frequency source setup	21
3.4	Potassium hyperfine transitions driven with radio-frequency radiation	22
3.6	Detunings for potassium dual MOT operation	24
3.7	Cavity signals of the 2D MOT and 3D MOT outputs	25
3.8	Potassium dual MOT laser system	26
3.9	Shared fiber distribution system	28
3.10	Potassium RAMAN optical setup	29
3.11	Schematic of RAMAN phase lock	30
3.12	Interferometry and detection optics	31
4.1	D ₂ line energy diagram of ³⁹ K	34
4.2	Detunings for potassium dual MOT operation	35
4.3	Characterization of the 2D and 3D MOT performance	36
4.4	Sub-DOPPLER cooling sequence and time-of-flight series	37
4.5	Detection sequence	39
4.6	Optical pumping scheme	39
4.7	Loss simulation for fluorescence detection of ³⁹ K	40
4.8	Two-photon Raman transition	41
4.9	Doppler-insensitive and -sensitive transitions	42
4.10	Raman excitation spectrum	44
4.11	One-photon AC-Stark shift	45
4.12	Raman laser frequency intensity ratio	47
4.13	Magnetic substate purification	49
4.14	Velocity selection sequence	50
4.15	Enhanced velocity and magnetic selection sequence	52
4.16	Doppler-sensitive Rabi oscillations	53

4.17	Simulation of Raman excitation probability	54
4.18	Space-time diagram of a Mach-Zehnder interferometer	55
4.19	Demonstration of k -reversal scheme	56
4.20	Allan deviation of a potassium long-term measurement	57
4.21	Determination of gravitational acceleration with potassium	58
4.22	Comparison of Raman beam splitting stabilities	59
4.23	Inertial-sensitive potassium fringes	60
5.1	Space-time diagram of a dual species Mach-Zehnder interferometer	63
5.2	Determination of the differential gravitational acceleration of rubidium and potassium	65
5.3	Allan deviation of UFF measurement	66
5.4	Residual magnetic gradient measurement	68
5.5	Influence of wavefront curvature	69
5.6	Influence of the Coriolis force	70
5.7	Two-photon light shift	71
6.1	Extrapolated Allan deviation	76
A.1	D ₂ line energy diagrams of ³⁹ K, ⁴⁰ K, and ⁴¹ K	102
B.1	D ₂ line energy diagram of ³⁹ K and laser frequencies	103
D.1	Yagi-Uda antenna	107

List of Tables

1.1	Overview of matter wave tests of the UFF	3
2.1	Comparison model of test masses A and B in the dilaton	14
2.2	Comparison of test masses A and B in the SME	15
5.1	Overview of systematic effects and their uncertainties	72
6.1	Comparison of the current and advanced systematic uncertainties	77
6.2	Proposed matter wave tests of the UFF	79
A.1	Atomic properties of rubidium and potassium	101
A.2	Comparison of alkali properties	101
C.1	Parameters used for the systematic uncertainty estimation	105
D.1	Dimensions and specifications of the used antennas	107

APPENDIX A

Properties of ^{87}Rb and ^{39}K

In Table A.1, atomic properties of ^{87}Rb and ^{39}K are compared. Table A.2 shows a comparison of the stable potassium isotopes with the neighboring elements, sodium and rubidium, with respect to the abundance and the hyperfine splitting. Figure A.1 depicts the D_1 and D_2 line electronic structure of the stable potassium isotopes.

Table A.1: Atomic properties of rubidium and potassium as stated in Refs. [88, 107, 120, 122].

	^{87}Rb	^{39}K
Atomic mass in u	86.91	38.96
Nuclear spin	3/2	3/2
D_2 transition frequency in THz	$2\pi \cdot 384.230\,484\,468\,5$	$2\pi \cdot 391.016\,170\,03$
D_2 transition wavelength in nm	780.241 209 686	766.700 921 822
D_2 natural linewidth in MHz	$2\pi \cdot 6.067$	$2\pi \cdot 6.035$
Saturation intensity in mW/cm^2	1.73	1.75
Hyperfine transition frequency ω_{12} in MHz	$2\pi \cdot 6834.682\,610\,904$	$2\pi \cdot 461.719\,720\,1$
Recoil frequency ω_r in kHz	$2\pi \cdot 3.77$	$2\pi \cdot 8.67$
Recoil velocity v_r in mm/s	5.8845	13.2983
Recoil temperature T_r in nK	361.96	418.06

Table A.2: Comparison of alkali properties as stated in Refs. [107, 182]. The atomic mass is stated in atomic mass units u, the nuclear magnetic moment is stated in units of the nuclear magneton μ_N .

Isotope	Mass in u	Abundance	Nuclear spin	Magnetic moment in μ/μ_N	Hyperfine frequency ω_{12} in MHz
^{39}K	38.963707	93.258 %	3/2	+0.391	461.7
^{40}K	39.963999	0.012 %	4	-1.298	1285.8
^{41}K	40.961825	6.730 %	3/2	+0.215	254.0
^{23}Na	22.989767	100 %	3/2	+2.218	1771.6
^{85}Rb	84.911794	72.17 %	5/2	+1.353	3035.7
^{87}Rb	86.909187	27.83 %	3/2	+2.751	6834.7

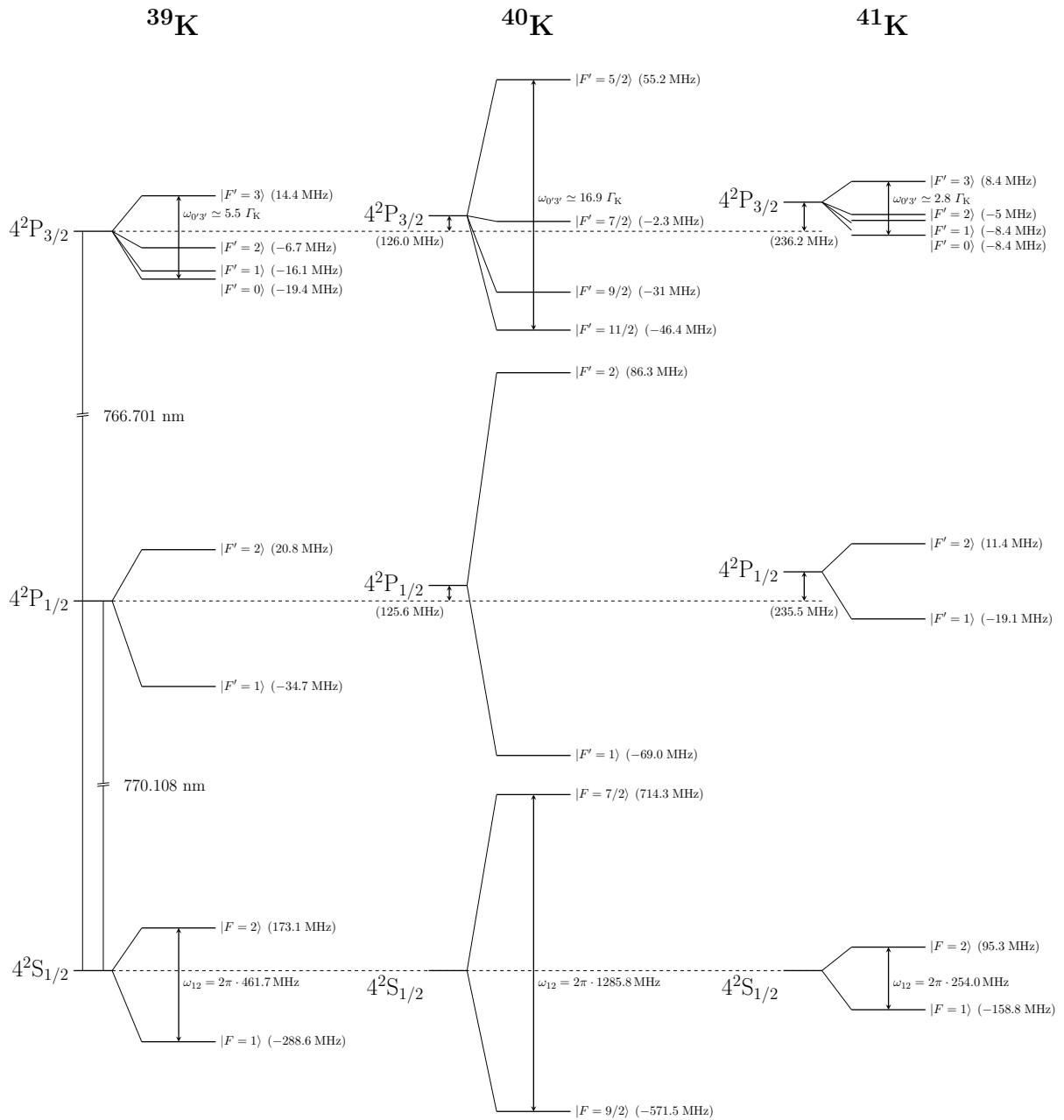


Figure A.1: Energy diagrams of ^{39}K , ^{40}K , and ^{41}K . Numerical values are taken from [107, 122] and frequencies are stated in ordinary frequency.

APPENDIX B

^{39}K laser frequencies

Figure B.1 shows all laser detunings used in the experiment.

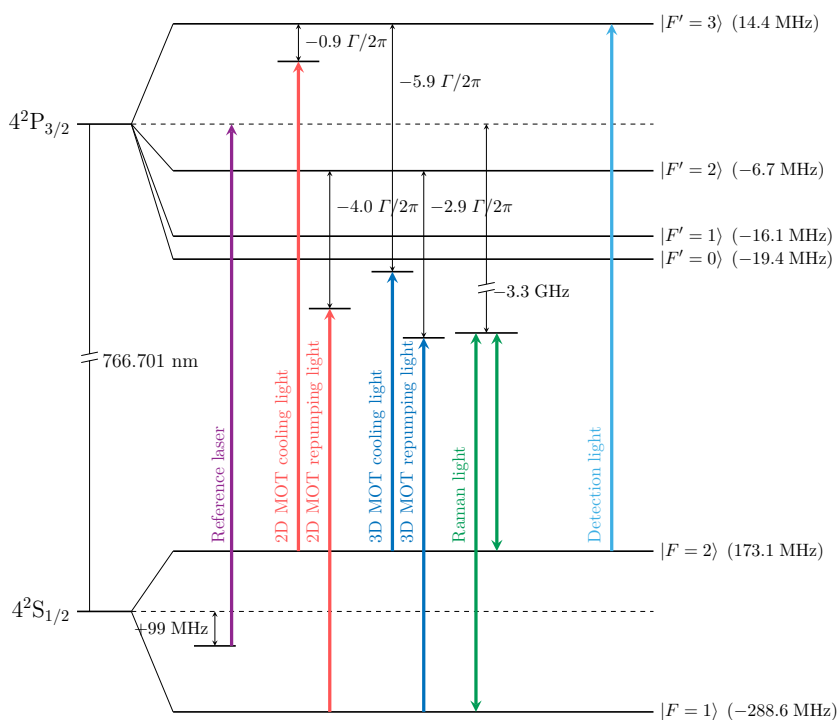


Figure B.1: D₂ line energy diagram of and the laser frequencies used in the experiment. Numerical values are taken from [107, 122] and frequencies are stated in ordinary frequency. In this thesis, numerical values for the overall RAMAN detuning are stated with respect to the reference laser.

APPENDIX C

Parameters used for the systematic uncertainty estimation

The parameters for the estimation of bias contributions $\Delta\eta$ and their related uncertainties $\delta\eta$ performed in Section 5.2 are listed in Table C.1.

Table C.1: Parameters used for the estimation of bias contributions $\Delta\eta$ and their uncertainties $\delta\eta$.

Ensemble parameters	⁸⁷ Rb	³⁹ K
Temperature in μK	27	32
Initial size	1 mm	
Differential position	1 mm	
Differential velocity	1 mm/s	
Interferometer parameters		
Free fall time before 1 st pulse t_{TOF}	43 ms	
Pulse separation time T	20 ms	
π -pulse width τ_π	15 μs	
RAMAN light field parameters		
Polarization	σ/σ	
Detuning $\Delta/2\pi$ in GHz	1.6	3.3
Frequency uncertainty $\Delta\omega_i/2\pi$	700 kHz	
Total power P_{tot} in mW	80	200
Intensity ratio I_2/I_1	2:1	1:1
Linear power drift P/P_{tot}	$5 \times 10^{-6} \text{ s}^{-1}$	
Radius σ_L	9.6 mm	
Vertical alignment uncertainty $\delta\alpha$	0.03 mrad	
Wavefront curvature R	300 m	

APPENDIX D

Radio frequency antenna

In Table D.1, the dimensions and the simulated gain factor G of the YAGI-UDA antenna (Figure D.1) described in Section 3.1.2 are compared to the half-wave dipole antenna.

Table D.1: Dimensions as labeled in Figure 3.2, and simulated gain factors G and impedances Z_L of the used antennas [110, 111]. All antenna elements are made of copper wire with a diameter of 2 mm.

		Half-wave dipole		YAGI-UDA antenna	
Gain factor G		1.65		4.94	
Impedance Z_L in Ω		$93.35 + i 51.31$		$41.51 + i 21.99$	
Antenna element	l_x in mm	d_x in mm	l_x in mm	d_x in mm	
Driven element	326.0	-	314.1	97.6	
Director	-	-	290.6	139.8	
Reflector	-	-	318.0	0.0	



Figure D.1: Photograph of the YAGI-UDA antenna employed in the experiment.

